UNIVERSITY OF CALIFORNIA

Santa Barbara

The Effects of Tau Proteins on Microtubule Mechanics and Molecular Motor Transport

A dissertation submitted in partial satisfaction of the

requirements for the degree Doctor of Philosophy

in Materials

by

Dezhi Yu

Committee in charge:

Professor Megan T. Valentine, Chair

Professor Philip Pincus

Professor Cyrus R. Safinya

Professor Omar A. Saleh

December 2014

The dissertation of Dezhi Yu is approved.

_____

Philip Pincus

_____

Cyrus R. Safinya

_____

Omar A. Saleh

_____

Megan T. Valentine, Committee Chair

December 2014

ACKNOWLEDGEMENTS

I would like to dedicate this thesis to all the people who have been a part of my life during my years in UCSB. The completion of this thesis would not have been possible without all of you. First and foremost, I would like to express my sincere gratitude to my advisor and committee chair Professor Megan Valentine for providing the opportunity and continuous support that I need to complete my PhD study in one of the most prestigious programs in the world. It has been my great honor to be a member of the Valentine Lab under the guidance of Dr. Valentine's enthusiasm and professionalism. Furthermore, I would like to thank Professor Stuart Feinstein for his words of wisdom, encouragements and his generosity in permitting me to use the resources and equipment in his lab. I would also like to thank all my committee members for their kind and helpful advice.

Secondly, I would like to thank my parents, my girlfriend Jenny, and all my friends for their patience and support. I am very grateful for all the fun and joy that all of you have provided me over the years to help me get through the gruesome days of my academic career.

Last but not least, I would like to thank my lab manager, Donna Mancusi, all former and current members of the Valentine Lab, Feinstein Lab, and Saleh Lab for all their help and advice.

VITA OF DEZHI YU
December 2014

EDUCATION

BS in Mechanical Engineering, University of California, Santa Barbara 2009 (highest honor)
MS in Bio/Macromolecular Materials, University of California, Santa Barbara 2010
PhD in Bio/Macromolecular Materials, University of California, Santa Barbara 2014 (expected)

PROFESSIONAL EMPLOYMENT

2009-2014: Graduate student researcher, Valentine Lab, University of California, Santa Barbara
Spring 2011: Teaching Assistant, Materials Department, University of California, Santa Barbara

PUBLICATIONS

Yu, D., LaPointe, N. E., Guzman, E., Pessino, V., Wilson, L., Feinstein, S. C., & Valentine, M. T. (2014). Tau Proteins Harboring Neurodegeneration-Linked Mutations Impair Kinesin Translocation in vitro. Journal of Alzheimer's Disease. **39**(2): p. 301-314.

Yu, D., Pessino, V., Kuei, S., & Valentine, M. T. (2013). Mechanical and functional properties of epothilone-stabilized microtubules. Cytoskeleton. **70**(2): p. 74-84.

Valdman, D., Atzberger, P. J., Yu, D., Kuei, S., & Valentine, M. T. (2012). Spectral analysis methods for the robust measurement of the flexural rigidity of biopolymers. Biophysical journal, 102(5), 1144-1153.

ABSTRACT

The Effects of Tau Proteins on Microtubule Mechanics and Molecular Motor Transport

by

Dezhi Yu

Microtubules are an essential component of the cytoskeleton that provide structural integrity and facilitate important functions in cells. In this work, I will explore several aspects of microtubule mechanics and function using a wide range of biophysical techniques. I am particularly interested in the effects of stabilizing agents, including small molecule inhibitors of microtubule dynamics (such as taxol or epothilone), and microtubule-binding proteins, such as tau. First, using advanced spectral analytical techniques, we studied the effects of tau proteins on the mechanical properties of single microtubule (MT) filaments under controlled *in vitro* conditions. We found that the short forms of 3-repeat (3R) and 4-repeat (4R) wild-type (WT) tau proteins reduce the stiffness of taxol-assembled MTs compared to a no tau control, despite the fact that the microtubule diameter is known to increase when these tau proteins bind. In contrast, single point tau mutants P301L, R406W and ΔN296, which are all linked to devastating neurological diseases, do not have significant effects on microtubule stiffness compared to a no tau control, raising interesting questions about possible mechanical origins of tauopathy diseases.

Next, we examined the effects of tau proteins on *in vitro* transport properties of kinesin-bound cargoes on microtubules. In comparison to the no tau control, kinesin-bound quantum dot cargoes had lower velocity and shorter run lengths in the presence of tau when moving on taxol-assembled microtubules. Most of the single point tau mutants that we tested showed similar slowing of cargo translocation, with speed reductions similar to those observed with WT tau. One exception was the 4R short R406W mutant tau, in which the velocities of kinesin-bound cargoes were significantly lower than in WT case. The disease mechanism for mutant has been particularly puzzling, so our results may suggest a more prominent role in disruption of axonal transport than was previously appreciated.

Next, we investigated the effects of microtubule-stabilizing chemicals epothilone-A and -B on 1) microtubule mechanics, 2) the transport properties of kinesins and 3) the ability of WT tau proteins modify the stiffness of microtubules assembled with epothilone. We found that microtubules assembled in the presence of epothilone-A or –B were less stiff compared to taxol-assembled MTs, and the addition of WT tau further reduced the stiffness. However, the differences in stiffness/persistence length between epothilone-assembled microtubules and taxol-assembled microtubules diminished after the addition of WT tau. Kinesin translocation speed was sensitive to the type of stabilizing chemical, and the changes in velocity in the presence of tau were also depended on the assembly condition. Epothiolone and taxol compunds are both frequently used in cancer chemotherapies, and our results shed light on the possible molecular mechanisms of neurological side effects (such as debilitating nerve pain) when these agents are used.

Lastly, we looked at the effects of tau on intracellular trafficking in COS-7 cells. We found that the microtubule network in the cells were dramatically modified after the introduction of tau via transient transfection, with substantial bundling, aggregation and membrane-association in the presence of tau. However, there were no obvious differences in the microtubule network structures between cells that were transfected with mutant tau and wild-type tau. Interestingly, despite the major modification of the cytoskeletal structures in the presence of tau, the measured velocities of lysosomes in directed transport in cells that were transfected with tau were not significantly different compared to the lysosome velocities in cells with no tau.

Taken together, studies provide important new insights into how tau proteins and other small molecule stabilizers modulate the mechanical and functional properties of cytoskeletal microtubules and how misregulations in tau may be related to the development of neurodegeneration and dementia diseases.

Table of Contents

I. Introduction

The cytoskeleton is comprised of several interpenetrated biopolymer networks inside a cell that composed with three classes of filaments: actin, intermediate filaments and microtubules. The cytoskeletal network not only provides structural support to maintain the integrity of a cell, it also participates in and facilitates in many essential processes such as force generation, cell division and intracellular transport. Microtubules (MTs) are the stiffest of the cytoskeletal polymers and are well known for their role in facilitating axonal transport in mammalian neurons. These unique properties and physiological relevance make MTs one of the most interesting topics to study in both the field of polymer science and biology.

Microtubules are polymers formed from α- and β- tubulin dimers (Figure 1-1). In cells, these tubulin dimers self-assemble into microscopic tubes with 13 protofilaments, outer diameter of ~25 nm and inner diameter of ~15 nm. MTs are structurally-asymmetry (or "polar") polymers with tubulin additions mainly occurring in the fast-growing + ends of the polymers where the β- tubulins were exposed. MTs generally grow from the centers to the peripheries of the cells. Unlike conventional synthetic polymers, tubulin dimers in MTs are not covalently bonded and MTs inside cells undergo periods of growth and shrinkage in a process as known as dynamic instability [1]. The dynamics of MTs in cells are regulated by different microtubule associated proteins (MAPs). MT binding protein, tau, is one of the best-studied MAPs that will be investigated extensively in my research and will be described in more detail in latter parts of this proposal. Other than through the use of MAPs, MT dynamics can also be regulated using synthetic chemicals. Paclitaxol (taxol) is a small-molecule inhibitor known to stabilize MTs and inhibit MT dynamic instability [2], and it is

used in chemotherapy to treat solid-mass cancers. These MAPs and small molecule stabilizer are also known to change MT structure by modulating the number of tubulin protofilaments and to modify the molecular structure and conformation of tubulin dimers [3-6]. These changes in MT structure not only affect the material and mechanical properties of MTs, but also change the geometry of the MT surface and possibly create physical hindrances, which can alter the binding and stepping behaviors of molecular motors [7]. Disruptions, misregulations and blockages in motor-driven transport can be detrimental to the well-being of cells, especially neurons where directed molecular transport along long axons are prominent and essential to cell health [8].

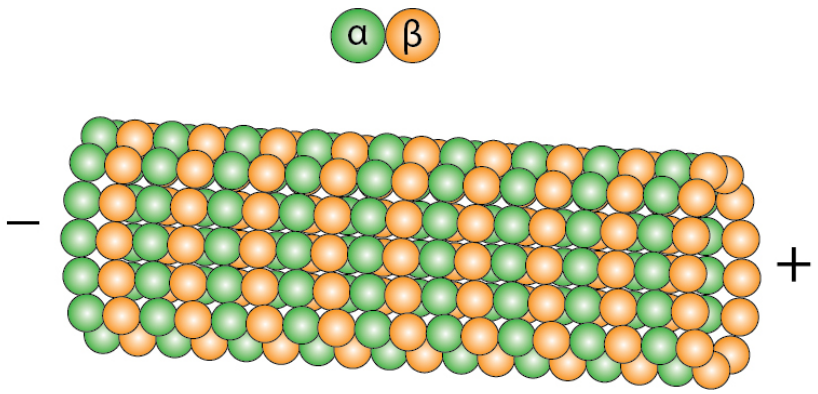

Figure 1-1: Schematic picture of microtubule structure

This thesis will discuss the following topics: 1) Exploring the mechanical properties of MTs *in vitro* under various chemical conditions (*i.e.* in the presence/absence of different microtubule associated proteins, different types of chemical stabilizers, and/or different types of nucleotides) in efforts to understand and establish models of how the structures of MTs vary under different conditions. 2) Investigating the effects of tau and disease-related

mutations of tau proteins on MT functional properties such as intracellular transport, which is investigated using kinesin translocation on MTs under simplified *in vitro* systems, in order to understand the role of intracellular transport or the lack thereof in disease and dementia development. 3) Applying similar biophysical tools to study the effect of wild-type and mutant tau on cargo trafficking in a highly complex system inside a cell.

II. Tau Proteins Harboring Neurodegeneration-linked Mutations Impair Kinesin Translocation *in vitro*[1]

The following work was a collaborated project between the Valentine Lab, Mechanical Engineering, UCSB, the Feinstein Lab, MCDB, UCSB and the Wilson Lab, MCDB, UCSB. All information in this section was published in the Journal of Alzheimer's Disease in 2014 [9]. All supplemental materials can be found on publisher's website site.

In this section, we will investigate the effect of wild-type tau and disease-related tau mutants on *in vitro* transport properties of kinesins.

A. Abstract

We tested the hypothesis that mutant tau proteins that cause neurodegeneration and dementia differentially alter kinesin translocation along MTs relative to normal tau *in vitro*. We employed complementary *in vitro* motility assays using purified recombinant kinesin, purified recombinant tau and purified bovine brain α:β tubulin to isolate interactions among these components without any contribution by cellular regulatory mechanisms. We found that kinesin translocates slower along MTs assembled by any of three independent tau mutants (4-repeat P301L tau, 4-repeat ΔN296 tau and 4-repeat R406W tau) relative to its translocation rate along MTs assembled by normal, 4-repeat wild type (WT) tau. Moreover, the R406W mutation exhibited isoform specific effects; while kinesin translocation along 4-repeat R406W tau assembled MTs is slower than along MTs assembled by 4-repeat WT tau,

[1] Reprinted from Journal of Alzheimer's Disease 39 (2), Yu, D., et al., Tau Proteins Harboring Neurodegeneration-Linked Mutations Impair Kinesin Translocation in vitro, 301-314, Copyright (2014), with permission from IOS Press.

the R406W mutation had no effect in the 3-repeat tau context. These data provide strong support for the notion that aberrant modulation of kinesin translocation is a component of tau-mediated neuronal cell death and dementia. Finally, we showed that assembling MTs with taxol before coating them with mutant tau obscured effects of the mutant tau that were readily apparent using more physiologically relevant MTs assembled with tau alone, raising important issues regarding the use of taxol as an experimental reagent and novel insights into therapeutic mechanisms of taxol action.

B. Introduction

The amyloid hypothesis, built upon both genetic and biochemical observations, suggests that Alzheimer's disease (AD) is initiated by the Aβ peptide, a small fragment derived from the amyloid precursor protein. More recent investigations indicate that Aβ-mediated neuronal cell death requires downstream action by tau [10], a neural microtubule (MT)-associated protein (MAP) that is essential for the normal development and maintenance of the central nervous system (CNS) [11-13]. Biochemically, AD tau is known to be hyperphosphorylated, fragmented and assembled into aggregates known as neurofibrillary tangles. These same tau modifications are also observed in numerous AD-related neurodegenerative diseases, collectively known as tauopathies [14, 15].

A number of tauopathies, including FTDP-17, PSP and CBD, have been genetically linked to mutations in the tau gene [10, 16-20]. Patients with these diseases do not exhibit any Aβ abnormalities, consistent with a downstream role for tau in Aβ-mediated neuronal cell death in AD and demonstrating that aberrant tau action alone is sufficient to cause

neurodegeneration. Disease-linked tau mutations fall into two groups: structural mutations that alter the tau amino acid sequence, and regulatory mutations that alter the expression ratios of the six different CNS tau isoforms generated via developmentally controlled alternative RNA splicing (Figure 2-1) [21-23]. The mechanisms by which these tau mutations promote neurodegeneration and dementia remain poorly understood, but once elucidated, may provide insights into the pathogenesis of AD and other tauopathies.

It has been recently hypothesized that errors in cargo transport along MTs may underlie some aspects of neurodegeneration in AD and other diseases (for example, see [24-26]), leading to increasing efforts to examine the role of tau in axonal transport. A number of cellular studies have shown that wild type (WT) tau can regulate kinesin activity and that the disruption of tau-kinesin interactions can compromise axonal transport. For example, over-expression of WT tau in cultured neuronal cells led to impaired axonal transport, organelle depletion in neuronal processes, enhanced oxidative stress in distal neuritic regions and a net retrograde bias of dynein-associated cargo [8, 27-29]. Similarly, over-expression of WT tau in transgenic mice led to axonal degeneration and accumulation of mitochondria and vesicles in the cell soma [30]. However, the magnitude of tau-mediated effects upon kinesin was less marked in other experimental systems. For example, tau showed a limited effect on axonal transport in murine retinal ganglion cells [31] and isolated squid axoplasm [32].

In vitro studies using completely reconstituted systems can identify direct effects of tau on kinesin-driven transport along MTs in the absence of complicating cellular regulatory mechanisms (such as tau phosphorylation). For example, a number of studies have shown

that the addition of WT tau to taxol-assembled MTs *in vitro* inhibits the subsequent binding of kinesin to MTs and decreases the kinesin run length, but has little effect on translocation velocity [7, 28, 33, 34]. Importantly, these effects can depend on which alternatively spliced isoform of tau is used. Each of the six naturally-occurring tau isoforms possess either three or four imperfect repeats in the C-terminal half of the protein ("3R tau" versus "4R tau"), separated from one another by shorter inter-repeats (Figure 2-1) [21, 35]. This region of repeats and inter-repeats possesses inherent MT binding, MT assembly and MT dynamics regulatory activities [36-40]. Each tau isoform also possesses either zero, one or two alternatively spliced exons in the N-terminal region of the protein that encodes the "projection domain" that is believed to extend outward from the MT surface ([21, 23, 38, 41]; (see Figure 2-1). Tau isoforms are designated as S (short), M (medium) or L (long), when they possess zero, one, or two projection domain insertions, respectively. Surprisingly, the shortest isoform of tau (3RS tau) showed a much stronger disruption to kinesin action *in vitro* than the longest tau isoform (4RL tau), suggesting that the decrease in kinesin binding affinity and run length was not simply due to physical interference with the fourth MT binding repeat or the projection domains, but had a different structural origin [7, 34].

One important but often overlooked possibility is that tau acts indirectly on axonal transport by modulating MT structure and topology in a manner that affects the ability of kinesin motors to move. Although most biochemical and biophysical assays view MTs as static, inert structures upon which MAPs and motor proteins bind, there is increasing evidence that MT structure is itself dynamic, regulatable, and sensitive to the presence of MAPs, motor proteins and small molecule regulators. For example, both tau and the anti-cancer agent taxol alter

MT protofilament number [6, 42], and both regulate MT dynamics at very low tau:tubulin or taxol:tubulin molar ratios [43, 44]. This suggests that small numbers of bound tau or taxol molecules might stabilize MTs by inducing long range structural alterations in the MT lattice. Long-range interactions have also been suggested to explain how the binding of one kinesin dimer to a MT can promote the directionally biased and cooperative binding of additional motors [45]. Finally, ultrastructural studies have shown that taxol increases the longitudinal intradimer and lateral interdimer bond energies [46], while kinesin binding to α-tubulin increases inter-tubulin dimer contact and axial stability along protofilaments [47].

The sensitivity of MT structure and topology to MAPs and small molecules suggests that there may not be one uniquely stable MT structure, but rather an ensemble of possible structures depending upon the presence of protein and small molecule effectors in solution during and after MT assembly. This is supported by a number of measurements of the mechanical properties of MTs that show that MT stiffness varies considerably under different stabilization conditions [48]. Moreover, these structural and mechanical differences can have functional consequences, as shown by recent work demonstrating that tau loses its ability to regulate kinesin run length on MTs stabilized by GMPCPP [49]. As further evidence for a possible role of MT structure in regulating axonal transport, we recently demonstrated that WT tau modulates kinesin-MT interactions in a 3RS tau versus 4RS tau isoform specific manner [50]. Importantly, we found the kinesin-MT interactions to be independent of tau concentration, ruling out simple steric hindrance mechanisms. Instead, we proposed that MTs assembled by 3RS tau and 4RS tau possess qualitatively different structures that support different kinesin translocation rates. Taken together, these data suggest that MTs may

undergo large length-scale conformational changes in response to various effectors and it is therefore reasonable to suggest that a misregulated MT structure could significantly impact axonal transport.

In this paper, we extend these arguments exploring the role of tau dysfunction in the context of neurodegenerative disease by hypothesizing that mutations in the primary sequence of tau contribute to neuronal dysfunction by assembling/stabilizing MTs with aberrant topology that support altered kinesin-dependent axonal transport. Using a suite of *in vitro* motility assays, we have identified three independent tau mutations (4R P301L, 4R ΔN296, and 4R R406W) that significantly reduce kinesin translocation velocity along MTs relative to WT tau. It is important to emphasize that these effects have been detected in a completely defined, reconstituted *in vitro* system, so the effects must be mediated solely by tau, tubulin and kinesin without any contribution from phosphorylation or other cell signaling pathways. We also find that the presence of taxol can, in many cases, suppress or abolish these mutant tau induced effects. These data provide strong support for the hypothesis that the 4R P301L, 4R ΔN296, and 4R R406W tau mutants contribute to neurodegenerative/dementia diseases by compromising axonal transport, and suggest a possible therapeutic role for taxane-like compounds in treating such diseases.

C. Materials and Methods

1. Purification and Rhodamine Labeling of Tubulin

MAP-free tubulin dimers (>99% pure) were purified from bovine brain in the absence of any stabilizing agents as previously described [51]. Briefly, bovine brain tubulin was purified

from brain homogenates by two cycles of polymerization and depolymerization, followed by elution through a phosphocellulose column. Rhodamine-labeled tubulin (0.14 mole rhodamine per mole tubulin) was prepared by carboxyrhodamine labeling (Molecular Probes) as described [52].

2. Generation and Purification of Recombinant Tau Proteins

Recombinant tau was produced using pRK expression vectors containing cDNA sequences encoding 3RS or 4RS human tau (containing no N-terminal inserts). Site-directed mutagenesis was used to generate all tau mutants used in this study from their corresponding wild type constructs using a Stratagene QuikChange kit. All mutations were verified by DNA sequence analysis (Iowa State DNA Sequencing Facility). In all cases, recombinant tau was isolated and purified essentially as previously described [53] except that the final purification steps consisted of a HiTrap Phenyl HP column (GE Healthcare) followed by dialysis into BRB-80 buffer (80mM PIPES, 1 mM EGTA, 1 mM $MgSO_4$, pH 6.8) supplemented with 0.1% β-mercaptoethanol. The concentration of purified tau was determined by quantitative SDS-PAGE comparison with a tau mass standard [43].

3. Kinesin Expression and Purification

The kinesin construct (K560-CL-his) was a gift from Dr. Ron Vale (UCSF). In a pET expression vector, the cDNA encodes the N-terminal 560 amino acids of human conventional kinesin heavy-chain lacking solvent exposed cysteines but retaining normal enzymatic and motile properties [54]. A single point mutation (T560C) at the C-terminus allows for specific labeling via maleamide-thiol coupling. The C-terminus of this “cys-lite” (CL) construct also

has a hexa-histadine cluster for Ni-affinity purification. K560-CL-his was expressed in BL21 (DE3) cells (Invitrogen), then cells were lysed and kinesin purified as previously described [50].

When prepared for use with quantum dots, the purified kinesin was subsequently labeled with EZ-Link® Maleimide-PEG2-Biotin (Thermo Scientific). When prepared for use in gliding assays, kinesin was typically further purified by a single 'bind and release' cycle using established MT-affinity cosedimentation procedures [55]. In both cases, kinesin was concentrated, supplemented with 10% sucrose and 0.1 mM ATP, drop frozen in liquid nitrogen in single-use aliquots and stored at -80°C.

4. Tau-MT Cosedimentation Assays

Tau-assembled MTs were prepared by mixing MAP-free tubulin at 15 μM with WT or mutant tau at concentrations of 3 μM (1:5 tau to tubulin molar ratio) or 0.5 μM (1:30 tau to tubulin molar ratio) in BRB-80 buffer supplemented with 2 mM GTP. Taxol-assembled MTs were prepared by mixing MAP-free tubulin with taxol (20 μM final taxol concentration; Sigma). Taxol MTs were assembled for 35 min at 35°C, at which time tau was added at 3 μM or 0.5 μM. After a total of 1 h assembly at 35°C, MTs were layered over 180 μL of a 35°C sucrose cushion (50% w/v in BRB-80, 2mM GTP) in a 5×20 mm UltraClear centrifuge tube (Beckman Coulter). Samples were centrifuged in a Beckman TLA 100.3 fixed angle rotor for 12 min at 60,000 rpm (194,000×g) at 35°C. Supernatants and pellets were collected and solubilized in SDS-PAGE sample buffer. The quantities of tau and tubulin in each fraction were determined by Western blotting using the monoclonal antibody Tau-1

(Millipore) and Coomassie blue staining respectively, taking care to operate within the linear detection range. Negligible quantities of tau or tubulin remained within the cushion. These data were used to determine the molar ratio of tubulin to tau in the MT pellet. Statistical analysis of cosedimentation data was conducted using GraphPad Prism Software. Within each assembly condition (1:5 or 1:30 tau:tubulin starting ratio, +/- taxol), data were compared using a one-way ANOVA followed by Tukey's post test. The data reported show the significance of comparisons between mutants and their corresponding WT.

5. Kinesin-Driven MT Gliding Assays

Gliding assays were performed as previously described, with minor modifications [50]. Flow-chambers were constructed using ethanol-cleaned glass coverslips and attached to a glass slide with double-sided tape. Kinesin was diluted to 20–50 μg/ml in BRB-80 buffer containing 10 mM β-mercaptoethanol then flowed into the chamber and allowed to directly adhere to the glass surface for ~3–5 min. Following attachment of motors, the chamber was blocked for an additional 5 mins with a solution of casein to reduce the non-specific binding of MTs to the glass surfaces.

To prepare fluorescent MTs for visualization, rhodamine-tubulin was mixed with unlabeled tubulin on ice at a molar ratio of one labeled tubulin dimer to every 3–5 unlabeled tubulin dimers, and then one of two polymerization methods was used. To generate taxol-assembled MTs, the tubulin mixture was incubated for 5-10 min in a water bath at 35°C. Taxol was then introduced in 3 steps, to a concentration of 1 μM, then 6.5 μM, then 20 μM (final) to prevent formation of non-MT structures [56]. After each addition, the suspension was incubated for

5-10 min at 35 °C. For measurements of taxol-assembled, tau-coated MTs, the appropriate tau protein was then added to a final ratio of 1:5 tau to tubulin, and the MTs incubated at 35ºC for another 15 min. The final tubulin concentration was 20 μM. MTs were then diluted 1:100 in warm motility buffer containing BRB-80, 5 mM ATP, 0.1% β-mercaptoethanol and an enzymatic oxygen scavenger system consisting of glucose oxidase, catalase, and glucose. MTs were flowed into the kinesin-containing flow chamber, which was immediately sealed with vacuum grease. As a control, taxol-assembled MTs were tested in the absence of tau at the beginning and end of each experimental session.

To generate tau-assembled MTs, fluorescent and unlabeled tubulin proteins were mixed with tau at a molar ratio of 1:5 tau to tubulin in BRB-80 buffer supplemented with 2 mM GTP. MTs were assembled for 1.5 hr at 35ºC then diluted in warm motility buffer containing BRB-80, 5 mM ATP, an enzymatic oxygen scavenging system (glucose oxidase (Sigma), catalase (Sigma), and glucose) and 8% glycerol, which helped to stabilize the MTs against depolymerization during data acquisition. The kinesin-containing flow chamber was pre-warmed to 35ºC on a heat block for ~1 min before MT addition and immediately sealed with paraffin wax. Dilution factors were optimized daily to obtain 5–30 MTs per field of view. As a control, WT tau-assembled MTs were prepared daily and tracked in parallel with corresponding mutant tau conditions.

For all gliding assays, data were collected from multiple independent experiments using tau proteins purified from at least two independent preparations.

6. Kinesin-driven Quantum-Dot (QD) Assays

For use in QD assays, taxol-assembled MTs were generated as above, except the incubation time between additions of taxol was extended to 20 min to generate longer MTs. Immediately after the final incubation, the MTs were pelleted in a benchtop centrifuge at 14,000 rpm for 10 min at room temperature to remove unpolymerized tubulin, which contributes to background fluorescence. The pellet was gently resuspended in a stabilization buffer containing 1 mM GTP, 20 μM taxol, and 1 mM DTT in BRB-80, and stored at room temperature, away from light. MTs formed by this method are typically stable for up to one week. QD assays were performed as previously described [57], with modifications. Glass flow-chambers were constructed by attaching plasma-cleaned 22x40 mm #1.5 coverslips to clean glass microscope slides with two parallel pieces of double-sided tape spaced ~5 mm apart. β tubulin antibody (SC-58884, Santa Cruz Biotechnology Inc.) solution (40 μg/mL) was flowed into the chambers to allow absorption to the coverslip surface. After a 10 min incubation, excess antibodies were washed out by addition of 50 μL of BRB-80.

The stock MT solution was diluted 1:20 in BRB-80, supplemented with 10 μM taxol, and 20 μL of the MT solution was then flowed into the chambers. After a 10 min incubation period, 4 mg/mL casein solution was introduced to wash out any unattached MTs, and to passivate any remaining active glass surfaces. After 10 min, biotinylated kinesins, diluted to 20 ng/mL in a solution of BRB-80 supplemented with 10 μM taxol and 1 mM AMPPNP, were introduced to the flow chambers. After 5 min, chambers were washed and Qdot® 605 streptavidin conjugated quantum dots (Q10101MP, Invitrogen), diluted to 0.2 nM in BRB-80 with 10 μM taxol, were introduced. After 5 min chambers were washed with a standard

motility buffer for single-molecule kinesin measurements, consisting of BRB-80 supplemented with 10 μM taxol, 5 mM DTT, 1% β-mercaptoethanol, an enzymatic oxygen scavenger system as well as the desired type and concentration of tau protein (typically 100 nM tau) [57]. The chambers were sealed with vacuum grease and visualized immediately.

Considering the cylindrical geometry of the microtubule (outer diameter of ~ 25 nm) and the size of the QD (diameter ~ 20 nm) there can be no more than 4 motors accessible to any QD that diffused near a microtubule during the QD loading step, and our run length measurements suggest that at least two motors are engaged. Based on our estimates for the molar ratio of polymerized tubulin dimer to kinesin dimer in the observation chamber of approximately 25:1 we believe that on average, 2-3 kinesin molecules are available to bind each QD during complex assembly. Motors are bound to the QD using a biotin-streptavidin linkage, which has a near covalent bond strength, and thus a bond lifetime that is much longer than our experimental observation.

7. Data Acquisition and Analysis: MT Gliding Assay

For taxol-assembled MTs, gliding events were visualized using a Nikon Ti-S microscope equipped with custom-built total internal reflection fluorescence (TIRF) illumination capabilities (100× magnification, 67 nm/pixel, 19-20°C ambient temperature). Excitation wavelength used for rhodamine imaging was 532 nm. Images were collected using an air-cooled EMCCD camera (Andor, iXon) every 0.4 s for 100 frames. MT tracking was performed manually using ImageJ to identify the leading tip of the moving MT in each frame. To calculate velocity, the total MT trajectory length was divided by the time interval over which motion was observed.

For tau-assembled MTs, gliding events were visualized by exciting the rhodamine-labeled MTs at 460 nm. MTs were warmed to 35°C using an objective heater (Bioptechs) and microscope stage warmer (Okolab). A Hamamatsu Orca II digital camera connected to a Nikon Eclipse E800 fluorescence microscope at 60x magnification (106 nm/pixel) was used in conjunction with Metamorph imaging software (Molecular Devices) to capture an image stack of 30 full frame images using a 4 s interval between acquisitions and a 200 ms exposure time (without binning). Velocity measurements were performed using the ImageJ 'Manual Tracking' plug-in (Fabrice P. Cordelieres, Institute Curie, Orsay, France; version 2005/06/15). Only MTs which had plus ends and minus ends visible throughout the entire process of tracking were selected for analysis. Frame to frame velocity was collected for ~20 frames, and then used to calculate an average velocity for each MT.

8. Data Acquisition and Analysis: QD Assay

Motions of single QDs were visualized using a custom-built total internal reflection fluorescence (TIRF) microscope at 100× (magnification = 67 nm/pixel). Images were collected at room temperature using an air- cooled EMCCD camera (Andor, iXon) at a rate of 10 frames per s (full frame transfer). Excitation wavelength used for QD imaging was 488 nm. A broadband emission filter was selected to allow the dim outline of the rhodamine-labeled MT to be observed in the background of the bright QD images. Images were analyzed off-line after data collection. Movies were manually screened to identify the motion of kinesin-driven QDs that warranted velocity analysis. Only runs that persisted for at least 30 frames were analyzed. QD position was determined as a function of time using the built-in

FIONA algorithm available through Video Spot Tracker software (made available by CISMM at UNC-CH, supported by the NIH NIBIB, Award# NIH 5-P41-RR02170).

The initial velocities of the kinesin-QD assemblies were calculated framewise then refined to discriminate between motions that were parallel or perpendicular to the MT axis using a graphic-based analysis algorithm implemented in MATLAB. This was particularly useful for cases in which tau binding disrupted the antibody-MT connection, leading to thermal fluctuations of the MT substrate upon which the kinesin motors walk. For each moving kinesin-QD assembly, a region with a width of 15 pixels was drawn around the trajectory, and the fluorescence intensity over the run duration was accumulated to obtain a single image displaying the average location of the underlying MT track. The MT location was then determined by fitting a Gaussian curve to the cross-section of intensity of the MT contour using ~ 100 evenly distributed points, as previously described [58, 59]. Curve fitting was implemented using built-in curve-fitting algorithms in MATLAB. Using the resulting MT coordinates, the initial velocities were projected into two orthogonal components, one parallel and one perpendicular to the MT contour. The kinesin velocity for a single translocation event (*i.e.,* a single 'run') was given by the mean of the parallel components of the framewise velocities. To determine run length, the total distance moved by each kinesin-coated QD was determined manually using built-in measurement tools in ImageJ.

D. Results

The goals of our work are (i) to determine how disease-linked tau mutants affect the ability of MTs to support kinesin translocation, and (ii) to determine the extent to which these

effects are enhanced or diminished by the presence of taxol. To accomplish these goals, we used two complementary *in vitro* assay geometries. In the MT gliding assay, kinesins are physisorbed to glass coverslips and the motor domains that extend into solution interact with freely diffusing MTs. As a result, MTs are propelled across the surface by a large ensemble of motors acting in concert. Individual MTs are visualized by microscopy and their velocities quantitated. In the quantum dot (QD) assay, small numbers of kinesin dimers (typical 2-3) are bound to QDs in a manner that mimics *in vivo* cargo attachment. In this case, single MTs are immobilized on a coverslip surface using anti-tubulin antibodies in order to promote a natural tubulin conformation. QD movement is visualized by microscopy and their velocities quantitated.

For the gliding assays, we used two different MT preparations - MTs were assembled by either tau alone (without any taxol) or MTs were assembled by taxol and subsequently coated with tau. Traditionally, MT gliding assays have been performed at room temperature and with taxol assembled MTs because taxol confers significant stability upon otherwise dynamic MTs. On the other hand, using tau assembled MTs provides a more biologically relevant condition. Because the absence of taxol reduces MT stability at room temperature, our tau-assembled MT gliding assays lacking taxol were performed at 35°C with the addition of a small amount (8%) of glycerol to suppress MT dynamics. With respect to the QD assay, these were performed at room temperature using taxol-assembled, tau-coated MTs because the antibody used for MT anchoring is unstable at 35°C. Despite this limitation, the measurement of the motions of individual QDs provides important mechanistic insights not available through the gliding assay, including the identification of pauses and the

characterization of cargo travel distance ("run length") as well as variations in cargo velocity. To ensure reproducibility, we repeated each measurement using at least two independent tau preparations for each protein tested, and presented mean velocities that were averaged over numerous independent observations (for more details, see Materials and Methods).

1. Differential effects of 3R WT and 4R WT tau on kinesin translocation in the absence and presence of taxol

Prior to examining mutant tau proteins, we first examined the effects of 3R WT tau and 4R WT tau on kinesin translocation. There is a substantial literature of the effects of WT tau on kinesin motion *in vitro* [7, 28, 33, 34] which our study extends in two important ways. First, we compared the effects of the 3RS and 4RS isoforms of tau, allowing the effects of the two different microtubule binding repeat regions to be assessed when adjacent to the same N-terminal region of tau, *i.e.*, both 3R and 4R tau were examined in the "short" projection domain context. Second, we directly examined the effects of taxol by assembling MTs with and without the drug present. In agreement with our prior work [50], we found that MTs assembled by 3R WT tau glide significantly faster than MTs assembled by 4R WT tau in the absence of taxol (Tables 3-2). Interestingly, for MTs assembled by taxol and coated by tau this gliding rate difference was reversed (Tables 3-2). Additionally, taxol-assembled MTs lacking tau glided faster than those coated with either WT tau isoform.

To gain additional insight into the mechanism of kinesin action, we next tested 3R WT tau and 4R WT tau using the QD assay. In agreement with the gliding assays, kinesin-QD complexes translocated significantly faster along taxol MTs lacking tau than along taxol MTs

coated with either 3R or 4R WT tau (Tables 3-2); however there were no statistically significant differences in kinesin velocity between the 3R WT and 4R WT tau. In no case did we observe obvious periods of pausing or variation in velocity. There were no tau concentration-dependent effects on velocity for either tau isoform at concentrations in the range of 100–1000 nM (data not shown), consistent with previous results [7, 50].

These data demonstrate that the effects of tau on kinesin-driven motility depend sensitively on the MT assembly conditions and also the geometry of the microtubule-kinesin attachment. In the gliding assay, MTs assembled by 3R WT tau support faster kinesin translocation rates than MTs assembled by 4R WT tau; however, for MTs assembled by taxol and then coated with tau, this effect is either absent or reversed. To better understand the influence of taxol and our experimental design, we repeated the MT gliding assay using taxol-assembled tau coated MTs under the temperature and glycerol conditions used in the taxol-free MT gliding assay (*i.e.,* 35°C and 8% glycerol). We found that the differences observed between 4R tau assembled MTs (lacking taxol) and 3R assembled MTs (lacking taxol) previously observed under these conditions disappeared when comparing taxol assembled/tau coated MTs (data not shown). Thus, we conclude that MTs assembled by 3R WT tau and 4R WT tau differentially affect the rate of kinesin translocation, and that this effect can be masked or altered by the presence of taxol.

2. Effects of neurodegeneration-linked tau mutations on the rate of kinesin translocation

Before testing the effects of mutant tau proteins on kinesin translocation, we first assessed the ability of each WT and mutant tau protein used in this work to assemble MTs from

tubulin dimer subunits and to bind to pre-formed taxol assembled MTs using a MT cosedimentation assay. Tau was incubated with either tubulin dimers or taxol assembled MTs at tau to tubulin dimer molar ratios of 1:5 or 1:30, bracketing the approximate physiological range for neurons [60, 61]. In both cases, the four tau mutants P301L, ΔN296, 3R-R406W, 4R-R406W demonstrated similar assembly and binding activities to their corresponding WT constructs (Figure 2-2). Consistent with previous results, we find that the ratios of tau:tubulin present in tau assembled MTs is somewhat higher than the ratios of tau:tubulin in the corresponding initial reaction mixture (especially at lower tau:tubulin molar ratios). This is not surprising since tau binds strongly to MTs but not to free tubulin dimers, and some tubulin remains in solution [50]. Based on these results, we argue that any differences observed in kinesin translocation along MTs assembled by, or coated with, these tau mutants must be due to inherent differences in tau action, rather than the result of differential tau-mediated MT assembly or differential tau binding to taxol-assembled MTs.

To begin assessing the effects of neurodegeneration-linked tau mutations on kinesin translocation, we first tested the effects of tau harboring the P301L point mutation. This mutation maps to exon 10, which is present only in the 4R tau context (Figure 2-1). When using tau-assembled MTs (without taxol), we observed a substantial ~ 33% reduction in gliding velocity of 4R P301L MTs relative to the 4R WT control MTs (Table 3-2). When using taxol-assembled, 4R P301L tau coated MTs, we found a consistent and statistically significant, albeit more modest, reduction (~8%) as compared to the 4R WT control when using the traditional gliding assay (Table 3-2). In the kinesin-QD assay, we observed a

modest but not statistically significant reduction in translocation velocity of kinesin-QDs on taxol MTs coated with 4R P301L tau relative to 4R WT tau.

We next examined the ΔN296 tau mutation, which also maps to exon 10, and is therefore present only in the 4R tau context (Figure 2-1). With the tau-assembled MT gliding assay (without taxol), we observed a substantial reduction in MT gliding velocities (~23%) using MTs assembled by 4R ΔN296 tau relative to MTs assembled by 4R WT tau. In contrast, no differences in gliding rates were observed between taxol assembled MTs coated with 4R ΔN296 and those coated with 4R WT tau using the traditional gliding or kinesin-QD assays.

We next tested the effects of the R406W tau point mutation on kinesin translocation. This mutation maps to the C-terminal tail of tau and is present in both 4R tau and 3R tau (Figure 2-1). Using MTs assembled by tau (without taxol) we found a substantial ~17% reduction in the gliding velocity of 4R R406W tau-assembled MTs relative to 4R WT tau (Table 3-1). Again, this effect was abolished in the traditional gliding assay using taxol-assembled MTs. Surprisingly, the difference between 4R R406W and 4R WT was discernable in the kinesin-QD assay; kinesin-QDs translocated 19% slower along taxol assembled MTs coated with 4R R406W tau relative to taxol assembled MTs coated with 4R WT tau. In marked contrast, none of the three assays revealed any reduction in kinesin translocation rate for the 3R R406W tau mutation, indicating a strong tau isoform-specific effect.

In agreement with our parallel studies with the WT tau proteins, control experiments using each tau mutant demonstrated that the difference between the two MT gliding assays is due

to the presence of taxol, rather than changes in temperature or the presence of glycerol (data not shown). Taken together, our data indicate that MTs assembled by 4R P301L, 4R ΔN296, and 4R R406W tau support slower rates of kinesin translocation as compared to MTs assembled by 4R WT tau. Moreover, we find that the presence of taxol can suppress these effects, and that the magnitude of the suppression appears to be sensitive to the geometry of the assay.

Finally, reductions in kinesin translocation rates were not observed with all tau mutants tested. We found that 4R ΔK280 tau, 4R P301S tau and 4R G303V (Figure S1) all (i) assembled MTs, and bound to taxol MTs, similarly to 4R WT tau (Figure S2) and (ii) did not slow the rate of kinesin translocation rate as assessed using the taxol-free tau assembled MT gliding assay, the assay in which we found the most dramatic effects for the P301L, ΔN296, and 4R R406W mutants (Supplemental Table S1). Specifically, the gliding velocity of 4R P301S tau MTs was statistically indistinguishable from that of 4R WT tau assembled MTs, whereas MTs assembled by either 4R ΔK280 tau or 4R G303V tau supported slightly (~8%) faster gliding speeds than 4R WT tau assembled MTs.

3. Effects of the tau proteins on kinesin-QD travel distance

As another assessment of kinesin translocation, we measured the distance traveled by the kinesin-QDs during single translocation events (*i.e.*, "run length"). This parameter is not measurable using a MT gliding assay, since new motors are continually engaged as the MT glides across the kinesin-decorated surface. In contrast, the QD accommodates a small number of kinesin motors (based on the QD size of ~20 nm, we estimate that 2-3 molecules

of kinesin are typically engaged), and therefore the kinesin-QD run length can be a useful metric when comparing MTs coated with different tau isoforms. Assuming that each motor operates independently, the probability of detachment of cargo from the MT depends on the product of detachment probabilities of each motor [62]. In the case of single kinesin motors moving along bare taxol-stabilized MTs, the probability of detachment is ~ 10^{-2} per step. Given an 8-nm step size, this leads to an average run length of ~ 800 nm. When two motors are simultaneously engaged, the predicted run length increases to 80 μm, much longer than the average MT used in our studies. Consistent with this, in the absence of tau, >90% of the kinesin-QD assemblies bind and translocate to the end of taxol assembled MTs. Therefore, the observed run length of taxol assembled MTs (~ 8 μm; Figure 2-3) is given by one-half of the average MT length, and is a substantial underestimate of the actual run length of the assembly.

In the presence of 3R or 4R WT tau, the percentage of kinesin-QD assemblies that bind and move to the end of the MT drops to ~50%, and the mean run length decreases by a factor of two to ~3.2–3.5 μm (Figure 2-3). This is consistent with prior work demonstrating that WT tau proteins tend to promote kinesin detachment (or inhibit reattachment) [7, 34]. Interestingly, there was a slight increase in run length in the presence of the P301L and ΔN296 mutants, but no significant effect of either 4R R406W tau or 3R R406W tau mutations on run length, all in comparison to their respective WT tau isoforms. These results suggest that velocity decreases for the R406W and P301L mutations observed with the QD assay do not correlate with enhanced kinesin dissociation from the MT.

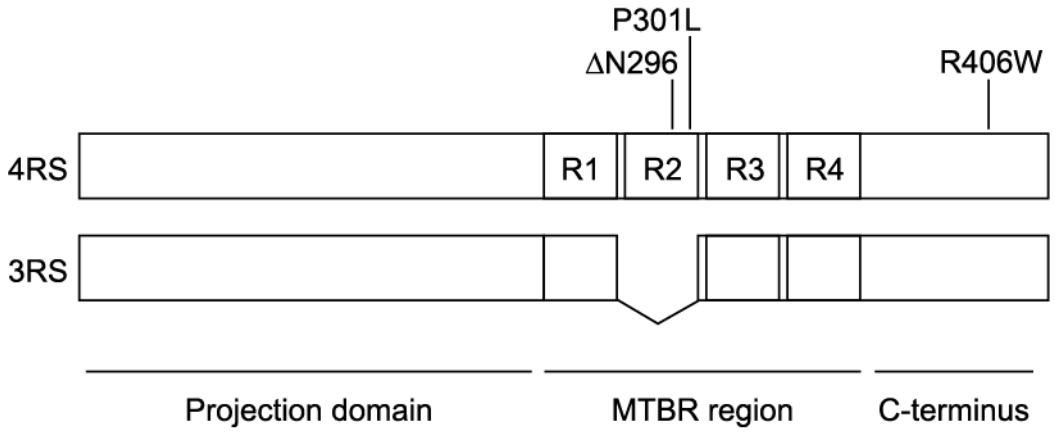

Figure 2-1: Schematic of the two wild-type (WT) tau isoforms used in this study, showing the projection domain, microtubule binding repeat (MTBR) region and the C-terminus of each. These two isoforms differ by the presence (4RS) or absence (3RS) of the alternatively spliced exon 10, comprising repeat two (R2) and the inter-repeat between R1 and R2. All tau proteins used in this study lack the two alternatively spliced exons (exons 2 and 3) in the projection domain, *i.e.,* all were the "short" isoforms. These isoforms are abundantly expressed in both development and maturity. Positions of point mutations that affect kinesin translocation are noted.

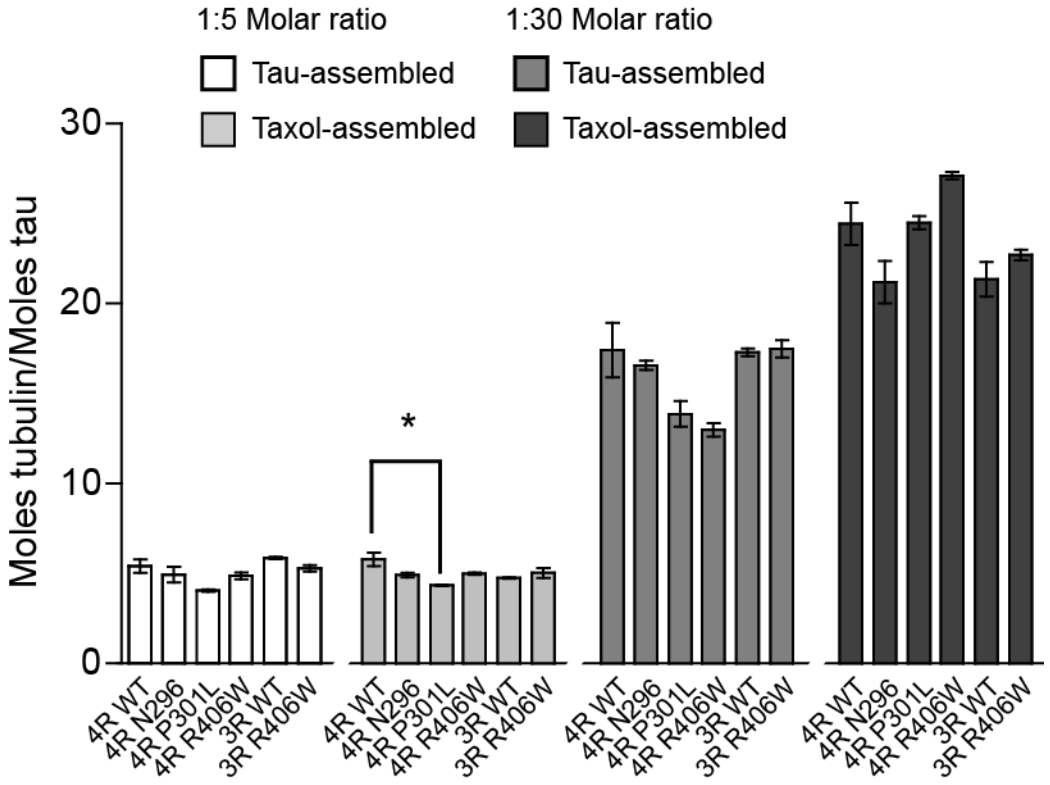

Figure 2-2: Cosedimentation assays comparing the tau:tubulin molar ratio in tau-assembled and taxol-assembled/tau coated MTs achieved by WT and mutant tau proteins. Two tau:tubulin ratios were used to assemble MTs 1:5 and 1:30, which span the physiological range in neurons. Following the assembly reactions, the samples were sedimented, the pellets containing assembled MTs were recovered and then assayed for tau and tubulin content. In each case, mutants were statistically compared with their corresponding WT isoform. Overall, all mutants in a given assay bind with an affinity that is similar to that of their corresponding WT tau, although one difference was statistically significant in one P301L assay at $*P < 0.05$. Error bars are SEM.

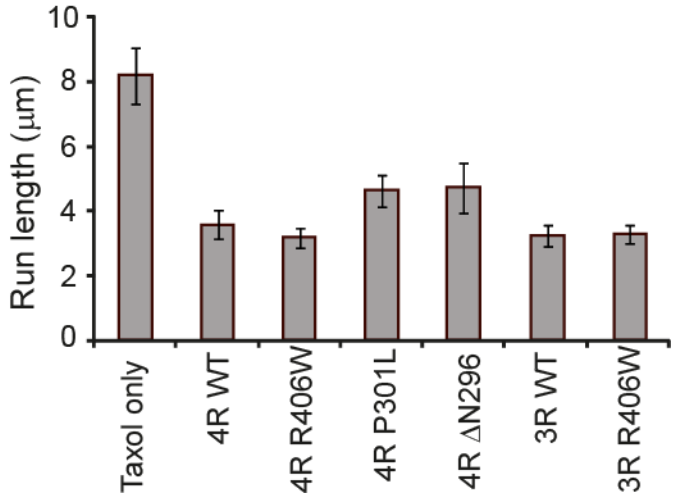

Figure 2-3: Kinesin-QD run length on MTs assembled by taxol and coated with various WT or mutant tau proteins. In control experiments using taxol assembled MTs lacking any tau, the run length was determined by the average MT length, since ~90% of kinesin-QD complexes walked to the end of the MT before dissociating. In the presence of 100 nM tau, the percentage of kinesin-QDs that walk to the end of the MT dropped to ~50%. We did not observe any mutation-dependent reduction in kinesin run length, suggesting that kinesin-MT dissociation is not substantially enhanced in the presence of disease-linked tau isoforms. Error bars are SEM; the number of samples per condition ranged from 24–54.

Table 3-1. Summary of velocity results for all conditions and assays

Assay	Condition	Taxo	*v* (μm/s)	*N*	v_{mutant} / v_{WT}	*p-value*
Gliding	4R WT	−	0.48 ± 0.01	78	—	
	4R P301L	−	0.32 ± 0.02	33	0.67 ± 0.04	<0.001
	4R ΔN296	−	0.37 ± 0.02	53	0.77 ± 0.04	<0.001
	4R	−	0.40 ± 0.01	34	0.83 ± 0.02	<0.001
	3R WT	−	0.54 ± 0.01	55	—	
	3R	−	0.55 ± 0.01	49	1.01 ± 0.02	NS
Gliding	No tau	+	0.36 ± 0.01	354	—	
	4R WT	+	0.32 ± 0.01	155	—	
	4R P301L	+	0.30 ± 0.01	69	0.92 ± 0.09	<0.0001
	4R ΔN296	+	0.32 ± 0.01	75	0.98 ± 0.09	NS
	4R	+	0.33 ± 0.01	76	1.01 ± 0.09	NS
	3R WT	+	0.29 ± 0.01	100	—	
	3R	+	0.32 ± 0.01	57	1.10 ± 0.13	<0.0001
QD	No tau	+	0.43 ± 0.01	93	—	
	4R WT	+	0.33 ± 0.02	38	—	
	4R P301L	+	0.30 ± 0.02	39	0.91 ± 0.08	NS
	4R ΔN296	+	0.36 ± 0.03	19	1.07 ± 0.11	NS
	4R	+	0.27 ± 0.02	57	0.81 ± 0.07	<0.05
	3R WT	+	0.36 ± 0.02	40	—	
	3R	+	0.36 ± 0.02	44	0.99 ± 0.07	NS

N is number of measured MTs or QDs at each condition. All errors are SEM. *P*-values are calculated for each protein that shows a significant difference in velocity using the Student's *t*-test at a 95% confidence level. For each mutant tau, the statistical comparison is made between the velocity measured using MTs assembled by, or coated with, the mutant tau as compared to MTs assembled by, or coated with, WT tau of the same isoform. NS = Not significant. Statistical data comparing the velocities measured using MTs assembled by, or coated with, 3R and 4R WT proteins, or comparisons with the velocity measured using taxol-assembled MTs lacking tau are shown in Table 2.

Table 3-2. Statistical comparison of the velocities for MTs assembled by WT

Assay	Taxol	Condition1	Condition2	p-value
Gliding	+	No tau	3R WT	<0.0001
	+	No tau	4R WT	<0.0001
	+	3R WT	4R WT	<0.0001
QD	+	No tau	3R WT	<0.001
	+	No tau	4R WT	<0.001
	+	3R WT	4R WT	NS
Gliding	−	3R WT	4R WT	<0.001

P-values are calculated for each protein that shows a significant difference in velocity using the Student's *t*-test at a 95% confidence level. In each case, the statistical comparison is made between the velocity measured in "Condition 1" versus the velocity in "Condition 2". NS = Not significant. Velocity data and number of samples are shown in Table 2.

E. Discussion

We sought to test the hypothesis that mutant tau proteins known to cause neurodegeneration and dementia can alter the normal pattern of kinesin translocation along MTs, thereby negatively impacting the essential process of axonal transport. Our strategy was to employ complementary *in vitro* assays composed entirely of defined components, *i.e.,* purified recombinant kinesin, purified recombinant tau (WT or mutant), purified bovine α:β tubulin, and in some cases taxol. This allowed the interactions among just these components to be assessed, without complicating contributions from complex cellular regulatory mechanisms (*i.e.,* phosphorylation). The major observations presented here are (*i*) that kinesin translocates slower along MTs assembled by any of three independent tau mutants (4R P301L tau, 4R ΔN296 tau and 4R R406W tau,) relative to its translocation rate along MTs assembled by 4R WT tau, (*ii*) that the R406W tau mutation has tau isoform specific effects, *i.e.,* while kinesin translocates slower along 4R R406W tau assembled MTs than along 4R WT tau assembled MTs, no such difference is observed between 3R R406W tau and 3R WT tau assembled MTs, and finally (*iii*) that assembling MTs with taxol followed by coating with tau often obscures, and in some cases abolishes, effects of tau mutants that are readily apparent using more physiologically relevant MTs assembled with tau alone. Taken together, these data demonstrate that mutant tau proteins known to cause neurodegenerative disease, including P301L tau, ΔN296 tau and 4R R406W tau, can alter the normal pattern of kinesin translocation along MTs, and provide support for the hypothesis that altered axonal transport could underlie at least one component of tau-mediated neuronal cell death and dementia in the tauopathies. Altered patterns of kinesin translocation could promote cell distress in numerous ways (such as improper distribution of essential proteins/organelles and/or

oxidative stress), which in turn could promote neuroinflammation and subsequent neurodegeneration [63].

One plausible mechanism of differential tau action (WT tau vs. mutant tau; 3R WT tau vs. 4R WT tau) is that MTs assembled by different tau proteins vary in their structures, which in turn affects kinesin translocation. This view is consistent with prior tau structure-function studies. P301L and ΔN296 map to the region of tau that interacts directly with MTs [37, 39, 64, 65]. It is therefore reasonable to suggest that mutant tau assembled and stabilized MTs are structurally and functionally distinct from WT tau-assembled MTs, leading to the slowing of kinesin velocities that we observe. The third mutation, R406W, maps downstream of the region possessing regulatory activities for MT assembly and MT dynamics, and its molecular basis of pathological action is unclear. R406W mutant tau was indistinguishable from WT tau with respect to regulating MT function in a heterologous expression system [66] and in the regulation of MT dynamics either *in vitro* [67] or in cultured cells [68]. These observations led investigators to suggest that R406W might cause neurodegeneration and dementia indirectly, for example, by altering the ability of regulatory kinases and/or phosphatases to interact with nearby phosphorylation sites [66-68]. However, given the fact that our current assay systems contain only purified tau, kinesin and tubulin, our data argue for some kind of direct action by the R406W mutant protein, but only in the 4R tau context. Consistent with tau isoform specific action of the C-terminal region of tau in which the R406W mutation resides, it has been shown that the C-terminal region of tau differentially affects the MT binding capabilities of 3R and 4R tau [69].

The fact that taxol can ameliorate, at least in part, the deleterious effects of mutant tau action is consistent with earlier work demonstrating that taxol induces structural and functional effects upon MTs [42, 44, 46, 70]. Interestingly, taxol and tau have many similar effects upon MTs [40, 44, 53, 64, 71] and data suggests that tau and taxol bind to very close (perhaps overlapping) sites on the inside surface of MTs [4, 72]. Perhaps the presence of taxol serves to complement mutant tau action, inducing structural effects that at least partially compensate for the inability of mutant tau to generate a WT tau structure for MTs? In this regard, it is notable that the MT stabilizing drug epothilone D is under study as a possible therapeutic for Alzheimer's and related dementias [73, 74]. The effect of taxol in the case of the 4R R406W mutation is particularly intriguing since we find that the gliding assay shows no velocity reduction with respect to WT tau in the presence of taxol, whereas the QD assay shows reduction of the same magnitude as was observed using tau-assembled MTs without taxol. The origin of these differences is not yet clear, although it is possible that the 4R R406W mutation causes a conformational change in the C-terminal region of tau creating an unusual MT surface topology, and that small numbers of kinesin molecules (coupled to the QD) are more sensitive to this change than are large groups of kinesin motors (all bound to the MT) in the gliding assay.

The observation that taxol often obscured the effects of mutant tau upon kinesin translocation along MTs is somewhat troubling from a purely experimental point of view, since taxol has been used extensively to study many aspects of MT biochemistry and cell biology. For the vast majority of these studies, it has been assumed that taxol assembled MTs were simply 'generic' MTs. However, there may be subtle, effector-mediated changes in MT structure

that impact MT function in important ways that we are just beginning to understand. It may therefore be prudent to minimize the use of taxol assembled MTs in future work investigating the effects of tau and other MAPs on MT structure and function, and previous work using taxol assembled MTs may require re-assessment for possible taxol-dependent effects.

III. Spectral Analysis Methods for the Robust Measurement of the Flexural Rigidity of Biopolymers[2]

The study in this section was conducted in collaboration with Paul Atzberger's research group, Department of Mathematics, UCSB. All information was published in Biophysical Journal in 2012 [59]. All supplemental materials can be found on publisher's website site.

In this chapter, we will discuss the new and improved spectral analysis method that we developed to robustly measure the flexural rigidity and persistence length of semiflexible biopolymers such as microtubules.

A. Abstract

The mechanical properties of biopolymers can be determined from a statistical analysis of the ensemble of shapes they exhibit when subjected to thermal forces. In practice, extracting information from fluorescence microscopy images can be challenging due to low signal/noise ratios and other artifacts. To address these issues, we develop a suite of tools for image processing and spectral data analysis that is based on a biopolymer contour representation expressed in a spectral basis of orthogonal polynomials. We determine biopolymer shape and stiffness using global fitting routines that optimize a utility function measuring the amount of fluorescence intensity overlapped by such contours. This approach allows for filtering of high-frequency noise and interpolation over sporadic gaps in fluorescence. We use benchmarking to demonstrate the validity of our methods, by analyzing an ensemble of

[2] Reprinted from Biophysical journal 102 (5), Valdman, Yu, et al., Spectral analysis methods for the robust measurement of the flexural rigidity of biopolymers, 1144-1153, Copyright (2012), with permission from Elsevier.

simulated images generated using a simulated biopolymer with known stiffness and subjected to various types of image noise. We then use these methods to determine the persistence lengths of taxol-stabilized microtubules. We find that single microtubules are well described by the wormlike chain polymer model, and that ensembles of chemically identical microtubules show significant heterogeneity in bending stiffness, which cannot be attributed to sampling or fitting errors. We expect these approaches to be useful in the study of biopolymer mechanics and the effects of associated regulatory molecules.

B. Introduction and Background

Cytoskeletal polymers, including actin and microtubules, are stiff, multistranded filaments that are essential to cell organization, motility, and division; to the transport of intracellular cargos by motor proteins; and to the generation and transmission of forces within and across cells. Because of their important role in establishing and regulating cellular mechanics, the elasticity of filaments and entangled cytoskeletal networks has been studied extensively. However, many important questions remain about the relationships between structure and mechanics [75]. In particular, although in vitro measurements of single filament elasticity have consistently shown significant variations in stiffness over roughly an order of magnitude, the molecular origins of these variations are incompletely understood [76-81]. This is largely a result of an inability to distinguish real heterogeneity in elasticity from variations that arise from sources of experimental and statistical uncertainty.

For microtubules (MTs), the stiffest cytoskeletal filaments, distinguishing between signals and noise is particularly challenging because the exhibited bending amplitudes are small and

often of a comparable magnitude to experimental noise. MTs are formed from the head-to-tail polymerization of tubulin dimers in long protofilaments that interact laterally to form a closed tubular structure, with outer diameter of roughly 25 nm [4, 5, 82, 83]. Structural studies have demonstrated that the number of MT protofilaments varies within in vitro and in vivo systems, and can even change along the length of a single MT [84-86]. Because the bending stiffness of a biopolymer scales as the fourth power of its radius, even small changes in the effective radius of the MT could have a large mechanical effect. Under some in vitro conditions, MT stiffnesses appear to depend on both the length and the polymerization velocity, suggesting that lattice shear and structural defects may also play an important role [79, 87-89]. Unfortunately, the large variation in experimental estimates of MT stiffness values has severely compromised our ability to correlate changes in mechanical response and filament composition, and has led to an incomplete understanding of the origins and regulation of MT mechanics.

To help address these issues, we have developed what to our knowledge are new methods to determine and analyze the motions of stiff, isolated, thermally fluctuating biopolymers visualized using fluorescence microscopy. Using approaches from statistical mechanics, we then infer mechanical properties from a spectral analysis of the ensemble of biopolymer configurations at thermal equilibrium. A central challenge in using this approach is the sensitivity of the spectral analysis methods to experimental noise [58, 78]. Previous methods to characterize the fluctuation spectra of biopolymer filaments made use primarily of local information in the fluorescent image, and typically involved three distinct operations: Step 1. Filament tracing to determine biopolymer configurations.

Step 2. Calculation of spectral components from estimated contours. Step 3. Analysis of the spectral components using statistical mechanics to ascertain mechanical properties [58, 78, 79]. Step 1 typically involved interpolating individual configuration points that were determined by manual selection or by local fitting of the cross-sectional intensity profiles of fluorescently labeled filaments [58, 78, 79]. Because each control node is fit independently, any local aberration (such as irregularity in fluorophore labeling or the interference of a nearby physical object) in the image near a control point could have a large influence on the entire fitted contour. Though these approaches have been successfully employed to provide important mechanical information for many types of biopolymers, for the stiffest biopolymers, results vary by roughly an order of magnitude, motivating the development of improved fitting and analysis methods [81, 90].

In this work, we develop a unified approach that combines Steps 1 and 2 into a single procedure, thus minimizing the introduction of errors. This is achieved by representing the biopolymer shape in terms of a contour expanded in an orthogonal polynomial basis. We fit the coefficients of the expansion directly to the fluorescence image by optimizing a utility function that measures the overlap of the entire contour with fluorescence intensity. This global approach is more robust to local disturbances in the fluorescence signal, and allows for the determination of biopolymer shape even in the presence of significant noise and artifacts in the images. To estimate the flexural rigidity of the biopolymer, we develop a statistical mechanics theory based on an energy formulated directly in terms of the coefficients of our spectral biopolymer representation.

Our approach has a number of distinct advantages. The description of the biopolymer by a smooth contour that is fit to the entire image at once naturally handles sporadic gaps in fluorescence intensity along the biopolymer through interpolation, and shows improvement in both filament tracing and determination of persistence length as compared to pointwise tracing. Because these methods are more robust against common sources of experimental noise, it is possible to analyze a larger number of images, giving rise to smaller sampling errors and improving measurement precision. Additionally, we achieve a more accurate description of the biopolymer near the end-points through the use of a basis of orthogonal polynomials. This is in contrast to the use of a trigonometric Fourier basis that implicitly requires a periodic function, and thus a no-curvature condition at the contour end-points to reduce spurious oscillations arising from Gibb's Phenomena [58, 78, 91]. Our method can, in principle, allow for curvature near the end-points, and could potentially facilitate studies of a wider class of biopolymers.

To assess the sensitivity of the proposed methods to experimental noise and sampling error, we introduce a benchmarking approach in which an ensemble of simulated images is generated from simulations of a fluctuating biopolymer with known mechanical properties. We introduce noise and artifacts into the images that are similar to those observed in experimental data. This approach allows for the systematic study of the roles played by different types of experimental noise, and the resultant uncertainty of estimated mechanical properties. The benchmarking approach we propose provides a potentially powerful metric for rating different spectral analysis methods and for understanding the statistical significance of differences reported in experimental results. We then apply the techniques to

an experimental data set of fluorescence images of fluctuating MTs. For even these stiff biopolymers, we find our methods reliably estimate the flexural rigidity and produce modal covariances in agreement with a wormlike-chain (WLC) model for MT mechanics. Interestingly, we find that the level of heterogeneity in persistence length in an ensemble of chemically identical MTs vastly exceeds that predicted from algorithmic error analysis, indicating that significant structural heterogeneity may be present in these samples. We anticipate that these approaches will facilitate the development of more sensitive assays based on the thermal fluctuations of biopolymers, and will enable central questions concerning the molecular origins of cytoskeletal mechanics to be answered.

C. Methodology

1. Variational contour fitting method

In developing this method, we have designed our algorithm for use with images of stiff, isolated filaments, such as MTs, in which a direct determination of the tangent-angle decorrelation function is not possible. Instead, we use information obtained from a description of the biopolymer shape in terms of a curve x(s) of length L, where s ∈ [0,L] is the arc-length parameter of the contour. To measure how well the contour x overlaps with the fluorescence signal of the biopolymer, we use the utility function

$$U[\mathbf{x}, I] = -\int_0^L \int_\Omega k(|\mathbf{y} - \mathbf{x}(s)|) I(\mathbf{y}) d\mathbf{y} ds. \qquad (1)$$

The fluorescence image intensity is given by $I = I(y)$ parameterized over the spatial domain Ω and $k(r)$ is a smoothing kernel vanishing for $r > r_0$. The inner-integral of Eq. 1 gives the average intensity in a region near the location **x**(s) by using the weighting specified by $k(r)$.

The outer-integral collects these values to provide a measure of the total amount of overlap of a contour with the biopolymer fluorescence signal. The convolution by *k(r)* with I filters the high spatial-frequency noise inherent in the image intensity.

We use the following kernel function (see Fig. 3-1), which has a number of desirable properties when used for discrete pixel maps and lattice models (see [92, 93]):

$$k(r) = \begin{cases} \alpha[1+\cos(\pi r/r_0)] & r \le r_0 \\ 0 & r > r_0. \end{cases} \qquad (2)$$

Here, r_0 is chosen to be approximately equal to the width of the imaged polymer. In the case of MTs, with a diameter of ~25 nm, r_0 is taken to be approximately equal to the width of the point-spread function of the microscope. The α is a normalization constant ensuring the kernel function weighting integrates to one.

The contour configuration that minimizes the utility function *U* provides a fit that maximizes the overlap within the image between the contour and the biopolymer fluorescence signal. This minimization requires a representation for the contour amenable to calculations, so we represent the contour by its tangent angle *θ(s)* along the length and by a reference point at the left end-point $\mathbf{x}_0 = \mathbf{x}(0)$. These physically meaningful degrees of freedom uniquely specify the contour curve **x**(s),

$$\mathbf{x}(s) = \int_0^s \boldsymbol{\tau}(\theta(s'))ds' + \mathbf{x}_0. \qquad (3)$$

The tangent vector τ for a given angle q is given by

$$\boldsymbol{\tau}(\theta) = (\cos(\theta), \sin(\theta)).$$

This representation is used to minimize the utility function by evolving the degrees of freedom ($\theta(s)$, $\mathbf{x}_0$) using the steepest-descent dynamical equations

$$\begin{aligned} \frac{\partial \theta(s)}{\partial t} &= -\frac{\delta U}{\delta \theta}(s) \\ \frac{\partial \mathbf{x}_0}{\partial t} &= -\nabla_{\mathbf{x}_0} U. \end{aligned} \tag{4}$$

The term $\delta U/\delta\theta$ denotes the variational derivative of the utility function, which generalizes the usual vector derivative and captures how values change when the entire collection of tangent vectors along the contour are varied [94]. The $\nabla_{\boldsymbol{x}_0} U$ denotes the usual vector derivative in x0 of the utility function.

It can be shown that for all possible variations of ($\theta(s)$, $\mathbf{x}_0$), the direction in configuration space giving the most rapid decrease in the utility function U is the negative of the gradient

$$-\nabla_{\theta(s),\mathbf{x}_0} U = -\left(\frac{\delta U}{\delta \theta}, \nabla_{\mathbf{x}_0} U\right).$$

This motivates the choice for the dynamics, which ensures the contour configuration moves in a manner that steadily decreases the value of U over time. The limiting contour configuration that is stationary under these dynamics has a zero gradient and is a critical point of the utility function U. Such a contour is a candidate for minimizing U [94].

To work with this description in practice, we expand the tangent angles in an orthogonal polynomial basis

$$\theta(s) = \sum_n a_n T_n(s). \tag{5}$$

Each $T_n(s)$ is a polynomial of degree n satisfying the orthonormal inner-product condition $< T_i, T_j >= \delta_{ij}$, where δ_{ij} is the Krönecker delta-function. The T_n values are shown in Fig. 3-2. In

practice, this expansion is truncated after a finite number of terms *N*, allowing for representation up to degree *N* polynomials. Dynamical equations are obtained readily for the coefficients $a_n(t)$ by plugging this expansion into Eq. 4 and projecting the direction of evolution on the polynomials up to degree N (see the Supporting Material).

A particularly useful feature of this coefficient representation is that even when only a finite number of coefficients are used, the contour recovered by Eqs. 3 and 5 has total arc-length L throughout the minimization procedure. Experimentally, this is a very reasonable constraint, as MT length is typically held constant by the use of small molecule inhibitors (such as taxol) during the course of the measurement. Although the total length of the polymer is held constant, the fitted contour can slide freely within the fluorescence signal of the illuminated filament during fitting. In practice, we determine the filament length from the average of the length of the contours obtained from our initial fits, then truncate by a fixed amount (typically by 10–20% of the initial length) to obtain a working length for final fitting. This truncation is implemented to avoid possible high-frequency oscillations that can sometimes arise due to compression of the fitted contour within the polymer after photobleaching has dimmed the fluorescence signal at the polymer ends. Even in the absence of spurious oscillations, the fluorescence signal at the ends of the microtubule tends to be of poor quality. By using a slightly shortened fitting contour, we avoid corrupting the spectral results with MT blurring and other imaging artifacts. Using benchmarking, we have determined the effect of contour truncation on the calculated persistence length, and for the simulated and experimental images analyzed here, the errors are typically <2–3%.

In presenting our approach, we use throughout the Chebyshev orthogonal polynomials defined by

$$T_n(s) = \cos\left(n \arccos\left(\left(\frac{2s}{L}\right) - 1\right)\right)$$

(see Trefethen (21)). This choice was motivated by the ability to take advantage of fast Fourier transform methods; however, other orthogonal polynomial bases could also be used. For more details concerning the particular forms of the variational derivatives used and truncation of the dynamics for a finite number of coefficients, see the Supporting Material.

2. Determining persistence length from the spectrum of biopolymer fluctuations

Using results from equilibrium statistical mechanics, we can estimate the elastic properties of isolated, thermally fluctuating biopolymers [78]. We focus here on determining the persistence length; however, these methods can be applied more generally to other mechanical moduli. To describe the elastic responses of biopolymers, we use the WLC model [95], which associates to a given biopolymer configuration **x**(s) a bending energy

$$E_{bend}[\mathbf{x}] = \frac{EI}{2} \int_0^L \left(\dot{\theta}(s)\right)^2 ds. \qquad (6)$$

The EI denotes the flexural rigidity and $\dot{\theta}(s) = d\theta/ds$ denotes the derivative of the tangent angle in s. For an isotropic elastic structure, EI is the product of the Young's modulus E and the geometric moment of inertia I. At thermodynamic equilibrium, the biopolymer thermal fluctuations have a Gibbs-Boltzmann distribution with the probability density

$$\rho_{bend}[\mathbf{x}] = \frac{1}{Z} \exp\left[\frac{-E_{bend}[\mathbf{x}]}{k_B T}\right], \qquad (7)$$

where T is the temperature, k_B is the Boltzmann constant, and Z denotes the partition function (see Reichl [96]).

Using our representation of the biopolymer configuration **x**(s) in terms of coefficients of the orthogonal polynomial expansion (see Eq. 5), the energy can be expressed as

$$\begin{aligned} E_{bend}[\mathbf{a}] &= \frac{EI}{2}\mathbf{a}^T S\mathbf{a} \\ S_{ij} &= \int_0^L \dot{T}_i(s)\dot{T}_j(s)ds. \end{aligned} \tag{8}$$

The term **a** denotes the composite vector of coefficients with $[\mathbf{a}]_n = a_n$ and S denotes the stiffness matrix of the biopolymer modes. The entries S_{ij} are given by the L^2-inner product of the orthogonal polynomials with index i and j, so the matrix is not necessarily diagonal. For example, for our choice of Chebyshev polynomials the off-diagonal entries of S are nonzero.

The Gibbs-Boltzmann distribution can be expressed using this coefficient representation as

$$\rho_{bend}[\mathbf{a}] = \frac{1}{\tilde{Z}} \exp\left[-\frac{1}{2}L_p\mathbf{a}^T S\mathbf{a} \right], \tag{9}$$

where $L_p = EI/k_BT$ gives the persistence length of the correlations of fluctuations along the contour and $\tilde{Z}$ is the partition function of this representation. Throughout, we treat the metric of the generalized coordinates as constant. In this form, we see that ρ_{bend} has the convenient form of a multivariate Gaussian with mean zero and covariance

$$\left\langle \mathbf{a}\mathbf{a}^T \right\rangle = \frac{1}{L_p}S^{-1}. \tag{10}$$

In our analysis, we find it convenient for finite contours of length L to define a nondimensional persistence length $l_p = L_p/L$. The covariance structure for biopolymer fluctuations derived from the WLC model and Eq. 10 is given by

$$C_{wlc}(\ell_p) = \frac{1}{\ell_p}\tilde{S}^{-1}. \qquad (11)$$

We have used the nondimensional WLC stiffness matrix defined by $\tilde{S} = LS$. This provides a covariance structure predicted by the WLC model when the nondimensional persistence length is l_p.

In experiments, the covariance is estimated by fitting contours to the fluorescence images and estimating modal coefficients. For M samples, the covariance is estimated by

$$C_{exp} = \frac{1}{M}\sum_m \mathbf{a}^{(m)}\mathbf{a}^{(m)T}. \qquad (12)$$

The $\mathbf{a}^{(m)}$ denotes the m^{th} sampled modal coefficient.

A central relation we use to interpret experimental fluctuations of a biopolymer and to infer its mechanical properties is

$$C_{exp} = C_{wlc}(\ell_p). \qquad (13)$$

This expression provides the key link between observed biopolymer fluctuations (left-hand side) and the biopolymer mechanical properties (righthand side). To infer mechanical properties in experiments, we seek to find a value of l_p so that C_{wlc} matches, to a good approximation, the covariance of the experimentally observed biopolymer fluctuations C_{exp}.

This requires minimizing the least-squares error given by

$$V(\ell_p) = \sum_n \left(c_n - \frac{1}{\ell_p} d_n \right)^2. \qquad (14)$$

In principle, any one entry in the covariance matrix could be used to determine persistence length, although it is possible to make use of redundant terms to increase accuracy (because there is sampling error in the coefficients), at the expense of additional computation time. We find in practice that it is sufficient to consider just the diagonal entries, thus the $c_n = [C_{exp}]_{n,n}$ are the diagonal entries of the covariance matrix for the experimentally observed biopolymer fluctuations. The $d_n = [\tilde{S}^{-1}]_{n,n}$ are the coefficients used for representing the covariances obtained from the WLC model (see Eq. 11). The fit for l_p is obtained by minimizing $V(l_p)$ and is given by

$$\ell_p = \frac{\|\mathbf{d}\|^2}{(\mathbf{d} \cdot \mathbf{c})}. \qquad (15)$$

We use composite vector notation for the experimental covariance data $[\mathbf{c}]_n = c_n$ and for the coefficients of the WLC model $[\mathbf{d}]_n = d_n$,

$$\|\mathbf{d}\|^2 = \sum_n d_n^2 \text{ and } \mathbf{d} \cdot \mathbf{c} = \sum_n c_n d_n.$$

We remark that other approaches making use of additional features beyond the covariance matrix of the WLC model could also be used to estimate the persistence length, such as the maximum-likelihood method [97].

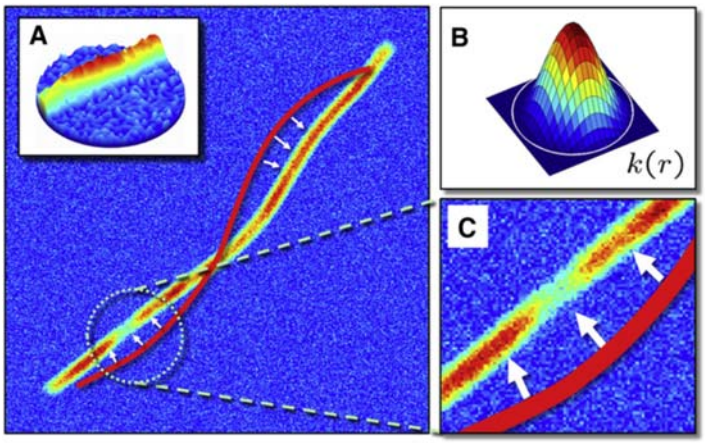

Figure 3-1: Schematic of the methodology. (A) The intensity of the fluorescence signal of the biopolymer (*inset*) and the fluorescence microscopy image being fit by a trial contour (*solid line*). (*Arrows*) Direction of evolution of the trial contour when using the method of steepest descent for the utility function given in Eq. 1. (B) The radially symmetric kernel function *k(r)* having cut-off radius r_0 (*indicated by dotted circle*). (C) Close-up of fluorescence image data within the range of influence given by r_0. In this case, the fluorescence image exhibits gaps in intensity along the biopolymer that are handled naturally by the utility function and the inherent interpolation of the trial contour.

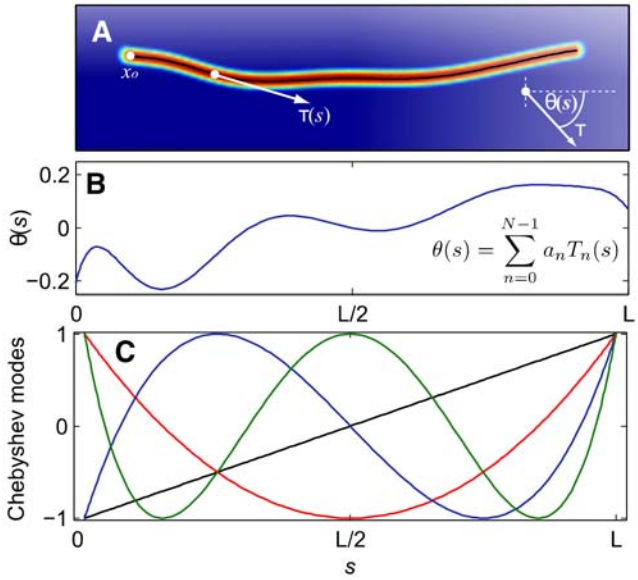

Figure 3-2: Representation of the biopolymer shape using orthogonal polynomials. (A) The contour tracing out the shape of the biopolymer is described by parameterizing the shape using arc-length *s* and the local angle *θ(s)* of the tangent vector t with respect to the x axis. The point x0 is used to uniquely determine the position of the contour. (B) To work with this description in practice, we expand q(s) in an orthogonal polynomial basis to obtain coefficients an. (C) We use the Chebyshev orthogonal polynomial basis for this purpose. The first four nonconstant orthogonal polynomial modes are shown.

C. Results and Discussion

1. Role of sampling error on estimated persistence length

There are two fundamentally independent sources of error to consider for this analysis. The first is the inherent problem of sampling error, where the derivation of mechanical quantities leads to errors due to an averaging over a finite number of experimental observations. The second is the effect of different types of noise in the microscopy images on the estimated values of physical quantities.

To determine the error in the estimated biopolymer persistence length l_p in terms of the number of sampled images M, we assume a biopolymer exhibits fluctuations given by the WLC model, and estimate the covariance using Eq. 12. The sampling error can be expressed as

$$\tilde{C}_M = C_{wlc}(\ell_p) + \boldsymbol{\xi}. \qquad (16)$$

The C_{wlc} (l_p) denotes the covariance structure obtained from the WLC model in Eq. 7. For a sufficient number of samples, ξ is approximately a Gaussian with mean zero and covariance $< \xi\xi^{T} > = \mathrm{Cov}(\mathbf{a}\mathbf{a}^{T})/M$. Expressions for this covariance can be obtained by computing the fourth moments of the Gaussian distribution given in Eq. 7. The tilde notation will be used throughout to distinguish variables that model quantities that would be estimated experimentally.

To simplify the presentation, we assume that the components of $[\mathbf{a}]_n$ can be treated as statistically independent. Additionally, we describe our theory only for estimates of the

diagonal entries of the covariance matrix, which are the only entries used in the least-squares fitting. We denote the diagonal entries of the covariance by the vectors $\tilde{\boldsymbol{c}}_M = \mathrm{diag}(\tilde{C}_M)$ and $\mathbf{c}_{wlc} = \mathrm{diag}(C_{wlc})$.We model the covariance estimates for M samples by

$$\tilde{\mathbf{c}}_M = \mathbf{c}_{wlc}(\ell_p) + \boldsymbol{\xi}. \qquad (17)$$

The ξ denotes a Gaussian with independent components each having mean zero and covariance $\langle \xi\xi^T \rangle = D_M$. The covariance has diagonal entries

$$[D_M]_{n,n} = E[\xi_n^2] = 2[\mathbf{c}_{wlc}(\ell_p)]_n^2/M \qquad (18)$$

with the off-diagonal entries zero.

This model can be used to study how sampling errors from the estimate of the modal covariances $\tilde{\boldsymbol{c}}_M$ propagate into the estimation of the persistence length $\tilde{l}_p$. In particular, from the least-squares fit of Eq. 15, we have

$$\tilde{\ell}_p^{-1} = \frac{(\mathbf{d}\cdot\tilde{\mathbf{c}}_M)}{\|\mathbf{d}\|^2} = \ell_p^{-1} + \sum_n \frac{\xi_n d_n}{\|\mathbf{d}\|^2}. \qquad (19)$$

This shows the estimated inverse persistence length $\tilde{l}_p^{-1}$ is a Gaussian-distributed quantity with mean $\tilde{\mu} = \tilde{l}_p^{-1}$ and variance $\tilde{\sigma}_M^2 = \boldsymbol{d}^T D_M \boldsymbol{d}/\|d\|^4$.

The estimated persistence length $\tilde{l}_p$ has the probability distribution

$$\rho_M(\ell_p) = \frac{\ell_p^{-2}}{\sqrt{2\pi\tilde{\sigma}_M^2}} \exp\left[-\frac{(\ell_p^{-1} - \tilde{\mu})^2}{2\tilde{\sigma}_M^2}\right]. \qquad (20)$$

Note that this distribution is not Gaussian; instead, it has long-tails as a consequence of the $\tilde{l}_p^{-2}$ term and yields an infinite variance. For different values of *M*, this distribution is shown in Fig. S1 in the Supporting Material.

The non-Gaussian form of the distribution requires that some care is taken when characterizing how the sampling errors influence the estimated value of $\tilde{l}_p$. We can no longer make use of the standard deviation to give the magnitude of errors because the second moment is infinite. Instead, we use a confidence interval based on the above probability distribution ρ_M. Interestingly, although the second moment is infinite, the distribution ρ_M can be well approximated by a Gaussian distribution for M sufficiently large ($M > 100$; see Fig. S1). Through an asymptotic analysis of Eq. 20, as M becomes large, we find ρ_M is approximated by a Gaussian with mean $\mu = l_p$ and variance $\sigma_M^2 = l_p^4 \tilde{\sigma}_M^2 = l_p^4 \boldsymbol{d}^T D_M \boldsymbol{d} / \|\boldsymbol{d}\|^4$. This can be used in practice to obtain confidence intervals for errors in estimates of $\tilde{l}_p$.

2. Generating simulated fluorescence images with controlled levels of noise and artifacts

To investigate effects of image noise on persistence length determination, we develop a systematic benchmarking approach, in which we generate an ensemble of simulated images from the fluctuations of a simulated biopolymer with known mechanical properties. We introduce in these images simulated background noise and other artifacts.

We then use our contour tracing and spectral analysis methods to determine the persistence length. A comparison of the measured and actual persistence lengths provides a well-controlled test for the reliability of the proposed methods, and enables experimental conditions to be optimized to improve measurement precision and accuracy.

To generate noise and artifacts similar to those encountered in experiments, we consider primarily two types of noise: 1), background noise in which randomly varying levels of intensity are seen throughout the image, and 2), sporadic gaps in which intensity varies in the

fluorescence signal along the biopolymer. The background noise is motivated by contributions from ambient light sources and out-of-focus fluorophores, whereas gap artifacts are motivated by the uneven binding of fluorescent labels along the biopolymer, inherent fluorescence excitation inefficiencies, and stochastic photobleaching.

To simulate the configurations of a biopolymer having a specified persistence length, we generate modal coefficients for our orthogonal polynomial representation of the contour using the multivariate Gaussian distribution with mean zero and covariance given by Eq. 10. Throughout our presentation, we use $l_p = 10$ and calculate values for the first eight modes ($N = 8$). To obtain an image with a fluorescence signal for the biopolymer of thickness r_0, we use the kernel function of Eq. 2 to trace along the biopolymer contour. For convenience, we normalize all fluorescence intensity values to lie between zero and one. We have also simulated filament contours using a random walk generator, and we find no significant differences in algorithm performance, thereby verifying that there is no bias introduced when generating the contours by using the Chebyshev basis.

To introduce background noise, we perturb each pixel value using two different Gaussian distributions. For pixels that are located on the contour, we perturb by a random value having mean $\mu_c = 0$ and variance σ^2_c. For pixels not located on the contour, we perturb using mean $\mu_b = 0$ and variance $\sigma^2_b = \sigma^2_c$. To characterize the noise, we define I_c to be the characteristic intensity difference between the contour and background $I_c = \langle I(y)\rangle_c - \langle I(y)\rangle_b$, where $\langle\cdot\rangle_l$, $l \in \{b, c\}$ gives, respectively, the average of intensity values over the contour or background pixels. To characterize the level of background noise in our images, we use the ratio σ_b/I_c.

To introduce gap noise along the contour, we modulate the fluorescence signal by a weight function obtained from a cosine series

$$c(s) = \sum_{k=0}^{K-1} w_k \cos\left(\frac{2\pi k s}{L}\right).$$

The random weight coefficients w_k are chosen so that the integral of $c(s)$ over $[0,L]$ has mean mg and variance σ^2_g. The form of c(s) necessitates that $w_0 = \mu_g$. To achieve a variance proportional to σ^2_g, we use $(w_1,\ldots,w_{K-1})$ uniformly distributed over the surface of a K-1 dimensional sphere of radius $\sqrt{2}\sigma_g$. To control how oscillatory the gap artifacts appear in the image, we vary the number of modes K. The random coefficients ensure random amplitude and phases for each of the modes, creating an irregular, realistic gap pattern. We find that K = 25 provides a modulation that agrees well with what is seen in experimental fluorescence images. To characterize the level of gap artifacts in our images we use the ratio σ_c / μ_g.

3. Benchmarking studies for different levels of noise and artifacts

To investigate the robustness of our methodology, we numerically generate ensembles of fluorescence images with prescribed noise conditions, similar to those observed in experiments (see Fig. 3-4). In contrast to prior works that have modeled the role of noise on fitting using theoretical assumptions [78], this benchmarking approach provides a direct and realistic comparison with actual microscopy data. The ensembles contain M = 1000 images, simulating the thermal fluctuations of a biopolymer with persistence length L_p = 9.45 L, where L is the polymer length (taken to be ‘‘1’’ in arbitrary units). To minimize the effects of sampling errors in these studies, we use the same underlying configurations for the simulated biopolymer to generate each ensemble of images. A sample image from each of these ensembles is shown in Fig. 3-3.

To initialize the contour tracing routine, an initial contour is chosen as the diagonal of a bounding box that encloses the Z brightest pixels (Z is typically chosen to be 2500). Because our algorithm is optimized to identify stiff, isolated filaments, the bounding box is automatically drawn around the filament of interest. We calculate the average intensity at each corner, and choose the diagonal that connects the two brightest corners as our initial contour for fitting. This diagonal typically overlays the actual filament, with numerous points of intersection and the length of the diagonal is roughly equal to the actual filament length.

To determine the effect of initial conditions on filament tracing, we tested 300 perturbations to the best initial fit of a single noisy numerically generated fluorescence image, then recorded the maximal difference between the final fit and the actual filament position to determine the robustness of our tracking algorithm. For the perturbations, the angle of the initial fit was chosen to lie within a range of $[-\pi/8, \pi/8]$ around the actual filament position, whereas the midpoint was independently perturbed to lie within a circle of radius 20 pixels from the actual center. For noise levels, we chose values that were similar to those observed experimentally. Of these, 90% of the initial fits converged to within two pixels (maximal deviation) of the correct contour, whereas 5% fit a portion of the filament well but failed to track the filament ends, and another 5% were drawn in regions dominated by noise and thus failed to converge to anything reasonable. This reproducibility demonstrates that our steepest-descent algorithm requires only a single point of intersection between the initial contour and fluorescence signal of the polymer to reliably trace the polymer shape.

Using an unperturbed initial fit, we find that in the absence of any explicitly introduced background noise or gap artifacts, our methods yield an estimated nondimensional persistence length of $\tilde{l}_p$= 9:38. We use this value (which is well within the expected range given our sampling error of 5.2% for M = 1000 images) as our reference when reporting relative errors to remove the baseline sampling error from the reported results and better reflect the differences in the levels of noise and artifacts in the images. For each simulated ensemble of images, we performed the spectral analysis using the initial five Chebyshev modes, which, for the stiff filaments we consider here, represent physically meaningful fluctuations. We report the results of the spectral analysis using our methods for each of the image ensembles in Table 2-1. When performing fits, we find that introduction of noise and gap artifacts can, in a small number of cases, result in images of insufficient quality. For such images (typically <5% of the ensemble), the contour fitting does not converge in a manner that is independent of the initial trial contour. These images are ignored when estimating the modal covariances and persistence length. In the case of experimental data, there is an initial manual review of images to eliminate those which show significant blurring of the filament contour or the presence of a very large interfering object. Additionally, we use only those mode variances that lie within ≈ 3 standard deviations of the mean, to eliminate the possibility that a rare fitting artifact could disproportionately change our stiffness results. In practice, very few images (<10%) are rejected based on these criteria.

As shown in Table 2-1, our global fitting approach enables robust determination of persistence length, even in the presence of substantial background noise and gap artifacts, which are frequently encountered in experiments. We find relative errors for the estimated persistence length to be <1% for a majority of low-to-moderate noise cases, and <10% even

for the largest background and gap noise levels probed. We find similarly good agreement for simulated filaments that are an order-of-magnitude stiffer and tested using an even larger range of gap and background noise conditions and sample sizes (see Table S3 in the Supporting Material).

To further demonstrate the level of improvement in filament tracing and persistence length determination in comparison to more conventional approaches, we generated and analyzed ensembles of 500 images of filaments with known stiffness, and subjected them to known noise-background and gap-noise artifacts. To assess the quality of contour fitting, we used two methods: the global contour tracing routines described above, and a pointwise fitting routine in which the filament position was determined by fitting a Gaussian distribution to the cross-sectional intensity profile of the filament at 200 points along the contour. We compared the coordinates outputted from each fit routine (x_{fit}, y_{fit}) to the coordinates used to generate the filaments (x_o, y_o) and calculated the root mean square (rms) error at each pixel position to be

$$E_{rms} = \sqrt{(x_{fit} - x_o)^2 + (y_{fit} - y_o)^2}.$$

For both fitting methods, we found the mean value of E_{rms} to be <1 pixel; however, we find the fit errors to be substantially lower when using our global fitting routine (as shown in Table S1). We see a factor-of-2 improvement in contour fitting under low noise conditions, and a 10–20% improvement in even the noisiest cases. To complete the comparison, we then input the filament coordinates determined via pointwise fitting into a Fourier-based spectral analysis routine. We found reasonable agreement with the known persistence length (<10% deviation) for all noise levels when using only the first Fourier mode. However, we found the

higher modes to be unreliable, particularly under levels of high background and gap noise (see Table S2). Noise corruption in the higher modes limits the use of averaging to improve measurement accuracy and prevents the identification of deviations from WLC behavior. The ability to average the response of the higher-order modes, each of which fluctuates independently, is particularly important, as sampling error dominates measurement uncertainty in many cases.

4. Experimental results for microtubules

To demonstrate our approach in practice, we apply our filament tracing and spectral analysis methods to characterize the persistence length of an isolated microtubule (MT) imaged using total internal reflection fluorescence microscopy. The MT was labeled with rhodamine dyes to enable visualization, and confined to move within a thin, well-sealed sample chamber to ensure that the fluctuating filament remained in focus throughout the experiment and only thermal forces acted upon the MT. The MTs were polymerized in the presence of the stabilizing compound taxol, rendering their length constant over the time course of the measurement, which is typically limited by fluorophore bleaching to be <100 s. The experimental details are further described in the Supporting Material.

MTs were visualized using an electron-multiplying charge-coupled device camera in full frame transfer mode at a frame rate of 10 Hz and using an exposure time of 0.1 s, which is comparable to the relaxation time of the slowest hydrodynamic mode. To verify that filament motion during this exposure time was not influencing our measurement, we reduced the exposure time to 0.066 s or 0.033 s (at a fixed frame rate of 10 Hz), and found no obvious

trend in our persistence length data that would indicate a systematic bias. We did, however, find that image noise increased substantially for shorter exposure times, with an ~40% increase in background noise for the 0.033-s exposure time as compared to the 0.1-s exposure time. A smaller fraction of images have convergent fits under these high noise conditions, consistent with the benchmarking results shown in Table 2-1.

As a test of our approach, an ensemble of M = 147 fluorescence microscopy images was analyzed using our contour fitting method and least-squares estimator to analyze the first four modes. From these, we determine a nondimensional persistence length of $\tilde{l}_p$ = 176.6 using the spectral characteristics of the fluctuating filament (see Fig. 3-4). In this test case, the MT contour length was estimated to be $\tilde{L}$ = 19.6 μm. This gives an actual dimensional persistence length of $\tilde{L}_p$ = 3.45 mm. To determine the uncertainty in this measurement, we consider errors arising from both sampling and image artifacts.We estimate the sampling error when using only M = 147 images to be ±0.48 mm in $\tilde{L}_p$. From analysis of the experimental fluorescence images, we estimate an average effective background noise of σ_b/I_c = 0.143 and average effective gap noise of σ_g/μ_g = 0.184. From the results of a benchmarking study performed under similar noise conditions, we estimate the contribution to $\tilde{L}_p$-uncertainty to be ±0.2 mm. We anticipate that the uncertainties due to sampling errors and noise artifacts behave in a fairly independent manner. Under this assumption, the total uncertainty can be estimated by adding these two contributions in quadrature. Therefore, we estimate $\tilde{L}_p$ = 3.45 ± 0.52mm.These results represent a measurement uncertainty of ≈ 15%. Our measured persistence length is well within the range of previously reported values [81, 90]. The dashed black line in Fig. 3-4 shows the variances for the Chebyshev modes predicted using a WLC

model with the same mean bending stiffness. Although deviations from WLC behavior have been reported for short MTs, for the range of MT lengths (≈ 8–20 μm) reported here, we find the predicted good agreement between the WLC model and our spectral data, for at least six independent modes [98]. This validates our fitting algorithm under experimental conditions and relatively small sample sizes.

We then applied this method to the study of an ensemble of 54 different MTs, generated under chemically identical conditions, and subjected to identical temperature, storage, and handling conditions. For each MT, ~300 images were analyzed to determine the single-filament persistence length. Given the image noise and sampling errors, we would predict a measurement uncertainty of ≈ 10%. As shown in Fig. 3-5, we measure a much larger range of persistence lengths, indicating that real sample heterogeneity, not image processing uncertainty, is driving this broad distribution. Within this large variation, we find the persistence length to be independent of the filament length, for the range of lengths (10–20 μm) studied here (see Fig. S2).

In the limit of homogeneous isotropic materials at fixed ambient temperature, the persistence length depends only on the Young's modulus E, contour length L, and filament radius, r. L_p varies linearly with E, which has been found to be in the range of 2-3 GPa for a wide range of proteins, including tubulin and actin, likely due to van der Waals interactions along the protein backbone [99]. By contrast, L_p varies as r^4, indicating that even small polydispersity in MT radius could give rise to substantial variations in stiffness. Interestingly, MTs have been shown to form with variable numbers of protofilaments both in vivo and in the presence

of taxol in reconstituted systems [42]. Thus, we favor a model in which an ensemble of MTs with differing radii give rise to a broad distribution of MT persistence lengths. A less likely possibility, in our view, is that the assumption of homogeneity and isotropy fails under some conditions, in which case it is more difficult to relate changes in L_p to a molecular mechanism. We would expect that in this limit, the fluctuation spectra would not follow a WLC model, so we would argue that the assumption of homogeneity and isotropy is appropriate in our analysis.

Table 2-1: Results for the simulated ensembles of fluorescence images

Gap noise	L_P	% Err	% Conv	L_P	% Err	% Conv	L_P	% Err	% Conv	L_P	% Err	% Conv
0	9.38	0.00	100	9.34	0.48	100	9.37	0.10	100	10.1	6.99	98
0.125	9.39	0.07	100	9.36	0.22	100	9.42	0.43	99	9.84	4.66	98
0.25	9.39	0.15	99	9.38	0.03	99	9.45	0.77	98	10.2	8.22	96
0.5	9.43	0.55	94	9.42	0.45	94	9.71	3.35	93	10.6	10.7	89
						Background noise						
		0			0.125			0.25			0.5	

To test the robustness of our spectral analysis methods, we simulated ensembles of fluorescence images with varying levels of background noise and gap artifacts generated from the fluctuations of a simulated biopolymer with known persistence length, $L_p = 9.45\ L$, where L is the polymer length (taken to be ‘‘1’’ in arbitrary units). At each condition we use $M = 1000$ simulated images. To simulate the configurations of a biopolymer having a specified persistence length, for each image we generate modal coefficients for our orthogonal polynomial representation of the contour using the multivariate Gaussian distribution with mean zero and covariance given by Eq. 10. We calculate values for the first eight Chebyshev modes ($N = 8$). We report the relative errors (% Err) in these estimates and the percentage of images found to be of sufficient quality to allow for convergent fits independent of the initial trial contour (% Conv). Relative errors are reported with respect to the baseline case of no background noise or gap artifacts. The table indices correspond to the same ordering and ratios used for characterizing the ensembles of images shown in Fig. 3-3.

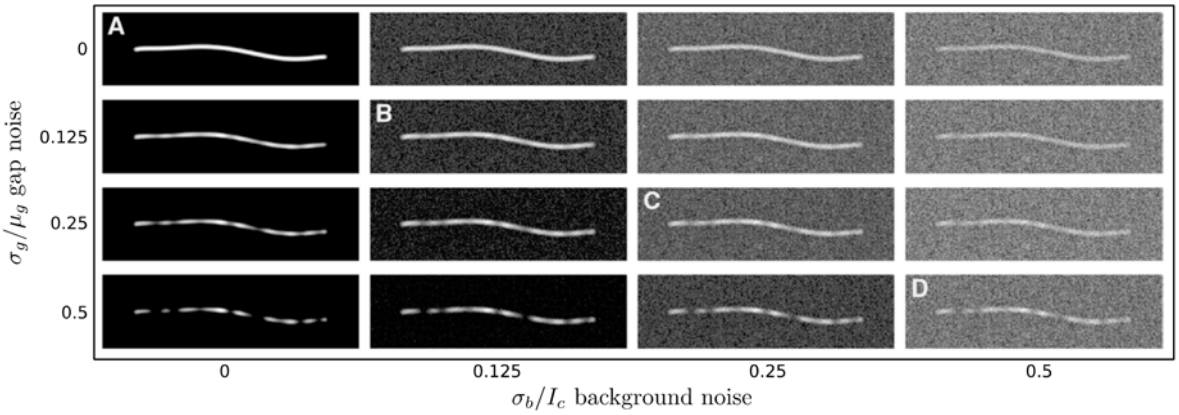

Figure 3-3: Ensembles of simulated fluorescence images. To investigate our spectral analysis methods when subjected to the types of noise and artifacts found in experimental images, we simulate ensembles of images from a simulated biopolymer with known mechanical properties. Shown here are images generated from biopolymer configurations using our contour representation with $l_p = 10$, $N = 8$. The ensembles correspond to different levels of background noise throughout the image and gap artifacts along the biopolymer contour. The background noise increases left to right while the gap artifacts increase from top to bottom. The level of background noise is characterized by the ratio σ_b/I_c for the perturbed background pixel standard deviation σ_b and the average difference of intensity between the contour and background I_c. The level of gap artifacts is characterized by the ratio σ_g/μ_g obtained by integrating the random cosine modulations used to generate the artifacts to obtain an effective mean mg and standard deviation σ_g.

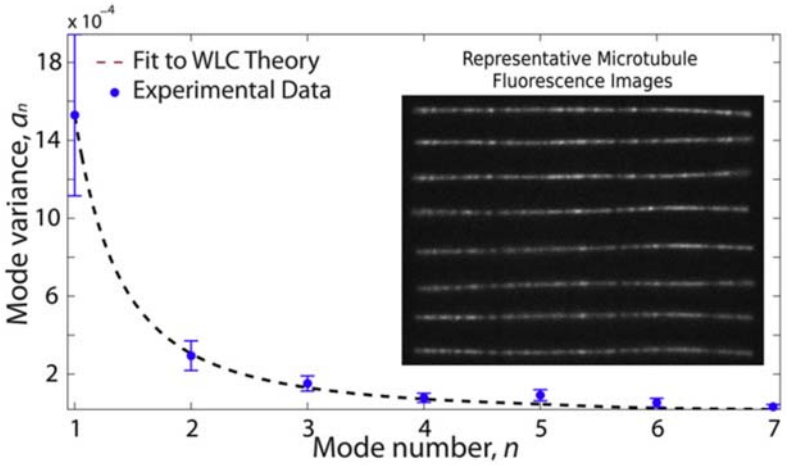

Figure 3-4: Experimental results for a microtubule. We analyze, using our spectral analysis methods, the thermal fluctuations of a microtubule for $M = 147$ images. (Inset) Exhibited thermal fluctuations in the microtubule shape. The exhibited modal covariances of the microtubule fluctuations agree well with a WLC model (dashed line). The error bars correspond to the 95.5% confidence intervals using our sampling error analysis in Role of Sampling Error on Estimated Persistence Length (see main text). Our methods yield an actual dimensional persistence length of $\tilde{L}_p = 3.45 \pm 0.52$ mm.

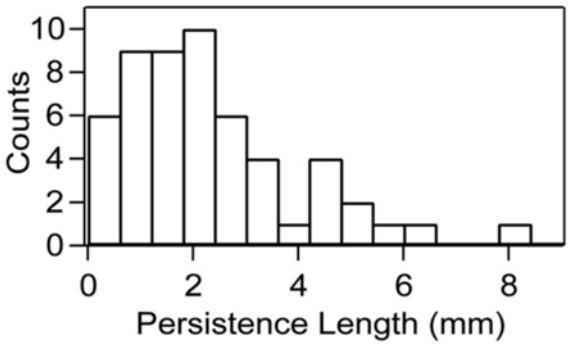

Figure 3-5: Experimental results for an ensemble of microtubules. Histogram of the persistence lengths of an ensemble of 54 different MTs, generated under chemically identical conditions, and subjected to identical temperature, storage, and handling conditions. For each MT, ~300 images were analyzed to determine the single-filament persistence length. Given the image noise and sampling errors, we would predict a measurement uncertainty of ≈ 10%, yet we measure a much larger range of persistence lengths, indicating that real sample heterogeneity, not image processing uncertainty, is driving this broad distribution.

D. Summary

We present what to our knowledge are new spectral analysis methods for the measurement of biopolymer flexural rigidity from observations of the biopolymer thermal fluctuations. Our approach was based on global fitting of an entire trial contour at once to the fluorescence image. We used a contour representation expressed in terms of the curve tangent angles parameterized by arc-length and expanded in a basis of orthogonal polynomials. Using this representation, we performed statistical analysis of the modal coefficients to infer a flexural rigidity for the biopolymer. Our spectral analysis methods were found to work very well even in the case of images exhibiting significant background noise and gap artifacts. The benchmarking approach we propose provides a potentially powerful metric for rating different spectral analysis methods and for understanding the statistical significance of differences reported in experimental results. Our data indicate that these spectral analysis methods provide a substantial improvement in precision for measurements of stiffness based on observed fluctuations of a biopolymer. We expect these approaches will enable future studies of the differential effects of polymerization conditions and the binding of various regulatory molecules on microtubule mechanics.

IV. Mechanical and Functional Properties of Epothilone-stabilized Microtubules[3]

This work was published in Cytoskeleton in 2013 [100]. All information in this chapter and additional supplemented materials can be found on publisher's website.

This section will discuss the effect of the MT stabilizing drugs epothilone-A and epothilone-B on both the mechanics of microtubules and functional transport properties of kinesins moving on these microtubules.

A. Abstract

Using a suite of biophysical tools, we assess the mechanical, structural, and functional properties of microtubules stabilized by the chemotherapeutic compounds epothilone-A, epothilone-B, and taxol *in vitro*. We demonstrate that microtubules stabilized by epothilone-A or epothilone-B are competent to bind tau proteins, and support kinesin translocation. Kinesin speed is sensitive not only to the type of small molecule stabilizer used, but also to the presence of the essential microtubule-associated protein tau. Epothilone-stabilized microtubules are substantially less stiff than taxol-stabilized microtubules. The addition of tau proteins to microtubules stabilized by either epothilone compound or taxol further reduces stiffness. Taken together, these results suggest that small molecule stabilizers do not simply stabilize a 'native' microtubule structure, but rather they modulate the structure, function, and mechanics of the microtubules they bind. This may have important consequences to the therapeutic use of these agents in cancer chemotherapies.

[3] Reprinted from Cytoskeleton 70 (2), Yu, et al., Mechanical and functional properties of epothilone-stabilized microtubules, 74-84, Copyright (2013), with permission from John Wiley and Sons.

B. Introduction

Taxanes and epothilones are potent chemotherapeutic drugs that target a broad spectrum of solid mass tumors by inhibiting microtubule (MT) dynamics, arresting mitosis, and inducing cell death [101-103]. Although these compounds are effective in reducing tumor size and improving survival rates, they can generate disabling and dose-limiting neuropathic side-effects, including pain and loss of sensation, which limit their clinical use [104-107]. The molecular basis of these effects is poorly understood, and as a result there are no approved therapies for the prevention or mitigation of chemotherapy-induced peripheral neuropathy (CIPN) [107, 108]. Onset of symptoms not only reduces quality of life, but impacts health and survival due to treatment delays and discontinuations. Interestingly, axonal dysfunction has been observed within the first month of treatment, well before the typical onset of pain symptoms [109]. This raises the possibility that MT-based kinesin transport and/or the MTs themselves may be altered by the stabilizing compounds, and more importantly, suggests that early or prophylactic interventions might be possible, if quantitative, predictive models of the molecular mechanisms of CIPN were known.

Although taxol-stabilized MTs have been used extensively in *in vitro* measurements of microtubule stiffness and kinesin-based motility, there have been very few reports of the effects of other anti-cancer therapeutics [7, 34, 78, 80, 110]. To address this, we use *in vitro* assays to directly measure the stiffness of, and the rates and patterns of collective kinesin translocation along, MTs that have been assembled by a variety of small molecule stabilizers and coated with the essential MT-associated protein (MAP) tau [9, 59].

Tau is a neural MAP that binds to MTs, promotes tubulin polymerization, regulates MT dynamics, and is essential for the normal development and maintenance of the nervous system [8, 26-29, 111-117]. Through alternative RNA splicing, a single tau gene produces six different tau isoforms, each of which possesses either three or four imperfect repeats in the C-terminal half of the protein ('3R tau' or '4R tau'), separated from one another by shorter inter-repeats [21, 23, 35]. In addition, each tau isoform possesses either zero, one or two inserts in the N-terminal portion of the protein [21, 23, 38, 41].

In this study, we focus on the 'short' tau isoforms with zero N-terminal inserts (referred to simply as '3R' or '4R' herein), which are abundantly expressed in neurons, and have strong MT binding and regulatory activities [7, 34]. We demonstrate that MTs stabilized by epothilone compounds bind tau proteins with affinities that are similar to those of taxol stabilized MTs. However, we find that epothilone-stabilized MTs are softer than taxol-stabilized MTs, and that they support slower rates of kinesin translocation when cargos are moved in the presence of tau.

C. Materials and Methods

1. Tubulin preparation and microtubule assembly

MAP-free tubulin dimers (>99% pure) were purified from bovine brain without stabilizing agents as previously described [51]. Briefly, tubulin was purified from brain homogenates by two cycles of polymerization and depolymerization, followed by elution through a phosphocellulose column. Rhodamine-labeled tubulin (0.14 mole rhodamine per mole tubulin) was prepared as described [52]. MTs were prepared by mixing 20 μM of MAP-free

tubulin and rhodamine-labeled tubulin mixed at a molar ratio of 5:1, with taxol, epothilone-A or epothilone-B (Sigma Aldrich) in PEM80 buffer (80 mM PIPES, 1 mM EGTA, 4 mM $MgCl_2$, pH 6.9) supplemented with β-mercaptoethanol and 2 mM of GTP. MTs were assembled at 35° C with an initial 10 minute incubation, then epothilone-A, epothilone-B, or taxol was introduced in 3-steps, to a concentration of 1 μM, then 6.5 μM, then 20 μM (final) with 20 minute waiting periods between each addition (total reaction time is 70 minutes). This step-wise addition is commonly used when generating taxol-assembled MTs to prevent formation of non-MT structures and promote long MTs [56]. The total tubulin concentration in the resulting stock MT solution is 20 μM.

2. Protein Expression and Purification

The kinesin construct (K560-CL-his) was a gift from Dr. Ron Vale (UCSF). In a pET expression vector, the cDNA encodes the N-terminal 560 amino acids of human conventional kinesin heavy-chain that lacks solvent exposed cysteines but retains normal enzymatic and motile properties [54]. A C-terminal hexa-histadine cluster allows for Ni-affinity purification. K560-CL-his was expressed in BL21 (DE3) cells (Invitrogen), and purified as previously described [50]. When prepared for use with quantum dots, the purified kinesin proteins were subsequently labeled with EZ-Link® Maleimide-PEG2-Biotin (Thermo Scientific) via maleimide-thiol coupling. In both cases, kinesin was concentrated, supplemented with 10% sucrose and 0.1 mM ATP, drop frozen in liquid nitrogen in single-use aliquots and stored at -80°C.

Tau-encoding plasmids and expressed proteins were a gift of Dr. Stuart Feinstein, UCSB. Tau (>99% pure) was recombinantly produced using pRK expression vectors containing cDNA sequences encoding 3-repeat or 4-repeat human tau containing no N-terminal inserts (which we refer to as 3R or 4R tau herein). Recombinant tau was purified as previously described except that the final purification steps consisted of a HiTrap Phenyl HP column (GE Healthcare) followed by dialysis into BRB-80 buffer (80mM PIPES, 1 mM EGTA, 1 mM MgSO4, pH 6.8) supplemented with 0.1% β-mercaptoethanol [53]. The concentration of purified tau was determined by quantitative SDS-PAGE, through comparison with a tau mass standard [43].

3. Tau-MT Cosedimentation Assays

Cosedimentation assays were used to determine the amount of bound tau under each polymerization condition. Here, MTs were formed as described. 3R or 4R tau were added at a molar ratio of 5:1 or 30:1 tubulin dimer:tau, and the reaction allowed to continue for an additional 15 minutes at room temperature. In detail, we used 3 μM and 0.5 μM of tau, and added the appropriate amount of MTs based on the tau:tubulin ratio. Tau-coated MTs were layered over 180 μL of a warm sucrose cushion (50% w/v in PEM-80, supplemented with 2mM GTP) in a 5×20 mm UltraClear centrifuge tube (Beckman Coulter). Samples were spun in a TLA 100.3 fixed angle rotor for 12 min at 60,000 rpm (194,000×g) at 35°C. Supernatants and pellets were collected and solubilized in SDS-PAGE sample buffer. The quantities of tau and tubulin in each were determined by Western blotting using the monoclonal antibody Tau-1 (Millipore) and Coomassie blue staining respectively, taking care to operate within the linear detection range. Negligible quantities of tau or tubulin

remained within the cushion. These data were used to determine the molar ratio of tubulin to tau in the MT pellet.

4. Kinesin-driven MT Gliding Assays

Gliding assays were performed as previously described, with minor modifications [50]. Flow-chambers were constructed by attaching a coverslip to a glass slide with double-sided tape. Prior to use, coverslips were cleaned by exposure to a gas plasma generated by exposing room air to an 18 W radio-frequency oscillating field for 10 minutes at pressure of ~0.5–2 Torr using a commercial benchtop plasma cleaner (Harrick PDC-32G). Kinesin was diluted to 20-50 μg/ml in PEM80 buffer containing 10 mM β-mercaptoethanol then flowed into the chamber and allowed to directly adhere to the glass surface for 3 min. Following attachment of motors, the chamber was incubated for an additional 5 min with a solution of casein (~0.5 mg/mL) to reduce the non-specific binding of MTs to the glass surfaces. Microtubules were polymerized as described and used within 24 hours. For experiments with tau protein, 3R or 4R tau was added to a final ratio of 5:1 tubulin to tau. For measurements without tau protein, an equivalent volume of warm buffer was added to ensure similar final MT concentrations. In all cases, the MTs were incubated at 35°C for another 15 minutes, and the solution was diluted 1:100 in warm motility buffer containing PEM80, 5 mM ATP, 0.1% β-mercaptoethanol and an enzymatic oxygen scavenger system (650 U/mL catalase, 15 U/mL glucose oxidase and 4.5 mg/mL glucose, final concentrations). The diluted MTs were flowed into the kinesin-containing flow chamber, which was sealed with vacuum grease and visualized immediately. Gliding events were visualized using a Nikon Ti-S microscope equipped with custom-built total internal reflection fluorescence (TIRF) illumination capabilities (100× magnification, 67 nm/pixel, 19-20°C ambient temperature). Excitation

wavelength used for rhodamine imaging was 532 nm. Images were collected using an air-cooled EMCCD camera (Andor, iXon) every 0.4 s for 100 frames. MT tracking was performed manually using ImageJ to identify the leading tip of the moving MT in each frame. To calculate velocity, the total MT trajectory was divided by the time interval over which motion was observed.

5. Kinesin-driven Quantum-Dot (QD) Assays

The epothilone-stabilized MTs used in the QD assays were generated as described with an extra centrifugation step (14 krpm, 10 minutes) to remove unpolymerized tubulin dimers, which contribute to background fluorescence. The pellet was gently resuspended in a stabilization buffer containing 1 mM GTP, 2 μM epothilone-A or epothilone-B, 1 mM DTT and 2 μg of sodium azide in PEM 80, and stored at room temperature, away from light. MTs formed by this method are typically stable for up to one week. QD assays were performed as previously described, with modifications [57]. Glass flow chambers were constructed by attaching plasma cleaned 22×40 mm #1.5 coverslips to clean glass microscope slides with two parallel pieces of double-sided tape spaced ~5 mm apart. β tubulin antibody (SC-58884, Santa Cruz Biotechnology Inc.) solution (40 μg/mL) was flowed into the chambers to allow absorption to the coverslip surface. After 10 min, excess antibodies were washed out by addition of 50 μL of PEM 80. The stock MT solution was diluted 1:20 in PEM 80, and 20 μL of diluted MT solution was flowed into the chambers. After a 10 min incubation period, 4 mg/mL casein solution was introduced to remove the unattached MTs, and to passivate the glass surfaces against non-specific adsorption of kinesin or tau. After 10 min, biotinylated kinesins, diluted to ~20 ng/mL in a solution of PEM80 supplemented with 1 mM AMPPNP,

were introduced to the flow chamber. After 5 min, chambers were washed and Qdot® 605 steptavidin conjugated quantum dots (Q10101 MP, Invitrogen), diluted in 0.2 nM in PEM 80 were introduced. After another 5 min, chambers were washed with a standard motility buffer for single-molecule kinesin measurements, consisting of PEM80 supplemented with 5 mM DTT, 1% β-mercaptoethanol, an enzymatic oxygen scavenger system (650 U/mL catalase, 15 U/mL glucose oxidase and 4.5 mg/mL glucose, final concentrations), 1 mM ATP, and the desired type of tau protein at a final concentration of 100 nM tau. The chambers were sealed with vacuum grease and visualized immediately at room temperature (19-20°C). Under these assembly conditions, the polymerized tubulin dimer to kinesin dimer molar ratio in the microchamber is approximately 25:1. Considering the cylindrical geometry of the microtubule and the size of the QD there will be, on average, 2-3 microtubule-bound kinesin molecules accessible to any QD that diffuses near a microtubule.

Motions of single QDs were visualized using a custom-built TIRF microscope at 150× (magnification = 67 nm/pixel). Images were collected at room temperature using air-cooled EMCCD camera (Andor, iXon) at a rate of 10 frames per second. Excitation wavelength for QD imaging was 488 nm. A broadband emission filter was selected to allow the dim outline of the rhodamine-labeled MT to be observed in the background of the bright QD images. Images were analyzed off-line after data collection. Movies were manually screened to identify the motion of kinesin-driven QDs that warranted velocity analysis. Only runs that persisted for at least 30 frames were analyzed. QD position was determined as a function of time using the built-in FIONA algorithm available through Video Spot Tracker software (made available by CISMM at UNC-CH, supported by the NIH NIBIB, Award# NIH 5-P41-

RR02170). The initial velocities of the kinesin-QD assemblies were calculated framewise then refined to discriminate between motions parallel or perpendicular to the MT axis using a graphic-based analysis algorithm implemented in MATLAB. This was particularly useful for cases in which tau binding disrupted the antibody-MT connection, leading to thermal fluctuations of the MT substrate upon which the kinesin motors walk. For each moving kinesin-QD assembly, a region with a width of 15 pixels was drawn around the average location of the underlying MT track. The MT location was then determined by fitting a Gaussian curve to the cross section of intensity of the MT contour using ~ 100 evenly distributed points, as previously described [59]. Curve fitting was implemented using built-in algorithms. Using the resulting MT coordinates, the initial velocities were projected into two orthogonal components, one parallel and one perpendicular to the MT contour. The kinesin velocity for a single translocation event (i.e., a 'run') was given by the mean of the parallel components of the framewise velocities.

6. Microtubule Fluctuation Assays

Epothilone-assembled MTs were diluted into a PEM 80 based solution supplemented with 5 mM DTT, 1% β-mercaptoethanol with oxygen scavenger system (glucose oxidase, catalase, glucose) and 1-5 mg/ml casein. For experiments with taxol-assembled MTs, the solution is supplemented with 10 μM taxol. A drop of 2.6 μL of the MT solution is pipetted onto a clean glass slide, and a plasma-cleaned 22×40mm #1.5 cover glass is placed on top. Gentle pressure is applied to spread the solution over the entire surface of the cover glass, resulting a distance between the glass surfaces of ~3 μm. The chamber is sealed with VALAP wax (equal parts vaseline, lanolin, and paraffin) to prevent convection and evaporation. The

sample is observed immediately using the custom-built TIRF microscope and images collected using an air cooled EMCCD camera at a rate of 10 frames per second. For these measurements, we set the incident angle for laser injection to be slightly below the critical angle for true total internal reflection. This allows a mixed mode TIRF/epi excitation that allows visualization of the filaments throughout the depth of the observation chamber. Magnification is 67 nm/pixel, and data are collected at room temperature (19-20°C). A movie of 300-400 frames was collected for each fluctuating MT, and was analyzed using a custom-designed tracing and spectral analysis method, as described [59].

D. Results

1. Cosedimentation assays assess ability of MTs to bind tau

To assess the ability of epothilone-stabilized MTs to bind wild-type (WT) tau isoforms, we performed cosedimentation assays in which MTs are assembled in the presence of either epothilone-A or epothilone-B, then coated with tau. We used a total tubulin dimer to tau molar ratio of 5:1 or 30:1, which brackets the approximate physiological range for neurons [60, 61]. Previous results have demonstrated that tau binds to MTs in the absence of stabilizing agents and to taxol-stabilized MTs with a high affinity in this concentration range [9, 50].

We find no obvious differences between the abilities of microtubules stabilized with epothilone-A or epothilone-B to bind either tau isoforms, as shown in Figure 4-1. To assess the statistical significance of these data, we use a two-sample Student's *t*-test, we find that the ratios of polymerized tubulin dimers to bound tau are indistinguishable under these

conditions (full results of statistical tests are available in Table I). Consistent with prior results, we find that the ratio of tubulin in the MT polymer to bound tau is smaller than the ratio of free tubulin to tau in the initial mixture, since not all tubulin dimers are incorporated into the polymer (especially at higher tubulin:tau molar ratios) and tau binds strongly to MTs but not tubulin subunits [50].

We then compared the tau binding behavior of the epothilone-stabilized MTs to that of MTs stabilized with taxol. Qualitatively, we find that MTs stabilized with taxol appear to bind slightly more tau than do MTs stabilized with either epothilone compound, as shown in Figure 4-1. Using a two sample Student's *t*-test, we find that the differences between MTs stabilized with epothilone-A and taxol are not significant to the 95% confidence level under any tau condition. For MTs stabilized with epothilone-B, there are significant differences for 4R tau at both the 5:1 and 30:1 tubulin:tau ratio, and for 3R tau at the 30:1 tubulin:tau ratio. For both the taxol- and epothilone-stabilized MTs, we find a reduction in the amount of bound tau as compared to MTs that have been polymerized in the presence of tau but without small-molecule stabilizers. This reduction is significant for all taxol-stabilized MTs, and for all epothilone-stabilized MTs at the 30:1 tubulin:tau ratio. At the 5:1 tubulin:tau ratio, only the 4R binding to epothilone-B-stabilized MTs was statistically different from the binding of 4R to MTs in the absence of small molecule drugs. This suggests that in the absence of stabilizers, MTs adopt different conformations that modulate the tau binding affinity, or that some fraction of the tau proteins are incorporated on the inner surface of the MT that is not easily accessible after polymerization, or both.

At the 30:1 tubulin:tau ratios, less tau is present in the initial mixture, and it is likely that differences in the amount of bound tau arise from actual differences in binding affinity since there is ample space on the MT for tau to bind. By contrast, at the 5:1 tubulin:tau ratio, packing considerations on the MT surface become more important. In this limit of high tau concentration, we find fewer differences between the various polymerization conditions, suggesting that filament geometry begins to dominate in this regime.

2. Effects of small-molecule stabilizers and tau on MT stiffness

We next assessed the mechanical properties of epothilone-stabilized MTs using a spectral analysis method that allows the stiffness of a freely diffusing filament to be determined from the ensemble of shapes it adopts under thermal excitation [78]. In this approach, movies of fluctuating rhodamine-labeled microtubules are collected, and the microtubule shape is fit in each frame to a continuous curve described by a series of Chebyshev polynomials [59]. The variance of the mode amplitudes is then compared to predictions made by the worm-like chain (WLC) polymer model to determine the persistence length, L_p, a common measure of biopolymer stiffness. Physically, L_p is the length over which the filament tangent angle becomes decorrelated. L_p depends both on filament shape and intrinsic materials properties: $L_p = EI/k_BT$ where EI is the flexural rigidity and k_BT is the thermal energy. For isotropic homogeneous structures, EI is the product of the Young's modulus E and the geometric moment of inertia I. Although deviations from WLC behavior have been observed for short microtubules (< 7 μm), the microtubules used in our study range from 10–20 μm, significantly longer than this cutoff [118].

Consistent with prior studies, we find the overall distribution of MT stiffness to be broad and non-Gaussian, so we characterize the filament stiffness at each condition by the median value, and indicate the percentile differences in the distributions using a box and whiskers plot format [119]. As shown in Figure 4-2, in the absence of tau we find MTs stabilized by epothilone compounds are substantially softer than are MTs stabilized by taxol. The median L_p value for taxol-stabilized MTs is 2.0 mm, whereas MTs stabilized by epothilone-A or epothilone-B have median L_p values of 1.6 mm and 1.2 mm, respectively. For MTs stabilized by taxol or epothilone-A, the addition of either 3R or 4R tau at a 5:1 molar ratio of tubulin:tau softens the filaments. The median persistence length of epothilone-A-stabilized MTs drops to 1.0 mm for 3R tau (~ 37% reduction) and 1.1 mm for 4R tau (~ 31% reduction). The median persistence length of taxol-stabilized MTs drops to 1.1 mm for 3R tau (~ 45% reduction) and 1.3 mm for 4R tau (~ 35% reduction). By contrast, for epothilone-B-stabilized MTs, the addition of tau has little effect: the median L_p of the epothilone-B-stabilized MTs increases slightly to 1.3 mm for 3R tau and decreases to 1.1 mm for 4R tau (~ 8% increase or reduction, respectively). Interestingly, although we find the stiffness of the bare MTs varies substantially depending on the type of small molecule used, upon addition of either 3R or 4R tau, these differences nearly vanish.

3. Effects of small-molecule stabilizers and tau on kinesin translocation

We next assessed the ability of MTs stabilized with epothilone-A or epothilone-B to support kinesin motility, and further, tested the effects of 3R or 4R tau proteins on kinesin translocation for each polymerization condition. These measurements are motivated by a desire to determine the functionality of epothilone-stabilized MTs, particularly with regard to

axonal transport, since transport defects have been linked to CIPN. We employ a quantum-dot (QD)-based motility assay, in which small numbers of kinesin motors are bound to fluorescent QDs in a manner that mimics *in vivo* cargo-attachment. Given the system geometry and kinesin concentrations, we estimate that there will be, on average, 2–3 microtubule-bound kinesin molecules per QD.

We measured the velocity of the kinesin-QD complexes moving on MTs assembled with epothilone-A, epothilone-B, or taxol, then coated with no tau, 100 nM 3R tau, or 100 nM 4R tau. In the absence of tau proteins, we find no significant difference between the speed of kinesin motors moving on MTs stabilized by taxol or epothilone-A; kinesins moving on epothilone-B-stabilized MTs show a modest, but statistically significant slowing with respect to the taxol MTs (Figure 4-3). The differences between the speeds of kinesins moving on MTs polymerized with epothilone-A or epothilone-B are not significant at the 95% confidence level. Full statistical analysis of the velocity data is given in Table II.

We find a substantial slowing when we introduce tau. As we previously reported, the addition of either 3R or 4R tau to taxol-stabilized MTs reduces the mean kinesin speed from 425 ± 10 nm/s (errors given by SEM) to 360 ± 15 nm/s (~15% reduction) or 334 ± 20 (~ 21% reduction), respectively [9]. For both isoforms, the tau-dependent velocity reduction is significant ($p < 0.001$), whereas the differences in mean speed between the two isoforms (3R versus 4R) is not.

We also find significant tau-dependent reductions in kinesin speed when using MTs polymerized with either epothilone-A or epothilone-B, and moreover find that the magnitude of the reduction is significantly larger than that observed when using taxol-stabilized MTs. When using epothilone-A-stabilized MTs, the addition of 3R reduces the mean kinesin speed from 387 ± 17 nm/s to 218 ± 17 nm/s (~ 44% reduction) and the addition of 4R tau reduces the mean kinesin speed to 203 ± 17 nm/s (~ 48% reduction). When using epothilone-B-stabilized MTs, the addition of 3R reduces the mean kinesin speed from 362 ± 20 nm/s to 204 ± 17 nm/s (~ 44% reduction) and the addition of 4R tau reduces the mean kinesin speed to 208 ± 18 nm/s (~ 43% reduction). For MTs stabilized with either epothilone compound, reductions in velocity upon addition of either tau isoform are significant ($p < 0.001$). However, we do not find any significant epothilone compound-specific differences when the tau type and concentration is fixed, and we do not find tau-isoform specific differences when either epothilone-A or -B are used.

Another common measure of kinesin function in single molecule *in vitro* assays is the total travel distance per diffusional encounter with the MT, or 'run length'. By contrast, in our assay, each QD accommodates a small number of kinesin motors, and thus the cargo run length is not a particularly useful metric. In the limit that each motor operates independently, the probability of detachment of cargo from the MT depends on the product of detachment probabilities of each motor. In the case of single kinesin motors moving along bare taxol-stabilized MTs, the probability of detachment is ~10^{-2} per step. Given an 8-nm step size, this leads to an average run length of ~ 800 nm. When two motors are simultaneously engaged, the predicted run length increases to 80 μm, much longer than the average microtubule length

used in our studies. Consistent with this, in the absence of tau, >90% of the kinesin-QD assemblies bind and translocate to the end of MTs assembled by either epothilone compound or taxol. The observed run length is given by one-half of the average MT length and this is a substantial underestimate of the actual run length of the assembly. In the presence of tau, the percentage of kinesin-QD assemblies that bind and move to the end of the MT drops to ~50%, and the mean value of run length also decreases, but we do not find any obvious trend with type of stabilizing compound used (data not shown).

To confirm the results of our QD assay in a different experimental geometry, we repeated these measurements using MT gliding assays, in which fluorescently-labeled MTs glide on top of a densely kinesin-coated surface. Multiple kinesin motors bind along the length of the filament and each steps toward the MT plus end, thereby propelling the MT across the surface. The velocity measured from the gliding assays will thus be an average velocity driven by the collective behavior of all active motors. As shown in Figure 4-3 and Table II, the data obtained with the gliding assay format follow the same overall trends as those obtained with the QD assay. In the absence of tau, we find no significant differences in MT velocity when epothilone-A, epothilone-B, or taxol are used. We find a significant velocity reduction when either tau isoform is added to MTs stabilized with either epothilone compound at a tubulin:tau ratio of 5:1. The speed reductions are smaller as compared to those measured using the QD assay, with tau-dependent reductions of ~ 15-18%, in contrast to the 43-48% reductions we observed with the QD assay. When compared to the velocities at which tau-coated taxol-stabilized MTs move, we again measure smaller differences than were observed with the QD assay. We find significant reductions in gliding velocities of MTs

coated with the 4R tau isoform for both epothilone compounds ($p < 0.001$). For the 3R tau isoform, we find even smaller differences between the speeds of MTs stabilized with either epothilone compound and taxol. When the MTs are coated with 3R tau, the reduction in gliding velocities for epothilone-A-stabilized MTs as compared to taxol-stabilized MTs is significant, although the *p*-value is smaller ($p < 0.01$); for 3R tau coated MTs, the velocity difference between the taxol-stabilized MTs and epothilone-B-stabilized MTs is not significant.

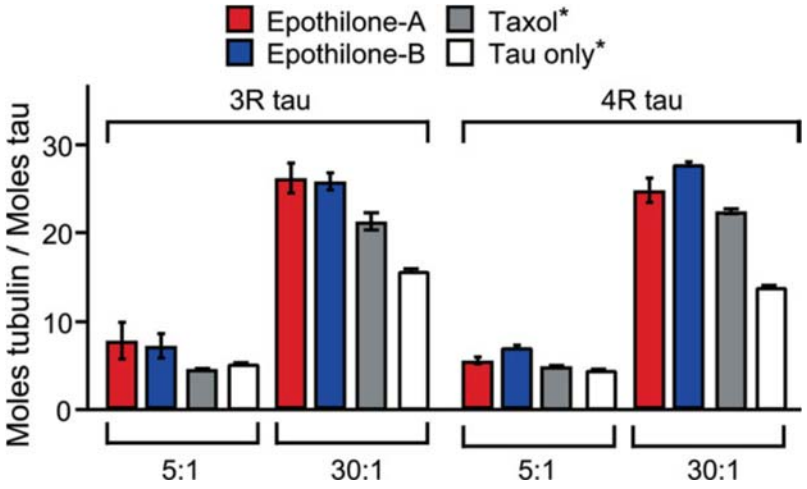

Figure 4-1: Results of Cosedimentation Assay. The ability of tau to bind to epothilone-stabilized MTs was assessed for both epothilone-A and epothilone-B. These data were compared to cosedimentation data obtained with taxol-stabilized and tau-assembled MTs. In each case, two tubulin:tau ratios were tested, 30:1 and 5:1 which span the physiological range in neurons, for both 3R and 4R tau. Full statistical analysis of these data is given in Table I. For each condition, the number of data points $N = 2$ or 3. Error bars are SEM. *Previously reported values [9].

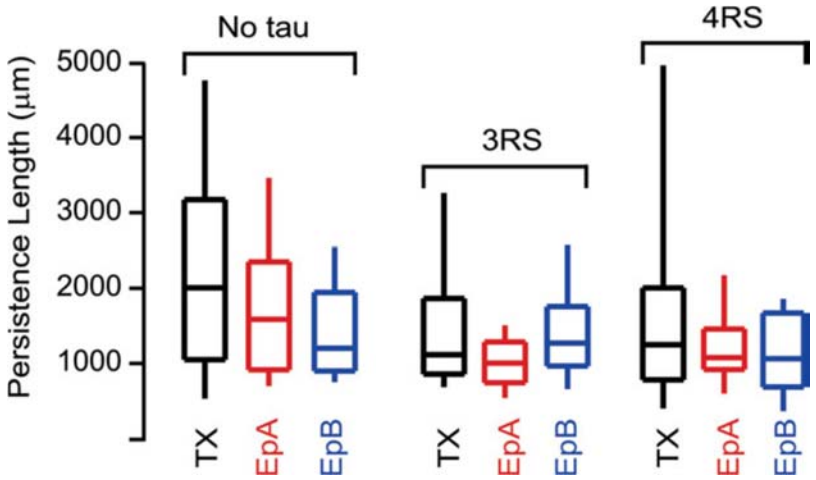

Figure 4-2: Microtubule stiffness as a function of stabilization condition and tau. MT stiffness is determined from the spectrum of thermal fluctuations of freely-diffusing filaments. MTs are stabilized by either epothilone-A, epothilone-B, or taxol, then coated with no tau, 3R tau, or 4R tau at tubulin:tau ratio of 5:1. Under each condition we find the distribution in stiffness determined from an ensemble of different MTs ($N = 25 – 78$). Box and whiskers plot is constructed as follows. The middle line of each box represents the median, the upper box edge represents the 75th percentile, the lower box edge represents the 25th percentile, and the upper and lower whisker extensions represent the 90th and 10th percentiles, respectively. Raw data distributions are shown in Figure S1.

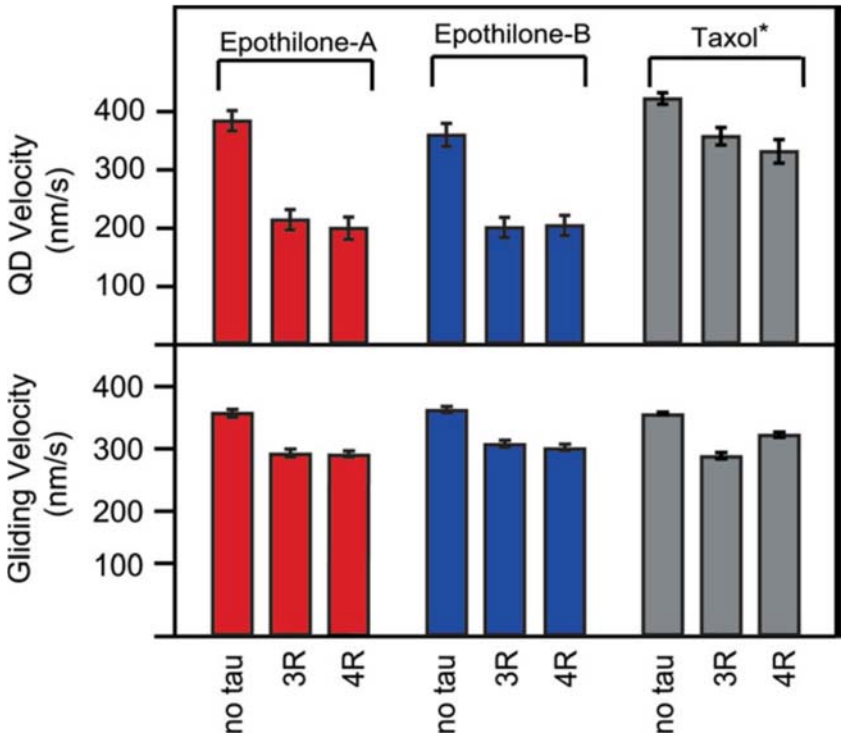

Figure 4-3: Kinesin velocity as a function of stabilization condition and tau. Kinesin velocity is determined using an MT gliding assay (upper panel, $N = 72 – 354$) or QD assay (lower panel, $N = 22 – 93$). MTs are stabilized by epothilone-A, epothilone-B, or taxol, then coated with no tau, 3R tau, or 4R tau. Full statistical analysis of these data is given in Table II. Error bars are SEM. *Previously reported values [9]. Raw data distributions are shown in Figures S2 and S3.

Table I. Results of Statistical Analysis of Cosedimentation Data

Condition 1	Condition 2	*h*	*P*-value
EpA 3RS 5:1	EpA 4RS 5:1	0	
EpA 3RS 30:1	EpA 4RS 30:1	0	
EpB 3RS 5:1	EpB 4RS 5:1	0	
EpB 3RS 30:1	EpB 4RS 30:1	0	
EpA 3R 5:1	EpB 3R 5:1	0	
EpA 4R 5:1	EpB 4R 5:1	0	
EpA 3R 30:1	EpB 3R 30:1	0	
EpA 4R 30:1	EpB 4R 30:1	0	
EpA 3R 5:1	TX 3R 5:1	0	
EpA 4R 5:1	TX 4R 5:1	0	
EpA 3R 30:1	TX 3R 30:1	0	
EpA 4R 30:1	TX 4R 30:1	0	
EpB 3R 5:1	TX 3R 5:1	0	
EpB 4R 5:1	TX 4R 5:1	1	$P<0.01$
EpB 3R 30:1	TX 3R 30:1	1	$P<0.05$
EpB 4R 30:1	TX 4R 30:1	1	$P<0.05$
EpA 3R 5:1	3R 5:1	0	
EpA 4R 5:1	4R 5:1	0	
EpA 3R 30:1	**3R 30:1**	**1**	***P*<0.01**
EpA 4R 30:1	**4R 30:1**	**1**	***P*<0.01**
EpB 3R 5:1	3R 5:1	0	
EpB 4R 5:1	**4R 5:1**	**1**	***P*<0.001**
EpB 3R 30:1	**3R 30:1**	**1**	***P*<0.001**
EpB 4R 30:1	**4R 30:1**	**1**	***P*<0.001**
TX3 R5:1	**3R 5:1**	**1**	***P*<0.001**
TX4 R5:1	**4R 5:1**	**1**	***P*<0.05**
TX 3R 30:1	**3R 30:1**	**1**	***P*<0.001**
TX 4R 30:1	**4R 30:1**	**1**	***P*<0.01**

A two-sample Student's *t*-test (implemented in MATLAB) is used to compare the cosedimentation data to identify statistically significant differences in tau binding. An h value of 1 indicates a significant difference at a minimum confidence level of 95%. P value ranges are shown for data where $h = 1$. The labels at each condition give the type of small molecule stabilizer used (EpA = Epothilone-A, EpB = Epothilone-B, TX = taxol), the type of tau protein used (3R or 4R), and the molar ratio of tau:tubulin dimer in the original mixture.

Table II. Results of Statistical Analysis of Velocity Data

		QD Assay		Gliding Assay	
Condition 1	Condition 2	*h*	*P*-value	*h*	*P*-value
EpA	EpB	0		0	
EpA	TX	0		0	
EpB	TX	1	$P<0.01$	0	
EpA 3RS	**EpA**	**1**	$\boldsymbol{P<0.001}$	**1**	$\boldsymbol{P<0.001}$
EpA 4RS	**EpA**	**1**	$\boldsymbol{P<0.001}$	**1**	$\boldsymbol{P<0.001}$
EpB 3RS	**EpB**	**1**	$\boldsymbol{P<0.001}$	**1**	$\boldsymbol{P<0.001}$
EpB 4RS	**EpB**	**1**	$\boldsymbol{P<0.001}$	**1**	$\boldsymbol{P<0.001}$
EpA 3RS	EpB 3RS	0		1	$P<0.05$
EpA 4RS	EpB 4RS	0		0	
EpB 3RS	**TX 3RS**	**1**	$\boldsymbol{P<0.001}$	**1**	$\boldsymbol{P<0.01}$
EpB 4RS	**TX 4RS**	**1**	$\boldsymbol{P<0.001}$	**1**	$\boldsymbol{P<0.001}$
EpA 3RS	TX 3RS	1	$P<0.001$	0	
EpA 4RS	**TX 4RS**	**1**	$\boldsymbol{P<0.001}$	**1**	$\boldsymbol{P<0.001}$
EpA 3RS	EpA 4RS	0		0	
EpB 3RS	EpB 4RS	0		0	

A two-sample Student's *t*-test (implemented in MATLAB) is used to compare the velocity data for both the QD and gliding assay to identify statistically-significant differences in kinesin translocation rates. An h value of 1 indicates a significant difference at a minimum confidence level of 95%. P value ranges are shown for data where $h = 1$. Those conditions that were found to be significantly different using both assays are indicated in bold. The labels at each condition give the type of small molecule stabilizer used (EpA = Epothilone-A, EpB = Epothilone-B, TX = taxol), the type of tau protein used (3R or 4R), and the molar ratio of tubulin dimer:tau in the original mixture.

E. Discussion

There have been several prior studies of the effects of tau on MT stiffness. In the absence of small molecule stabilizers, MTs that have been polymerized in the presence of GTP with GMPCPP stabilizing caps were measured to have a mean L_p of ~ 6.0 mm at 37°C using a similar spectral analysis method [80]. For MTs that are polymerized in the presence of taxol without GMPCPP caps, the mean L_p has been measured by spectral analysis to be 7.5 mm at 37°C and 4.9 mm at 25°C [78, 80]. The stiffness of MTs polymerized in the presence of a recombinant bovine tau protein with 4 binding repeats and 2 projection domains at a molar ratio of ~5:1 tubulin:tau, but without small molecule stabilizers, was determined to be 7.9 mm [80].

A second prior approach examined the shape changes of MTs that are actively bent using optical tweezers, then allowed to relax back to their equilibrium shape by moving through a viscous buffer [76, 77]. Using this relaxation method, the persistence length of MTs grown off an axoneme template under various polymerization conditions was determined for MTs at room temperature (22°C –25°C). In the absence of stabilizing compounds or tau, the mean L_p was measured to be 0.9 mm, and in the presence of taxol this value decreases to 0.2 mm [77]. Although there are significant variations in the stiffness values determined by different methods (as reviewed in [120]), the hydrodynamic relaxation methods tend to give systematically lower values for stiffness than do the methods that employ spectral analysis of thermal fluctuations. The role of taxol in determining MT stiffness has been particularly controversial, although most measurements have indicated that the addition of taxol softens

MTs [120]. Consistent with this, we have found that the addition of taxol to GMPCPP-stabilized MTs reduces MT stiffness (data not shown).

To our knowledge, there have been no measurements of the effects of epothilone compounds on MT stiffness, however, a number of structural studies have indicated that epothilone binding induces tubulin conformational changes. Hydrogen-deuterium exchange mass spectroscopy experiments have shown that epothilone-A, epothilone-B, and a synthetic analog of epothilone-B called ixabepilone improve longitudinal contacts at the interface between tubulin dimers along a single protofilament and have little effect on the lateral interactions between protofilaments [121, 122]. Similar interactions were observed when MTs were stabilized by docetaxel, a compound related to taxol [121]. The epothilones and taxol appear to bind to the same (or overlapping) sites on the tubulin dimer, and to stabilize MTs in a similar manner [123]. MTs stabilized by either taxol or epothilone-B have been found to have similar architecture, with the epothilone-stabilized MTs being slighter larger in diameter: 60% or 35% of taxol-stabilized MTs have 12 or 13 protofilaments, whereas 22% or 67% of epothilone-B-stabilized MTs have 12 or 13 protofilaments, respectively [124]. Given this, the origins of decreased stiffness with the epothilone compounds are not clear.

In the absence of small molecule stabilizers, the addition of a wide variety of tau constructs uniformly increased MT stiffness, as measured by hydrodynamic relaxation [76]. When MTs were assembled with the tau construct most similar to our 3R tau (the HT23 construct with three MT binding repeats and zero projection domains) the mean L_p value increased from 0.9 mm to 2.1 mm when the MT surface wass nearly saturated with tau. When a four-repeat

tau construct with two projection domains (the HT40 construct, or the 'long' form of 4R tau) was used at a concentration near MT saturation, the MT L_p was 2.5 mm. When the concentration of HT40 was systematically increased from ~2% to ~ 85% of saturation, the measured L_p values increased monotonically.

Our results extend this prior work in two ways. After confirming that MTs stabilized by both epothilone-A and -B were able to bind tau proteins at affinities that were similar to taxol-stabilized MTs, we determined the effects of these non-taxol small molecule stabilizers on MT stiffness. We find that in the absence of tau proteins, epothilone-stabilized MTs are substantially less stiff than those stabilized by taxol, and that epothilone-A- and -B-stabilized MTs have slightly different stiffnesses. Of all three stabilizing compounds, epothilone-B MTs are most flexible. When we add either the 3R or 4R 'short' tau constructs, to the taxol- or epothilone-A-stabilized MTs, the stiffness decreases. For epothilone-B stabilized MTs, there is no clear effect with the addition of tau. This is in contrast to prior work on MTs assembled by tau in the absence of stabilizing drugs, in which the addition of tau proteins has always increased stiffness. Interestingly, the stiffness differences that we observed using MTs formed by different stabilizing compounds in the absence of tau nearly vanish.

The molecular-level changes that give rise to this tau-dependent reduction in stiffness in the presence of small-molecule stabilizers are not clear. Possible mechanisms include either a reduction in the number of protofilaments upon addition of tau, or a change in the inter- or intra-protofilament interaction energy that would lead to a reduction in the effective bending modulus of the MT. For the case of taxol-stabilized MTs, the addition of any of the six

naturally-occuring isoforms of tau has been shown to increase the average MT protofilament number in a tau concentration-dependent manner [125]. This suggests that at least for taxol-stabilized MTs, the reduction in stiffness due to tau addition must arise from changes in the interaction energies between tubulin dimers. To our knowledge, the effects of epothilone compounds on MT structure in the presence of tau are unknown.

We also tested the ability of epothilone-stabilized MTs to support kinesin translocation using two experimental geometries in the QD and MT gliding motility assays. In the absence of tau, both epothilone-A and -B are able to support kinesin-driven motility, at speeds that are similar to and in most cases indistinguishable from that of taxol-stabilized MTs. For all small molecule stabilizers, we find that the addition of tau decreases kinesin velocity. In almost all cases, the reductions observed are greater when MTs are stabilized with an epothilone compound rather than taxol. The tau-dependent reductions are markedly larger for the epothilone compounds when the QD assay is used.

We suspect that the origins of these differences arise due to the different binding geometries in the QD and gliding assays. In the MT gliding assay, large ensembles of kinesin motors work cooperatively to move a microtubule, whereas in the QD assay only 2-3 kinesin motors are actively engaged at any one time. It is possible that the topography of the epothilone-stabilized MTs differs from that of the taxol-stabilized MTs in a manner that causes the kinesin motors to adopt different trajectories along the surface. Since the QD assay averages the motions of a small number of motors, any instantaneous changes in stepping patterns due either to direct tau-kinesin interactions, or to tau-dependent differences in the tubulin-kinesin

interactions may be more evident in the QD assay than in the MT gliding assay that averages over a much larger ensemble.

Alternatively, it is possible that the differences observed using the MT gliding and QD assays arise from subtle changes in tau concentration in the two assays. The multiple wash steps and buffer exchanges used in the preparation of the immobilized MTs and kinesin-QD complexes prevent knowledge of the absolute tubulin:tau molar ratio, whereas the MT gliding assay maintains a well-defined tubulin:tau ratio of 5:1. However, we have tested the effects of tau concentration on kinesin translocation using taxol-stabilized MTs and found no change in velocity for tau concentrations ranging from 100 nM to 1 μM, consistent with prior results. Moreover, the QD assay preparation is identical for MTs polymerized with each small molecule stabilizer, and we control the average number of MTs per field of view for each experiment. Thus even if some of the differences we observe between the QD and MT gliding assays do arise from changes in bound tau concentration, we expect that the differences observed between the taxol- and epothilone-stabilized MTs using the QD assay do not.

In summary, we find the MTs stabilized by either epothilone-A or epothilone-B are competent to bind tau proteins, and support kinesin translocation. However, epothilone-stabilized MTs are substantially less stiff than taxol-stabilized MTs, and the addition of tau proteins to MTs stabilized by either epothilone-A or taxol further reduces stiffness. Kinesin translocation is also affected not only by the presence of tau, but by the type of small molecule stabilizer used. These results suggest that small molecule stabilizers do not simply

stabilize a “native” MT structure, but rather are active agents that remodel MT structure, function, and mechanics. This may have important consequences to the use of these agents as chemotherapeutics. One possible outcome of our work is the development of functional screening methods to select and optimize chemotherapeutic compounds with minimal impacts on MT stiffness, kinesin translocation, and axonal transport.

V. Effect of disease-linked tau mutants on taxol-assembled microtubule mechanics

This chapter will discuss the effects of disease-related tau mutants on the mechanical properties of taxol-assembled microtubules.

A. Abstract

Using the biochemical and biophysical tools that we have developed in the previous sections, we investigated the effects of three different tau proteins, each with a different single-point mutation, on the mechanical properties of microtubules (MTs) that were assembled in the presence of taxol. We found that MTs that are assembled with taxol and coated with R406W, P301L or ΔN296 tau mutants have persistence lengths similar to those of taxol-assembled MTs in the absence of tau. Other than the 4RS ΔN296 mutant, the persistence lengths of all mutant tau-coated MTs (3RS R406W, 4RS R406W and 4RS P301L) are significantly higher than MTs coated with their corresponding wild-type tau (3RS WT and 4RS WT) constructs. The discrepancies in MT stiffness suggest that the binding of mutant tau proteins can affect the "native" structure and modify the mechanics of the MTs differently compared to the wild-type constructs. Although the differences are subtle, small defects in MT regulations in neurons may over time contribute to severe diseases, such as dementia.

B. Methods

Taxol-assembled MTs were generated using the same method as in Chapter II (See *Tubulin preparation and microtubule assembly*, Page 65). Microtubule fluctuation assays were conducted as described previously in Chapter IV (See Microtubule Fluctuation Assays, Page

68) with minor modification. After the polymerization reaction has completed, one of the tau constructs (3RS WT, 4RS WT, 3RS R406W, 4RS R406W, 4RS P301L, 4RS ΔN296) is added to solution at a 5:1 molar ratio of tubulin:tau (final concentration of 100 nM). The statistical significance of the persistence length differences we observe data was determined using a built-in non-parametric Kolmogorov-Smirnov test algorithm in MATLAB.

C. Results and Discussion

Using the spectral analysis technique described in Chapter III (See Page 34), we measured the persistence lengths, L_p, of taxol-assembled MTs coated with one of the six tau constructs (3RS WT, 4RS WT, 3RS R406W, 4RS R406W, 4RS P301L, 4RS ΔN296) at a 5:1 molar ratio of tubulin:tau. In agreement with ourprevious results and the obervations of others, the distributions of MT persistence lengths were non-Gaussian [9, 59], and again we characterize the MT persistence length at each condition by the median value, and graphically present the distributions using a box and whisker plot format. As shown in Figure 5-1, the median persistence length of taxol-assembled MTs in the absence of tau is 2.0 mm. The median persistence lengths reduce to 1.1 mm and 1.3 mm upon the addition of 3RS WT and 4RS WT tau, respectively. The median persistence lengths measured for MTs that are assembled by taxol and then coated with one of the four mutant tau constructs are 2.0 mm for 3RS R406W, 2.0 mm for 4RS R406W, 1.9 mm for 4RS P301L and 1.6 mm for 4RS ΔN296. We tested the statistical significance of the persistence length distributions using a non-parametric two-sample Kolmogorov-Smirnov test. As shown in Table 5-1, the persistence lengths on MTs in the absence of tau are significant stiffer than those of MTs coated by either of the 3RS WT and 4RS WT tau proteins. The mutant tau-coated MTs showed no difference in MT stiffness

compared to the no tau condition, but all are significantly stiffer than their corresponding wild-type tau construct, except for 4RS ΔN296.

The differences in stiffness and persistence lengths between some of the wild-type tau and mutant tau constructs suggest possible differences in MTs structure modifications. A previous study showed that the addition of tau as a secondary stabilizer, after MTs were assembled in the presence of taxol, modifies the radius of curvature of the MT surface and increases the average protofilament number of the MTs [6]. With our assumption that MTs are homogeneous and isotropic, the bending stiffness is equal to $\boldsymbol{EI}$, where $\boldsymbol{E}$ is the effective Young's modulus, and $\boldsymbol{I}$ is the second moment of area of the MT cross-section, which roughly scales as the fourth power of the MT radius. The increase in protofilament number will necessarily increase the radius of the MTs, which will in theory lead to an increase in stiffness. However, we observed lower MT stiffness in the presence of wild-type tau, which was contradicted to our expectation. Although the underlying mechanism is not understood at this point, we suspect that the binding of tau alters the arrangements of tubulin dimers and modifies the inter- and intra-protofilamental energy landscape along the MTs, which lowers the effective Young's modulus of the MTs to (over)compensate for the effect of increasing radius and the second moment of area. Additionally, it is possible that mutations in the tau sequence can also lead to different binding behaviors, as recent results in our lab have found evidence of cooperative binding behavior in a similar microtubule-associated protein (MAP) binding system of EB1 [126]. The differences in tau-tau interactions can lead to abnormal clumpings or aggregations that create greater geometric changes on the MT surface and larger accumulated electrostatic effects on the binding energy landscape. Despite all these

possible models of what may happen in the MT structure, we should be cautious about interpreting the results from this study since the MTs in the experiments were assembled in the presence of small molecule stabilizer taxol. As we have discussed in studies in Chapters II and IV, these small molecule stabilizers do not simply stabilize the "native" structure of MT. We have seen multiple incidents of these small molecule stabilizers "locking" MTs in specific structures that mask the potency of a secondary stabilizing agent such tau on the mechanical and functional properties of MTs. Recently, we have looked at the mechanical properties of MTs that were assembled in the presence of WT tau without the inclusion of taxol. The persistence lengths of these tau-assembled MTs were much higher (~10 mm, data not shown) compared to any of our taxol-assembled tau-coated MTs. These results further bolster our theory that MT properties, mechanical and functional, were dominated by the first stabilizer used during MT assembly, which limits the effects of secondary stabilizers. One must pay attention to the assembly conditions and the order of addition of different stabilizing agents when conducting future experiments on microtubule-related subjects. Future high-resolution single-filament structure measurements on the MT lattice structure under various assembly and stabilization conditions will be essential to understand the molecular mechanisms driving the observed changes in MT mechanics. Of particular interest are super-resolution imaging methods that may allow for dynamic measurements of the binding and motions of tau proteins on the MT lattice.

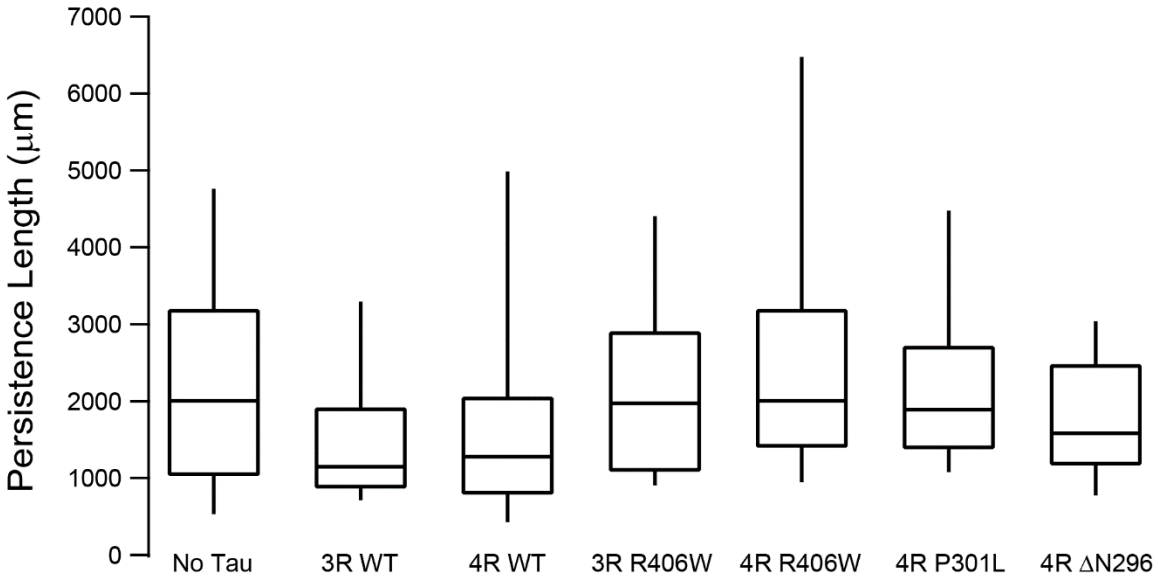

Figure 5-1: Microtubule stiffness in various conditions. MT stiffness is determined from the spectrum of thermal fluctuations of freely-diffusing filaments. MTs are assembled by taxol, then coated with no tau, 3RS WT, 4RS WT, 3RS R406W, 4RS R406W, 4RS P301L or 4RS ΔN296 tau at tubulin:tau ratio of 5:1. Under each condition we find the distribution in stiffness determined from an ensemble of different MTs ($N = 27 – 78$). Box and whiskers plot is constructed as follows. The middle line of each box represents the median, the upper box edge represents the 75th percentile, the lower box edge represents the 25th percentile, and the upper and lower whisker extensions represent the 90th and 10th percentiles, respectively.

Table 5-1: Statistical Analysis of Persistence Length Data

Condition 1	Condition 2	*h*
No Tau	3R WT	1
No Tau	4R WT	1
No Tau	3R R406W	0
No Tau	4R R406W	0
No Tau	4R delN296	0
No Tau	4R P301L	0
3R WT	4R WT	0
3R WT	3R R406W	1
3R WT	4R R406W	1
3R WT	4R delN296	1
3R WT	4R P301L	1
4R WT	3R R406W	1
4R WT	4R R406W	1
4R WT	4R delN296	0
4R WT	4R P301L	1
3R R406W	4R R406W	0
3R R406W	4R delN296	0
3R R406W	4R P301L	0
4R R406W	4R delN296	0
4R R406W	4R P301L	0
4R delN296	4R P301L	0

A two-sample Kolmogorov-Smirnov test (MATLAB) is used to analyze the statistical differences of microtubule persistence lengths between different conditions. A *h* value of 1 indicates a significant difference at 95% confidence level.

VI. The Effects of Tau on Intracellular Trafficking in COS-7 Cells

In this chapter, we will discuss the effect of WT and mutant forms of tau on cytoskeletal structure and intracellular transport in non-neuronal COS-7 cells.

A. Abstract

Tau proteins are expressed abundantly in human neurons, and are known to regulate the dynamics and structures of cytoskeletal microtubule filaments. Tau mutations and misregulation can cause severe neurodegenerative diseases including Alzheimer's disease, frontotemporal dementia with parkinsonism-17, progressive supranuclear palsy, and corticobasal degeneration. We previously showed that 4RS wild-type (WT) tau proteins and 4RS tau mutants (R406W, P301L, ΔN296) can inhibit the efficiency of kinesin-driven cargo transport along microtubules in a simplified *in vitro* environment. This cellular mechanism is extremely important as it regulates the chemical balance inside the cytoplasm. Moreover, the transport of vital organelles and other molecules through substantial distances across the cell is impossible to achieve efficiently via random diffusion. This active transport mechanism is utilized by many biological and therapeutic processes such as virus infection, gene therapy, and drug delivery. In this study, we used a combination of biophysical tools and imaging techniques to investigate the effects of transient tau expression on lysosome transport in COS-7 African green monkey kidney tissue cells, which are natively tau-free. We found that the introduction of tau proteins (either wild-type or mutant tau) dramatically rearranges the structure of microtubule networks in the COS-7 cells, yet the modifications in the cytoskeletal networks had little effect on the speed and run length of motor-driven direct lysosome transports in the cells. This suggests that localized transport events are insensitive

to the global structure of the MT cytoskeleton, and that MT bundling and aggregation do not substantially impair motor-driven transport. Additionally, although the introduction of tau clearly impacted MT organization, we found little evidence that the disease-linked tau mutants were particularly toxic, in fact we found mutant and WT tau forms led to similar overall structures and transport phenotypes.

B. Methods

1. Cell Culture

COS-7 African green monkey kidney tissue cells were maintained in maintenance medium composed of Dulbecco's Modified Eagle's Medium supplemented with 5% horse serum (Cellgro, 35-030-CV), 5% supplemented calf serum (HyClone, SH30072.03), 44 μM sodium bicarbonate and 1% Antibiotic-Antimycotic (Gibco, #15240-062) at 37°C and in a humidified, 7.5% CO_2 atmosphere. Cells were maintained at a subconfluent density and were split 1:5 every roughly 2-3 days to ensure that cells were not overly populated. Cells were trypsinized (Gibco, 25300-054), resuspended in antibiotic-free maintenance medium and plated on coverslip-bottomed culture dishes (Bioptechs) coated with poly-L-lysine (50 μg/mL, Sigma) at a concentration of 0.25×10^4 cells/cm^2 two hours prior to transfection. We note that, *in vivo* studies with tau proteins may be easier to interpret in primary neuron cultures or using other neuron-related cell types, such as PC12 cells, a line derived from a pheochromocytoma of the rat adrenal medulla which can be induced to adopt a neural morphology under treatment by nerve growth factor, which both have native expression of tau proteins to regulate MT growth and structures [61]. Unfortunately, and despite substantial time investment and effort, we had technical difficulties in culturing and expressing tau in

PC-12 cells, and eventually decided to move forward with the COS-7 line, which has been extensively used in biophysical studies, particularly of intracellular transport [127]. COS-7 cells have the distinct advantage that they lack endogenous tau, so there is no population of WT tau to dilute the effects of the mutants.

2. Tau DNA and transfection

The PAAV-IRES-hrGFP (Strategene, 240075) expression vector containing an insert of human cDNA sequences for 3-repeat short or 4-repeat short tau isoforms was used to introduce tau proteins in COS-7 cells. The expression vector substrate contains a CMV promoter, which is compatible with mammalian cells and a separate internal ribosome entry site (IRES) for GFP expression. The fluorescence signal from the freely diffusing GFP proteins acts to identify the transfected cells within the ensemble (transfection efficiency is typically ~20%). Single point mutations (P301L, R406W and ΔN296) were introduced into the 4-repeat tau gene using the QuickChange II site-directed mutagenesis kit (Agilent Technologies, 200523). The vector containing the tau sequence of interest (1 μg) was transfected into the COS-7 cells 2-hrs after seeding in coverslip-bottomed culture dishes, as described previously (*Cell culture*, page 97) using the PolyJet transfection reagent (3 μL, SignaGen, SL100688). The plasmid/PolyJet containing media was removed and replaced with fresh maintenance media 18 – 20 hours post-transfection.

3. Lysosome labeling, image acquisition and tracking

COS-7 cells were visualized using fluorescence microscopy 1-2 days after transfection. Before imaging, lysosomes in the cells were fluorescently labeled using LysoTracker Deep

Red (50 nM, Life Technologies) at 37°C for 30 minutes. The media containing LysoTracker was then replaced with Live Cell Image Solution (Life Technologies, A14291DJ) immediately before imaging. Cells were visualized with an Olympus DSU Confocal microscope, using the 100X oil immersion objective (NA = 1.X) and with spinning disk removed to allow for epifluorescence illumination. The cells are maintained at 37°C using a heated environmental enclosure. All imaging was performed at the UCSB NRI-MCDB Microscopy Facility. Images were obtained using a Hamamatsu ImaEM CCD camera with a frame rate of 0.5 Hz for a total collection time of 100 seconds. Lysosomes in the image series were tracked using the MOSAIC particle tracking algorithm available as an ImageJ plugin [128]. Tracking parameters were optimized to eliminate tracking errors (Radius = 4, Cutoff = 0, Percentile = 0.1%, Link Range = 2, Displacement = 9).

4. Trajectory analyses

One challenge of this research is identifying and selecting the motor-driven motions of the fluorescent lysosomes from among the large data set of diffusive and non-directional motions of non-motor driven cargoes. To accomplish this, multiple selections were performed to identify motor-bound lysosomes that underwent directed processive transport. Initially, only those tracked lysosome trajectories that persisted for at least 30 frames were selected to warrant their validity to perform additional analysis. To distinguish processive cargoes from those that are diffusing or are not moving at all, we performed the Speed Correlation Index analysis, as described in Bouzigues and Dahan, 2007 [129]. Trajectories were first divided into different sets of a multi-segment system with segments of equal lengths (See Figure 6-

1); then the directional correlations between neighboring segments were calculated for each set as following:

$$C_k(i) = \frac{U_k(j) * U_k(j+1)}{|U_k(j)||U_k(j+1)|}$$

where C_k (i) is the speed correlation index, ranging from 0 to 1 (0 indicates complete uncorrelated random motion, and 1 indicates perfectly correlated motion),at point i in set k, U_k (j) and U_k (j+1) are the average velocity vector of segment j, which contains point i, and the neighboring segment j+1. The average correlation, C(i), was then calculated at point i over all k segment sets. Segments that contained consecutive points with high correlation index indicate correlated directional motions. Parameters in the analysis such as segment length and threshold value of correlation index were determined and optimized in simulated trajectories of pure random diffusion that closely mimicked the actual experimental environment (Data not shown). Based on the outcomes of these simulations, sections in the trajectories with correlation indexes higher than 0.6 (segment length = 5) that persisted for more than 15 points were selected for further analyses. Trajectories were divided into runs that were categorized as anterograde (+, toward cell periphery) or retrograde (-, toward cell center) based on the directions of the movements in relation to the radial vectors from the centers of the cells. A displacement was anterograde if the angle between the displacement vector and the radial vector from the cell center was less than 90°, in all other cases this trajectory be tagged as retrograde. The mean speed and run length (total travel distance) of each run was measured.

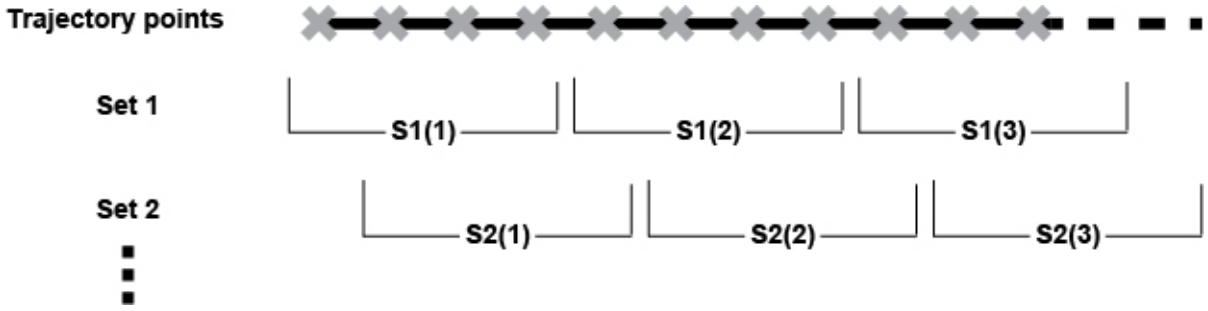

Figure 6-1: Speed correlation index analysis. Trajectory were divided into segments of equal length ***L***, in this case ***L*** = 4. Different sets of segments were generated by shifting the origin of the original segment set by 0, 1, ..., ***L***-1.

5. Immunofluorescence

Cells were first fixed with warm 3.7% formaldehyde (37°C) for 8 minutes at 37°C. Cells were then subsequently fixed in chilled 100% methanol (-20°C) for 5 minutes. Fixed cells were rehydrated with PBST buffer (0.1% Triton-X-100 in PBS) and incubated in PBST blocking buffer (1% BSA, 1% donkey serum, and 0.1% Triton-X-100 in PBS) for 30 minutes. Cells were incubated overnight first with rabbit monoclonal anti-alpha tubulin antibody (1:500, EMD Milipore), then incubated overnight in the presence of Cy5-conjugated goat anti-rabbit secondary antibody (1:400, Jackson ImmunoResearch). Tau proteins in the fixed cells were labeled with Tau 5 mouse anti-rat antibody (1:500, BD Biosciences) for 1 hour, followed by Cy3-conjugated goat anti-mouse secondary antibody (1:400, Jackson ImmunoResearch) for 1 hour. All incubations with antibodies were done at room temperature. Cells were washed 4 times for 8 minutes per wash cycle with PBST after each antibody incubation. Images were obtained using Olympus Fluoview 1000 Spectral Confocal, with a 60X silicone oil immersion objective (NA = 1.X) at the UCSB NRI-MCDB Microscopy Facility.

C. Results

1. Immunofluorescence images reveal substantial disruption of the microtubule network upon the addition of tau

Previous studies suggest the expression of tau in non-neuronal cell lines, such as Sf9, COS and L cells, alters cell morphology and induces formation of microtubule (MT) bundles [130-133]. We were interested in examining the effects of tau on the MT network morphology and structure in the COS-7 cells. We employed immunofluorescence techniques to visualize the distribution of MT filaments and tau proteins in cells that were fixed 1-2 days post-transfection. Surprisingly, the immunofluorescence images in our study showed, for all conditions, a diffusive fluorescence signal of tau in transfected COS-7 cells with no apparent co-localization with MT filaments. Despite this, we observed dramatic changes in MT network morphology in COS-7 cells after transfection with several prominent features. (1) Instead of the long filamentous MTs that we observed in cells without tau expression (Figure 6-2 1st row, bottom cell 2nd row), we found bright punctate tubulin signals in cells that were transfected with tau after one day. These punctate spots were indications of possible disruption and aggregation of unpolymerized tubulins. (2) We also observed thick "membrane-associated" MT bundles near the cell peripheries in the majority of transfected cells (Figure 6-2, 3rd row), which transformed the MT network from an "aster-like" morphology to a radial, "wheel-like" geometry. (3) Lastly, we found the formation of "axon-like" MT bundles into extended "processes" between transfected cells and neighboring cells (Figure 6-2, 4th row). These phenotypic features were observed for all tau constructs (3RS WT, 4RS WT, 4RS P301L, 4RS R406W, and 4RS ΔN296). Additionally, these phenotypic features appeared to be more prominent in COS-7 cells two days after transfections, when

more bundling and more membrane association was observed (Figure 6-3). Higher tubulin fluorescence intensity was also found in cells 2-days post-transfection as compared to cells that were transfected and then fixed after only one day (Figure 6-3).

2. Addition of tau in COS-7 cells reduces cargo velocity

Another focus of this study is to assess the effect of tau on cargo trafficking inside COS-7 cells. We fluorescently labeled lysosomes in the cells using LysoTracker Deep Red reagent and imaged using fluorescence microscopy. Time-lapsed images were collected and analyzed with well-developed particle tracking algorithm. Unlike the *in vitro* studies that we discussed in Chapters II and IV, the environment in the cellular system is much more complex as we had less control over the surrounding composition and distribution of the microtubule (MT) filaments and labeled particles in the experiments. Furthermore, cargoes in cells are typically carried with multiple motors and also different types of motors in comparison to the simplified Q-dot assay in our *in vitro* studies where particles were coated only with purified kinesin proteins and only moved along isolated MTs. As a result, cargoes in cells are able to move in both directions along MT filaments and exhibit many different moving behaviors due to geometry constraints and physical hindrances.

Lysosomes that were undergoing directed transport were selected for velocity analysis. Trajectories were divided into runs that were categorized as anterograde (+, toward cell periphery) or retrograde (-, toward cell center) based on the direction of the particle motion with respect to the center of the cell. The average speed of each run was measured as described previously (Methods: *Trajectory analyses*, Page 99). Based on the overall

organization of the MT cytoskeleton, and many prior studies of MT-based transport, we assume that the motions along different directions of the MTs were driven by different groups of motor proteins. Anterograde transports are known to be dominated by kinesin motors, whereas retrograde transports are handled by dyneins. These two families of motor proteins were found in previous studies to have different structures and different stepping behaviors [134, 135]. Therefore, we would expect to see differences in the velocities measured in different directions. Interestingly, as shown in Figure 6-3, the mean velocities measured in our experiments for anterograde and retrograde lysosome transports are surprisingly similar for most of our conditions. We conducted statistical analysis to compare the anterograde and retrograde velocities measured in each condition using a two-sample Kolmogorov-Smirnov algorithm (MATLAB), and found no statistical significance in any of the conditions based on a 95% confidence level.

We next examined the effect of tau on anterograde (kinesin-driven) lysosome transport. Without the introduction of tau, lysosomes that were transported in the anterograde direction had an average velocity of 397 ± 34 nm/s. One day after transfection, the average anterograde velocities dropped to 253 ± 48 nm/s for 3RS WT, 361 ± 50 nm/s for 4RS WT, 294 ± 27 nm/s for 4RS P301L, 285 ± 28 nm/s for 4RS R406W, and 264 ± 20 for 4RS ΔN296. Some of the differences seemed to be substantial, yet only the average anterograde velocities of lysosomes in 4RS R406W and 4RS ΔN296 transfected cells were statistically different to that measured using the no tau condition. None of the lysosome anterograde speeds for cells expressing the tau mutants were statistically different than for cells expressing wild-type 4RS WT. After two days of transfection, we measured the average

anterograde velocities to be the following: 272 ± 52 nm/s for 3RS WT, 248 ± 32 nm/s for 4RS WT, 310 ± 31 nm/s for 4RS P301L, 393 ± 47 nm/s for 4RS R406W, and 350 ± 28 nm/s for 4RS ΔN296. When we compare the anterograde velocities of lysosomes moving in cells expressing the two wild-type constructs to a no tau control, we found a significant reduction in speed according to the Kolmogorov-Smirnov test. On the other hand, the lysosome velocities for cells expressing the mutants showed no statistical significance as compared to the cargo speeds for cells without tau, suggesting that the mutant-tau-containing cells eventually recover in a way that the WT-tau-containing cells do not. The full statistical analysis is shown on Table 6-1.

Similarly for retrograde (dynein-driven) lysosome transport, the average velocities dropped one day after transfection from the no tau velocity of 378 ± 34 nm/s to 341 ± 57 nm/s for 3RS WT, 280 ± 37 nm/s for 4RS WT, 269 ± 25 nm/s for 4RS P301L, 253 ± 25 nm/s for 4RS R406W, and 254 ± 29 nm/s for 4RS ΔN296. The velocities in mutant-expressing cells were significantly different than the no tau velocities, while the wild-type velocities were not. In contrast to the kinesin-driven transport, in no case were the cargo speeds for the 4RS mutant-expressing cells statistically significant compared to 4RS WT. On Day 2 after transfection, we again observed the recovery of average retrograde velocities for tau mutants to 320 ± 30 nm/s for 4RS P301L, 290 ± 38 nm/s for 4RS R406W, and 367 ± 29 nm/s for 4RS ΔN296, while the average velocities for wild-type constructs decreased further to 261 ± 37 nm/s and 265 ± 34 nm/s for 3RS WT and 4RS WT, respectively. More statistical test results can be found in Table 6-1. Distributions of lysosome velocities and run lengths are shown in Figure S6-1, S6-2 and S6-3, yet we did not notice any obvious trends or outliers from the

distribution histograms, again suggesting that the mutant and WT type forms had similar effects on motor-driven transport.

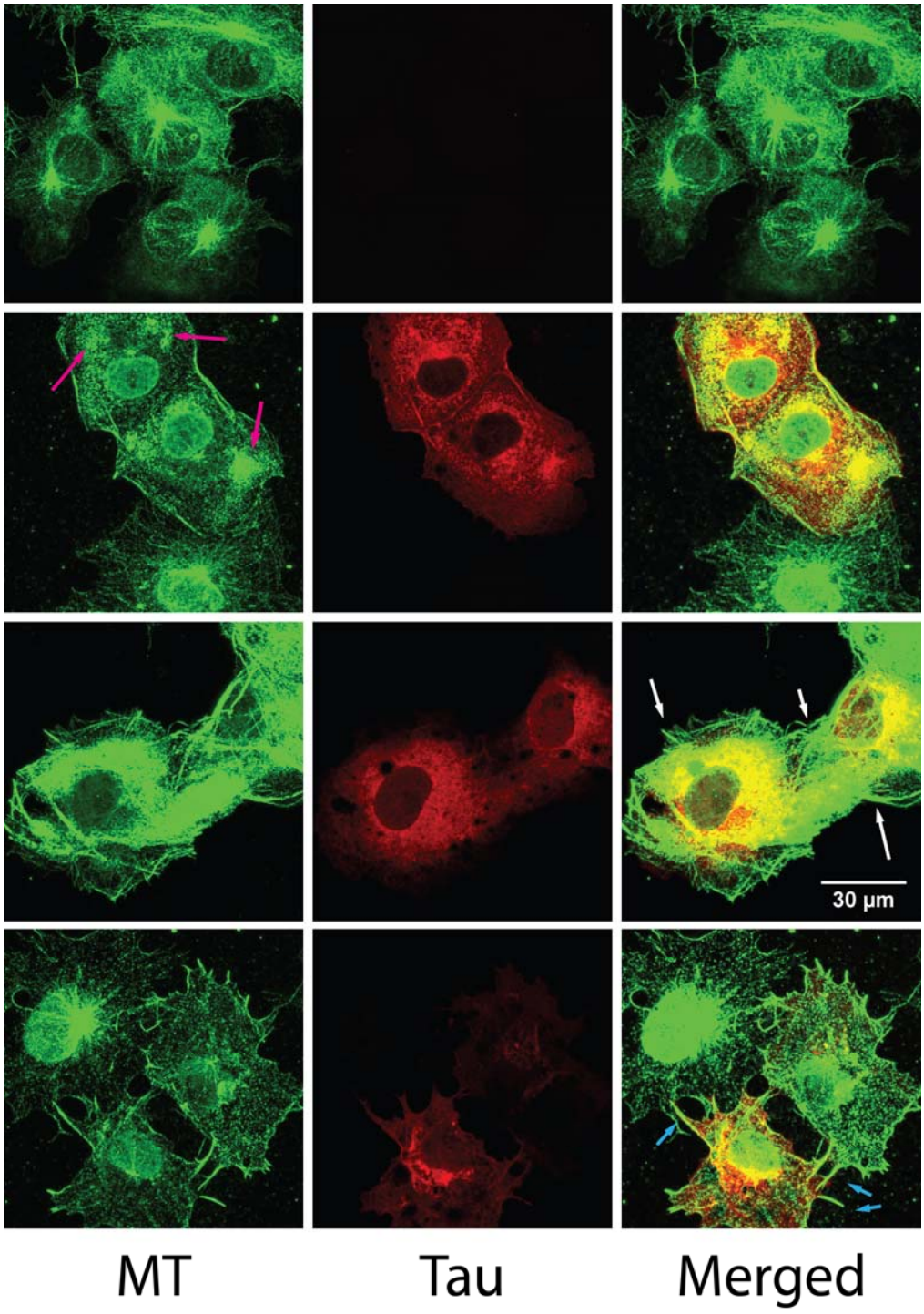

Figure 6-2: Representative immunofluorescence images of COS-7 cells. The addition of tau caused disruptions in the microtubule network. Row 1 (No tau) shows regular microtubule networks in COS-7 cells. Row 2 (4RS WT day 1) shows signs of unpolymerized tubulin aggregations (magenta arrows). Row 3 (4RS R406W Day 2) shows formations of thick microtubule bundles in near cell peripheries (white arrows). Row 4 (4RS ΔN296 Day 1) shows formations of microtubule bundle do "processes" (light blue arrows).

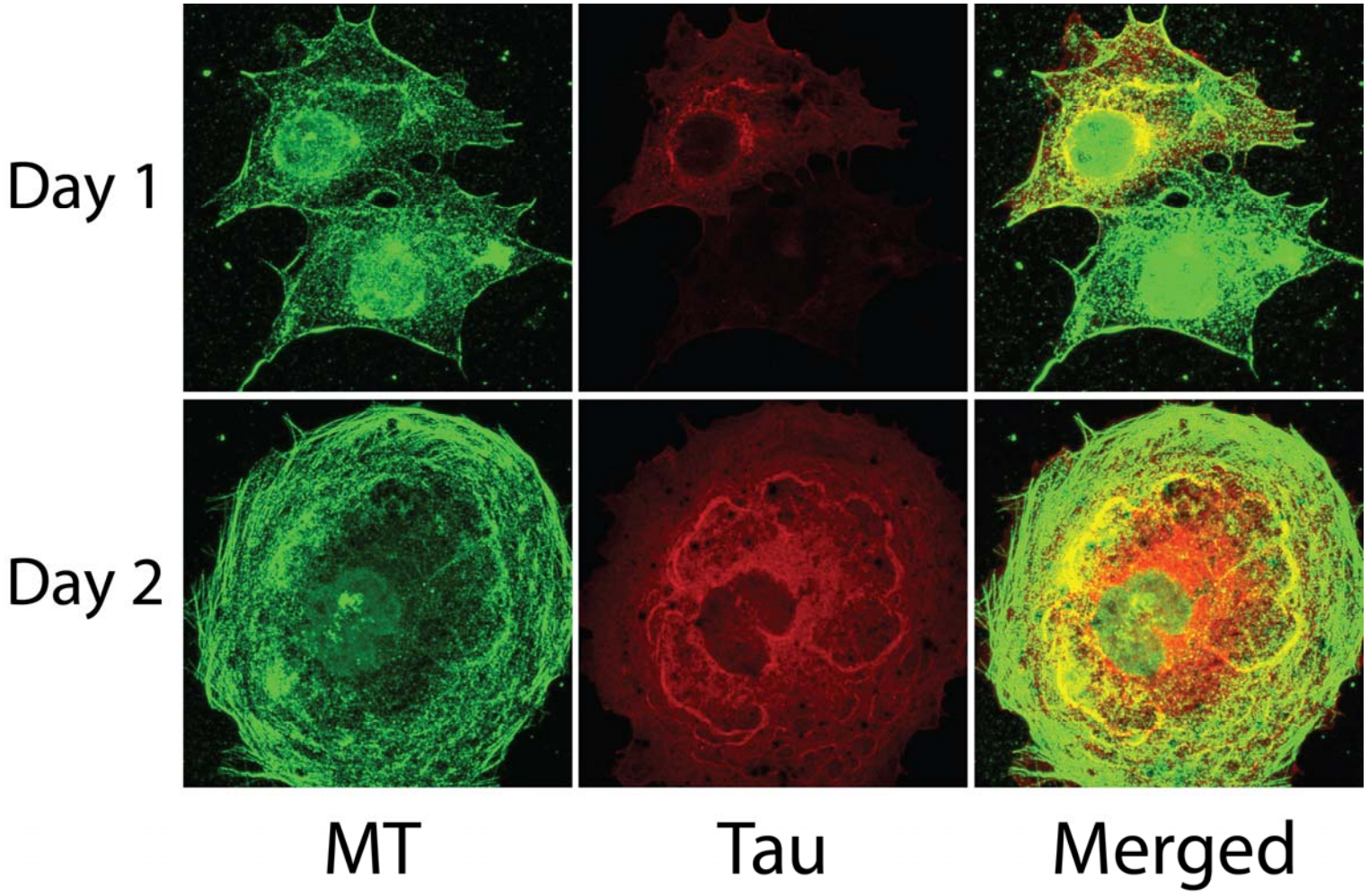

Figure 6-3: Microtubule network morphology comparisons between 1-day and 2-day post-transfection in COS-7 cells. Cell that was transfected with tau (4RS P301L) for two days (Row 2) displayed more prominent bundling of microtubules near cell periphery and had more tubulin/microtubule content in the cell compared to cells that were transfected with tau for one day.

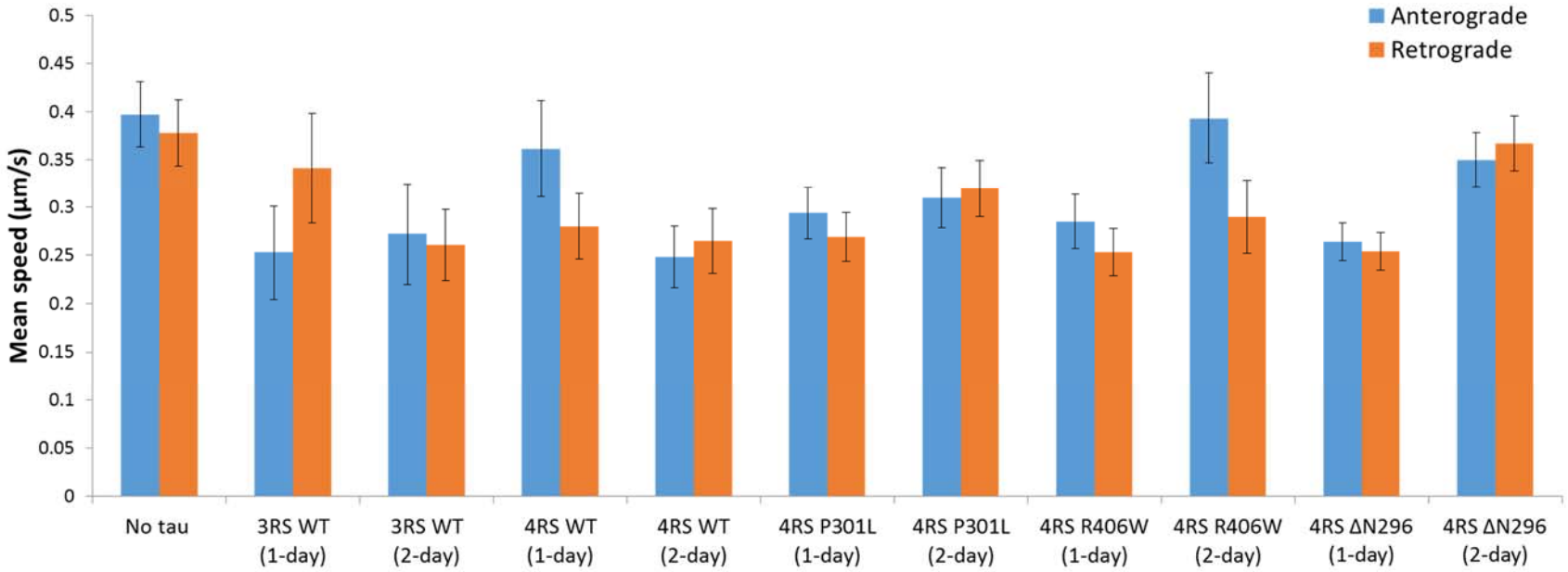

Figure 6-3: Mean velocities of lysosomes transported directionally in anterograde and retrograde directions. Trajectories of selected lysosomes were divided into runs that were categorized as anterograde (+, toward cell periphery) or retrograde (-, toward cell center) based on the direction of the particle motion with respect to the center of the cell. The average velocity of each run was displayed above (N = 19 -106). Error bars are SEM.

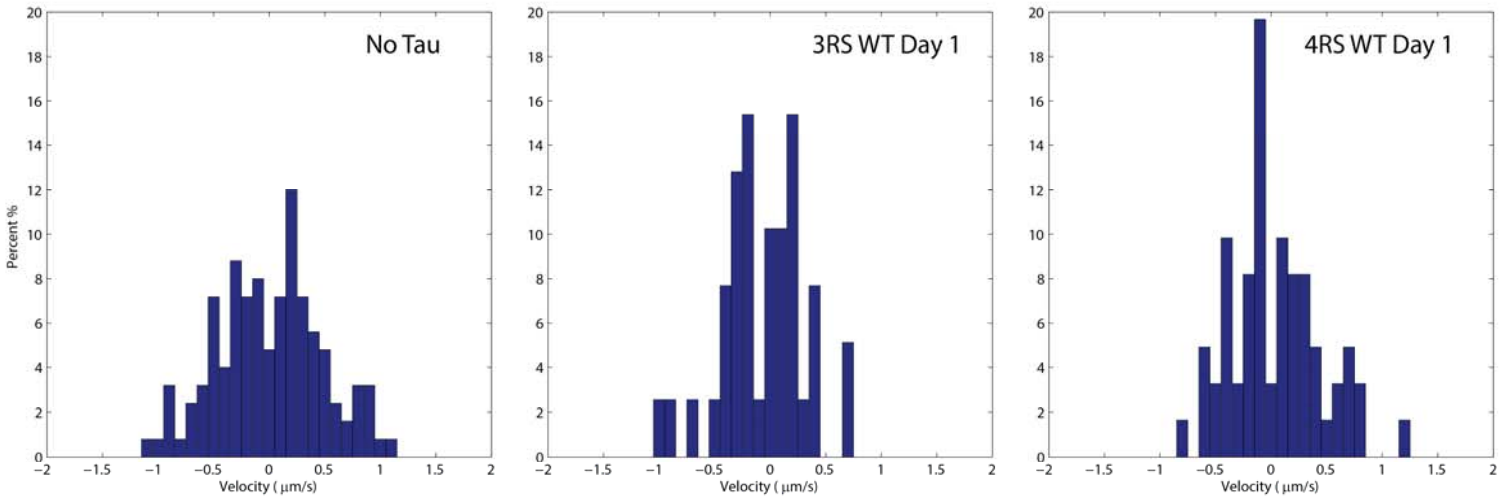

Figure S6-1: Average lysosome velocity distributions for cells that had no tau, 3RS WT tau and 4RS WT tau 1-day after transfection. Velocities in the anterograde (towards cell periphery) direction are positive, and velocities in the retrograde (towards cell center) direction are negative.

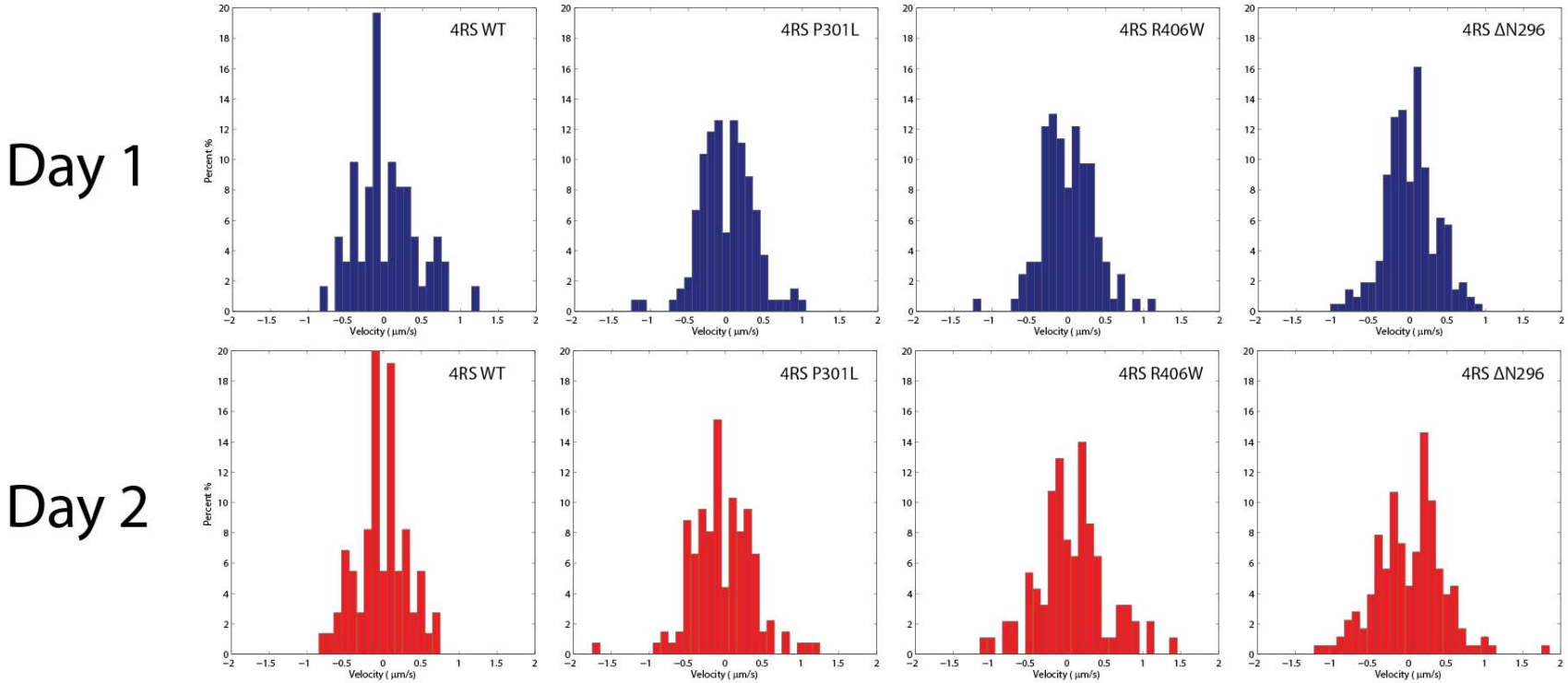

Figure S6-2: Average lysosome velocity distributions for in cells that were transfected with 4-repeat wild-type and mutant tau for one and two days. Velocities in the anterograde (towards cell periphery) direction are positive, and velocities in the retrograde (towards cell center) direction are negative.

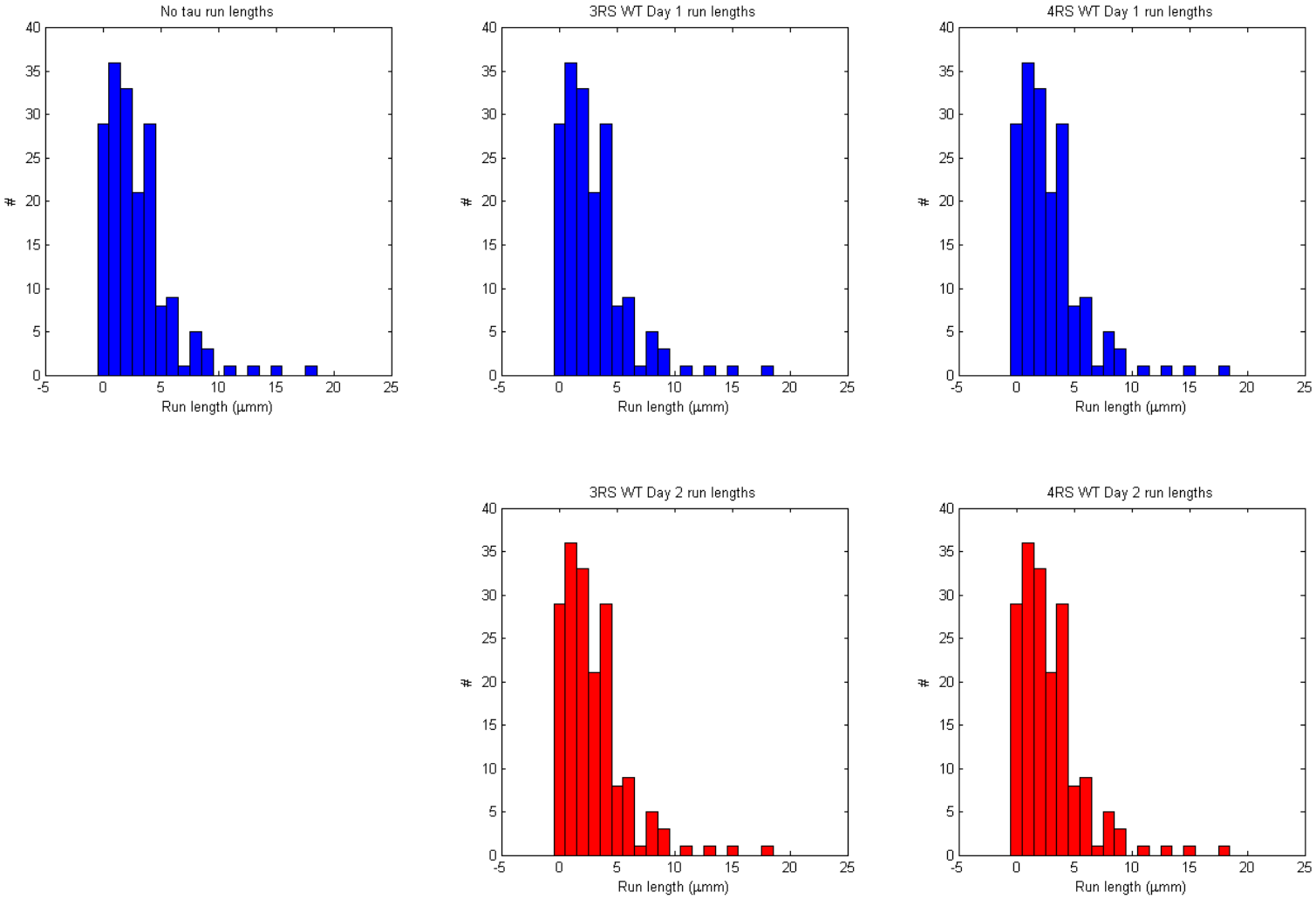

Figure S6-3: Lysosome run lengths distributions for COS-7 cells with no tau and cells transfected with 3RS and 4RS wild-type tau

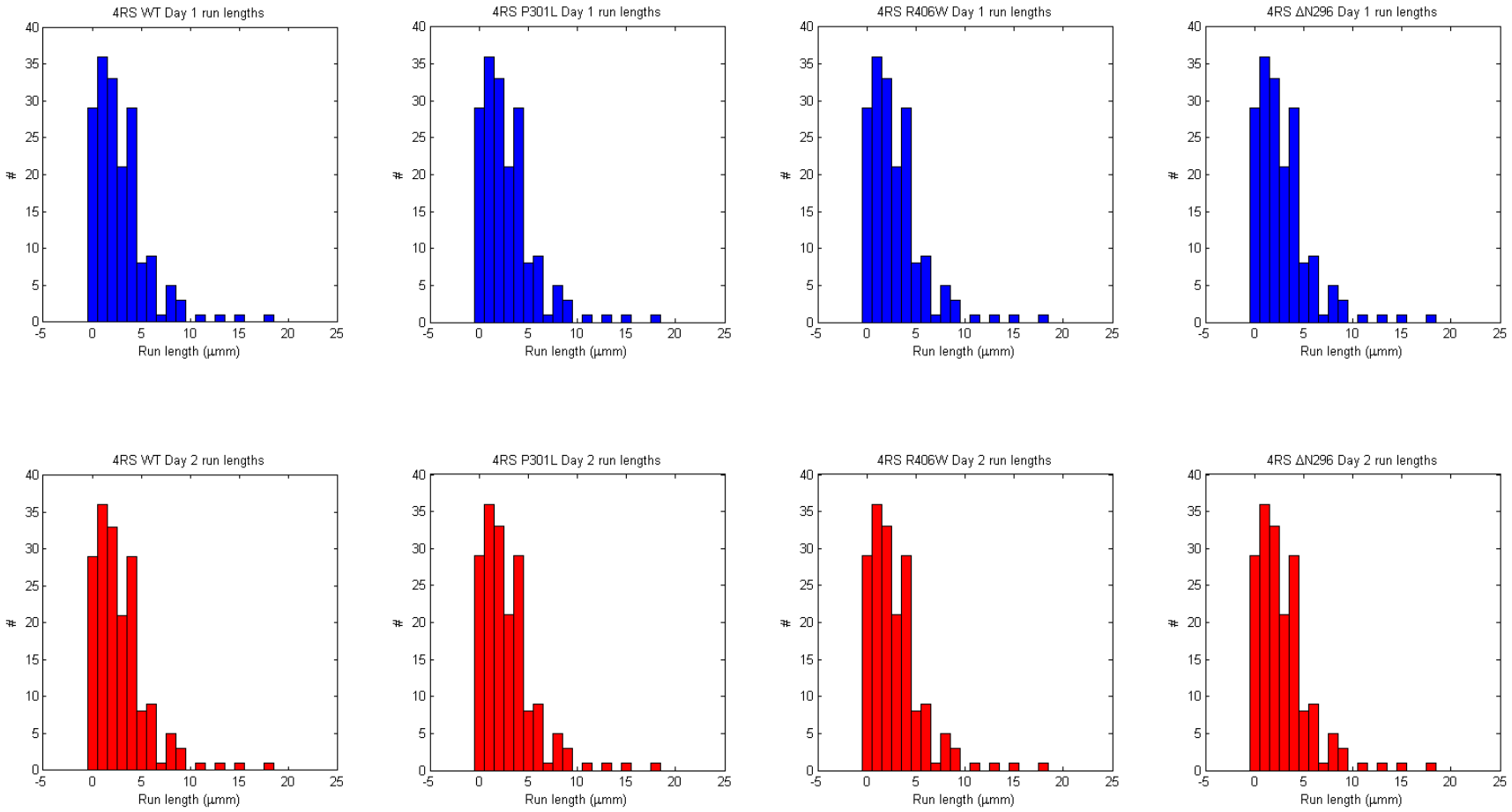

Figure S6-4: Lysosome run lengths distributions for tau-transfected (4RS WT, 4RS P301L, 4RS R406W and 4RS ΔN296) cells

Table 6-1: Statistical Analysis of Lysosome Velocities			
Condtion 1	**Condition 2**	**h, anterograde**	**h, retrograde**
No Tau	3RS WT Day 1	0	0
No Tau	4RS WT Day 1	0	0
No Tau	4RS P301L Day 1	0	1
No Tau	4RS R406W Day 1	1	1
No Tau	4RS ΔN296 Day 1	1	1
No Tau	3RS WT Day 2	1	1
No Tau	4RS WT Day 2	1	1
No Tau	4RS P301L Day 2	0	0
No Tau	4RS R406W Day 2	0	1
No Tau	4RS ΔN296 Day 2	0	0
3RS WT Day 1	4RS WT Day 1	0	0
3RS WT Day 1	4RS P301L Day 1	0	0
3RS WT Day 1	4RS R406W Day 1	0	0
3RS WT Day 1	4RS ΔN296 Day 1	0	0
3RS WT Day 1	3RS WT Day 2	0	0
3RS WT Day 1	4RS WT Day 2	0	0
3RS WT Day 1	4RS P301L Day 2	0	0
3RS WT Day 1	4RS R406W Day 2	0	0
3RS WT Day 1	4RS ΔN296 Day 2	0	0
4RS WT Day 1	4RS P301L Day 1	0	0
4RS WT Day 1	4RS R406W Day 1	0	0
4RS WT Day 1	4RS ΔN296 Day 1	0	0
4RS WT Day 1	3RS WT Day 2	0	0
4RS WT Day 1	4RS WT Day 2	0	0
4RS WT Day 1	4RS P301L Day 2	0	0
4RS WT Day 1	4RS R406W Day 2	0	0
4RS WT Day 1	4RS ΔN296 Day 2	0	0
4RS P301L Day 1	4RS R406W Day 1	0	0
4RS P301L Day 1	4RS ΔN296 Day 1	0	0
4RS P301L Day 1	3RS WT Day 2	0	0
4RS P301L Day 1	4RS WT Day 2	0	0
4RS P301L Day 1	4RS P301L Day 2	0	0
4RS P301L Day 1	4RS R406W Day 2	0	0
4RS P301L Day 1	4RS ΔN296 Day 2	0	0
4RS R406W Day 1	4RS ΔN296 Day 2	0	0
4RS R406W Day 1	3RS WT Day 2	0	0
4RS R406W Day 1	4RS WT Day 2	0	0
4RS R406W Day 1	4RS P301L Day 2	0	0
4RS R406W Day 1	4RS R406W Day 2	0	0

4RS R406W Day 1	4RS ΔN296 Day 2	0	1
4RS ΔN296 Day 1	3RS WT Day 2	0	0
4RS ΔN296 Day 1	4RS WT Day 2	0	0
4RS ΔN296 Day 1	4RS P301L Day 2	0	1
4RS ΔN296 Day 1	4RS R406W Day 2	1	0
4RS ΔN296 Day 1	4RS ΔN296 Day 2	1	1
3RS WT Day 2	4RS WT Day 2	0	0
3RS WT Day 2	4RS P301L Day 2	0	0
3RS WT Day 2	4RS R406W Day 2	0	0
3RS WT Day 2	4RS ΔN296 Day 2	1	1
4RS WT Day 2	4RS P301L Day 2	0	0
4RS WT Day 2	4RS R406W Day 2	1	0
4RS WT Day 2	4RS ΔN296 Day 2	1	1
4RS P301L Day 2	4RS R406W Day 2	0	0
4RS P301L Day 2	4RS ΔN296 Day 2	0	0
4RS R406W Day 2	4RS ΔN296 Day 2	0	1

A two-sample Kolmogorov-Smirnov test (MATLAB) is used to analyze the statistical differences of lysosome velocities between different conditions. A *h* value of 1 indicates a significant difference at 95% confidence level.

D. Discussion

Intracellular transport is an essential biological process that facilitates and regulates the basic functions of a cell. Its role is even more prominent in polarized cell types with long extended features such neurons, where important cargos are required to be transported over large distances that would be impossible to achieve efficiently with random diffusion alone. Many believed that disruptions in axonal transport could lead to full-blown neurodegenerative dementia such as Alzheimer's and Parkinson's [8, 10, 27, 29]. Thus, extensive research have been conducted on the basis of intracellular transport from *in vitro* single molecule/filament studies on protein motors and microtubule mechanics to *in vivo* studies on collective transports in model cells. Microtubule binding protein tau was identified as a major contributor to the regulation of microtubule structures and motor protein transport behaviors. Abnormal expressions and defects of tau were found to disrupt motor translocations *in vitro* and *in vivo* with mechanisms that were not fully understood, but many believed that tau proteins interfere by forming physical blockages on MT filaments [7-9].

In this study, we examined the effects of six different wild-type and mutant tau constructs (3RS WT, 4RS WT, 4RS P301L, 4RS R406W, and 4RS ΔN296) on MT network morphology and of motor-driven transport properties using COS-7 cells. We observed three main phenotypes: 1) formation of bundles (often near the cell peripheries), 2) punctate aggregations of what we believe to be non-filamentous tubulins or short tubulin oligomers, and 3) formation of "axon-like" "processes" (Figure 6-2). These phenotypes were found in all tau-expressing COS-7 cells, and interestingly we did not notice any significant differences between the different tau constructs. With these dramatic reorganizations in the MT network

structure, one might expect interferences, and inhibitions in intracellular transports, which could lead to chemical imbalance and cell death.

Using fluorescence microscopy in combination with advanced image analysis techniques, we assessed the effect of tau on the velocities of motor-driven lysosome translocations in the COS-7 cells. Surprisingly, despite the massive reorganization in the MT networks, the lysosome velocities in tau-expressing cells were not significantly different than that in control cells without transfections. We were additionally surprised that there was no significant difference between the velocities anterograde and retrograde transports, which presumably were driven by different families of motor proteins. Previous *in vitro* single molecule studies showed that kinesins and dyneins have different molecular structures, different stepping behavior and different regulations in the presence of tau [7, 136, 137]. Thus, we did not expect kinesins and dyneins to behave the same way when encountered tau or other types of microtubule binding proteins. However, there was no evidence in our study showing differential modifications by tau on transports of different directions. Although the molecular mechanism was not well-understood, prior studies often described the behavior of *in vivo* bidirectional cargo transports as a tug-of-war between competing motors [138-141]. Therefore, it is possible that the differential effects of tau on individual motors were masked by some strange tug-of-war interactions on the multi-motor-bound lysosomes. Another possible explanation is that our ability to determine the direction of lysosome motions in tau-expressing COS-7 cells was compromised by the reorganization of MT networks, where the often radial directions of lysosome motion in “wheel-like” networks confounded our assignment of motor direction compared to assignments made in the “aster-like” networks we

normally found in non-transfected cells. Separate fluorescent labeling of the MT filaments in the live-cell experiments could help to better determine the directions of the lysosome motions. However, based on the immunofluorescence images that we obtained, the densities of the MT filaments in some of the "wheel-like" networks, especially on Day 2, were so high that it would be difficult to distinguish the correct direction of a moving lysosome even with fluorescently labeled MTs.

One would also expect the average velocities to be hampered incrementally as we increased the time post-transfection with presumably higher expressions of tau proteins for longer waiting times. However, for some of the mutants (noticeably for 4RS R406W and 4RS ΔN296), we observed higher average velocities on Day 2 post-transfection than Day 1. The underlying mechanism of the recovery in velocities was not understood, but we can offer several possible causes. It is possible that some of these tau mutants lose their effectiveness to regulate the intracellular transport system over time, which allow the native regulation mechanisms in the COS-7 cells to restore and recover. This may be supported with our observation of higher tubulin/microtubule contents in tau-transfected cells on the second day (Figure 6-3). On the other hand, we would not rule out the possibility that this apparent recovery was an artifact arising from selection bias, where cells with high tau expression might be so sick two days post-transfection that most or all active cargo transports were so severely disrupted that the only cells that were selected for measurement were those cells that were either more tolerant against the effects of tau, or those that had slower expression of tau. Instead of looking at time dependence effects of tau expression on intracellular transport, it will be interesting for future experiments to quantitatively examine the relationship between

expression level of tau and its effect on cargo transport. This will provide tremendous insights on not only how neurodegenerative diseases are developed, but also shed light on how the progression and severity of the disease are related to the level of tau misregulations.

In summary, we find the addition of tau in natively tau-absent cellular system will cause undesirable disruption and misregulations on the intracellular transport system despite use of a normal wild-type tau construct. Although we saw little to no effects of tau on lysosome transports in COS-7 cells in terms of cargo velocity, we believe that the distributions of important organelles were significantly modified due to the changes in MT network orientations. These alterations on the delicate intracellular regulation system can possibly lead to detrimental effects to the well-being of the cells.

VI. Conclusion

In this research, we tested the effect of microtubule binding tau protein on the microtubule mechanics and molecular motor transports in both simplified *in vitro* settings and a more complex cellular system. We had successfully developed useful experimental tools to examine the material and functional properties of microtubule. Using these tools, we were able to measure the mechanical stiffness of microtubules with great confidence and observe changes in their mechanics under different chemical conditions. We gained tremendous insight on the determining factors of microtubule mechanics and how we can control and modify its material properties in controlled laboratory settings. In addition, we explored how the functional properties in terms of cellular transport may be related to these changes in microtubule mechanics / structures. We also examined the effects some of the less common microtubule stabilizing molecules and proteins such as epothilone-A and –B molecules, and tau mutants P301L, R406W and ΔN296, which are related to specific neurodegenerative disease. Our studies provides important additional mechanical and functional information of these molecules / proteins to the forever expanding list of microtubule stabilizers.

Even though we had found interesting effects of tau on the mechanical properties and functional properties of microtubules and intracellular transport, the underlying molecular mechanism is still not well understood. There are many speculations in the field on how tau interacts and alters microtubule structure and molecular motor translocations along microtubules. For a long time, many scientists and biologists believed that tau proteins are tightly-bound proteins that binds to the surface of microtubules and stabilize microtubule dynamics [40, 43]. Many also suggest that those tau proteins that were bound on the

microtubule surface act like physical roadblocks and restrict motor transport [7]. However, our microtubule mechanics studies and studies by other suggest that tau proteins do not simply bind to the outer surface of microtubule but they are also capable to alter the lattice interactions and structure in various assembly conditions [6, 100]. Recent studies also found evidence of tau diffusion along mircrotubules which further complicate the interactions between tau and microtubule-associated motors [142, 143]. Yet there is a lack of unified consensus models on these interactions. We believe that the understanding of the molecular mechanisms is crucial for future researches on developing next generation active biomaterials and finding possible cures for many neurodegenerative dementias. In order to tackle this problem, improvements on high-resolution imaging techniques will be needed in combination with sophisticated computer simulations and creative collaborations joining expertise across different fields. These studies will open up new ideas and examine various molecular interactions in greater detail than are achievable using our more traditional experimental methods. In particular, super-resolution structural analyses, such as cryo-EM and STORM, will be extremely helpful. Cryo-EM studies are capable of measuring the fine structural changes in the microtubule lattices and network geometry in various environments. On the other hand Stochastic optical reconstruction microscopy or STORM gives real-time, dynamic data of microtubules in aqueous environments and has the resolution to monitor cargo motions on such finer spatial and temporal scales [144-146]. Future studies using these tools will help improve theoretical models for microtubule mechanics and motor stepping behaviors, and collaborations to tackle these important issues are now being formed. Lastly, it would be fascinating to further investigate the detailed interactions between molecular motors on multi-motor cargoes using a combinations of advanced single-molecule methods

and computer simulations. These studies will provide insightful information on how different motors, such as kinesin and dyneins, on cellular cargos cooperate and communicate in order to accomplish essential tasks such as cellular transport along MAP-coated MTs in an efficient manner.

For the cellular work, an important future direction is the development of cell culture lines that more accurately mimic the human disease state for biophysical and biochemical experiments. This is particularly important for studies of tau, where the isoform distribution and regulation can be significantly different among different species. For example, six isoforms of wild-type tau proteins can be found in the human central nervous system, whereas adult mouse brain only contains exclusively 4-repeat isoforms, an expression profile that would be fatal in humans [147]. Thus, we expect that the effects disease-related tau mutants and the disease phenotypes could be dramatically different in primary neurons harvested from rodents, not to mention other non-neuronal cell lines, compared to real human nerve cells. Fortunately, the recent progressions in stem cell technology are bringing the promising hopes of producing suitable human-derived cell types for many biomedical, biophysical andpharmaceutical research in the near future.

With technology improving in all facets in the field of science, it will be only a matter of time for us to fully understand the effect of tau on microtubule structure and molecular motor transport from molecular mechanism, to collective function and larger scale cellular impacts.

VII. References

1. Mitchison, T. and M. Kirschner, *Dynamic instability of microtubule growth.* Nature, 1984. **312**(5991): p. 237-42.
2. Wilson, L., et al., *Taxol stabilization of microtubules in vitro: dynamics of tubulin addition and loss at opposite microtubule ends.* Biochemistry, 1985. **24**(19): p. 5254-62.
3. Downing, K.H. and E. Nogales, *Tubulin structure: insights into microtubule properties and functions.* Curr Opin Struct Biol, 1998. **8**(6): p. 785-91.
4. Nogales, E., et al., *Structure of tubulin at 6.5 A and location of the taxol-binding site.* Nature, 1995. **375**(6530): p. 424-7.
5. Nogales, E., et al., *High-resolution model of the microtubule.* Cell, 1999. **96**(1): p. 79-88.
6. Choi, M.C., et al., *Human microtubule-associated-protein tau regulates the number of protofilaments in microtubules: a synchrotron x-ray scattering study.* Biophys J, 2009. **97**(2): p. 519-27.
7. Dixit, R., et al., *Differential regulation of dynein and kinesin motor proteins by tau.* Science, 2008. **319**(5866): p. 1086-9.
8. Stamer, K., et al., *Tau blocks traffic of organelles, neurofilaments, and APP vesicles in neurons and enhances oxidative stress.* J Cell Biol, 2002. **156**(6): p. 1051-63.
9. Yu, D., et al., *Tau Proteins Harboring Neurodegeneration-Linked Mutations Impair Kinesin Translocation in vitro.* Journal of Alzheimer's Disease, 2014. **39**(2): p. 301-314.
10. Ballatore, C., V.M. Lee, and J.Q. Trojanowski, *Tau-mediated neurodegeneration in Alzheimer's disease and related disorders.* Nat Rev Neurosci, 2007. **8**(9): p. 663-72.
11. Caceres, A., S. Potrebic, and K.S. Kosik, *The effect of tau antisense oligonucleotides on neurite formation of cultured cerebellar macroneurons.* J Neurosci, 1991. **11**(6): p. 1515-23.
12. Esmaeli-Azad, B., J.H. McCarty, and S.C. Feinstein, *Sense and antisense transfection analysis of tau function: tau influences net microtubule assembly, neurite outgrowth and neuritic stability.* J Cell Sci, 1994. **107 (Pt 4)**: p. 869-79.
13. Takei, Y., et al., *Defects in axonal elongation and neuronal migration in mice with disrupted tau and map1b genes.* J Cell Biol, 2000. **150**(5): p. 989-1000.
14. Huang, Y. and L. Mucke, *Alzheimer mechanisms and therapeutic strategies.* Cell, 2012. **148**(6): p. 1204-22.
15. Lee, G. and C.J. Leugers, *Tau and tauopathies.* Prog Mol Biol Transl Sci, 2012. **107**: p. 263-93.
16. Hutton, M., et al., *Association of missense and 5'-splice-site mutations in tau with the inherited dementia FTDP-17.* Nature, 1998. **393**(6686): p. 702-5.
17. Hong, M., et al., *Mutation-specific functional impairments in distinct tau isoforms of hereditary FTDP-17.* Science, 1998. **282**(5395): p. 1914-7.
18. Clark, L.N., et al., *Pathogenic implications of mutations in the tau gene in pallido-ponto-nigral degeneration and related neurodegenerative disorders linked to chromosome 17.* Proc Natl Acad Sci U S A, 1998. **95**(22): p. 13103-7.

19. Spillantini, M.G., et al., *Mutation in the tau gene in familial multiple system tauopathy with presenile dementia.* Proc Natl Acad Sci U S A, 1998. **95**(13): p. 7737-41.
20. Spillantini, M., et al., *A novel tau mutation (N296N) in familial dementia with swollen achromatic neurons and corticobasal inclusion bodies.* Annals of Neurology, 2000. **48**(6): p. 939-943.
21. Himmler, A., et al., *Tau consists of a set of proteins with repeated C-terminal microtubule-binding domains and variable N-terminal domains.* Mol Cell Biol, 1989. **9**(4): p. 1381-8.
22. Kosik, K.S., et al., *Developmentally regulated expression of specific tau sequences.* Neuron, 1989. **2**(4): p. 1389-1397.
23. Himmler, A., *Structure of the bovine tau gene: alternatively spliced transcripts generate a protein family.* Mol Cell Biol, 1989. **9**(4): p. 1389-96.
24. Morfini, G.A., et al., *Axonal transport defects in neurodegenerative diseases.* J Neurosci, 2009. **29**(41): p. 12776-86.
25. Sheng, Z.-H. and Q. Cai, *Mitochondrial transport in neurons: impact on synaptic homeostasis and neurodegeneration.* Nat Rev Neurosci, 2012. **13**(2): p. 77-93.
26. Stokin, G.B., et al., *Axonopathy and transport deficits early in the pathogenesis of Alzheimer's disease.* Science, 2005. **307**(5713): p. 1282-8.
27. Ebneth, A., et al., *Overexpression of tau protein inhibits kinesin-dependent trafficking of vesicles, mitochondria, and endoplasmic reticulum: implications for Alzheimer's disease.* J Cell Biol, 1998. **143**(3): p. 777-94.
28. Trinczek, B., et al., *Tau regulates the attachment/detachment but not the speed of motors in microtubule-dependent transport of single vesicles and organelles.* J Cell Sci, 1999. **112 (Pt 14)**: p. 2355-67.
29. Mandelkow, E.M., et al., *Clogging of axons by tau, inhibition of axonal traffic and starvation of synapses.* Neurobiol Aging, 2003. **24**(8): p. 1079-85.
30. Spittaels, K., et al., *Prominent axonopathy in the brain and spinal cord of transgenic mice overexpressing four-repeat human tau protein.* Am J Pathol, 1999. **155**(6): p. 2153-65.
31. Yuan, A., et al., *Axonal Transport Rates In Vivo Are Unaffected by Tau Deletion or Overexpression in Mice.* The Journal of Neuroscience, 2008. **28**(7): p. 1682-1687.
32. Morfini, G., et al., *Tau binding to microtubules does not directly affect microtubule-based vesicle motility.* J Neurosci Res, 2007. **85**(12): p. 2620-30.
33. Seitz, A., et al., *Single-molecule investigation of the interference between kinesin, tau and MAP2c.* Embo J, 2002. **21**(18): p. 4896-905.
34. Vershinin, M., et al., *Multiple-motor based transport and its regulation by Tau.* Proc Natl Acad Sci U S A, 2007. **104**(1): p. 87-92.
35. Lee, G., N. Cowan, and M. Kirschner, *The primary structure and heterogeneity of tau protein from mouse brain.* Science, 1988. **239**(4837): p. 285-8.
36. Gustke, N., et al., *Domains of tau Protein and Interactions with Microtubules.* Biochemistry, 1994. **33**(32): p. 9511-9522.
37. Goode, B.L. and S.C. Feinstein, *Identification of a novel microtubule binding and assembly domain in the developmentally regulated inter-repeat region of tau.* J Cell Biol, 1994. **124**(5): p. 769-82.

38. Hirokawa, N., Y. Shiomura, and S. Okabe, *Tau proteins: the molecular structure and mode of binding on microtubules.* J Cell Biol, 1988. **107**(4): p. 1449-59.
39. Butner, K.A. and M.W. Kirschner, *Tau protein binds to microtubules through a flexible array of distributed weak sites.* J Cell Biol, 1991. **115**(3): p. 717-30.
40. Panda, D., et al., *Kinetic stabilization of microtubule dynamics at steady state by tau and microtubule-binding domains of tau.* Biochemistry, 1995. **34**(35): p. 11117-27.
41. Chen, J., et al., *Projection domains of MAP2 and tau determine spacings between microtubules in dendrites and axons.* Nature, 1992. **360**(6405): p. 674-7.
42. Diaz, J.F., et al., *Changes in microtubule protofilament number induced by Taxol binding to an easily accessible site. Internal microtubule dynamics.* J Biol Chem, 1998. **273**(50): p. 33803-10.
43. Panda, D., et al., *Differential regulation of microtubule dynamics by three- and four-repeat tau: implications for the onset of neurodegenerative disease.* Proc Natl Acad Sci U S A, 2003. **100**(16): p. 9548-53.
44. Derry, W.B., L. Wilson, and M.A. Jordan, *Substoichiometric binding of taxol suppresses microtubule dynamics.* Biochemistry, 1995. **34**(7): p. 2203-11.
45. Muto, E., H. Sakai, and K. Kaseda, *Long-range cooperative binding of kinesin to a microtubule in the presence of ATP.* J Cell Biol, 2005. **168**(5): p. 691-6.
46. Xiao, H., et al., *Insights into the mechanism of microtubule stabilization by Taxol.* Proc Natl Acad Sci U S A, 2006. **103**(27): p. 10166-73.
47. Krebs, A., K.N. Goldie, and A. Hoenger, *Complex formation with kinesin motor domains affects the structure of microtubules.* J Mol Biol, 2004. **335**(1): p. 139-53.
48. Hawkins, T.L., et al., *Mechanical properties of doubly stabilized microtubule filaments.* Biophys J, 2013. **104**(7): p. 1517-28.
49. McVicker, D.P., L.R. Chrin, and C.L. Berger, *The Nucleotide-binding State of Microtubules Modulates Kinesin Processivity and the Ability of Tau to Inhibit Kinesin-mediated Transport.* Journal of Biological Chemistry, 2012. **286**(50): p. 42873-42880.
50. Peck, A., et al., *Tau isoform-specific modulation of kinesin-driven microtubule gliding rates and trajectories as determined with tau-stabilized microtubules.* Cytoskeleton, 2011. **68**(1): p. 44-55.
51. Miller, H.P. and L. Wilson, *Preparation of Microtubule Protein and Purified Tubulin from Bovine Brain by Cycles of Assembly and Disassembly and Phosphocellulose Chromatography*, in *Methods in Cell Biology*, L. Wilson, Correia, J.J., Editor. 2010, Elsevier Inc. p. 3-15.
52. Hyman, A., et al., *Preparation of modified tubulins.* Methods Enzymol, 1991. **196**: p. 478-85.
53. Levy, S.F., et al., *Three- and four-repeat tau regulate the dynamic instability of two distinct microtubule subpopulations in qualitatively different manners. Implications for neurodegeneration.* J Biol Chem, 2005. **280**(14): p. 13520-8.
54. Rice, S., et al., *A structural change in the kinesin motor protein that drives motility.* Nature, 1999. **402**(6763): p. 778-84.
55. Case, R.B., et al., *The directional preference of kinesin motors is specified by an element outside of the motor catalytic domain.* Cell, 1997. **90**(5): p. 959-66.
56. Thompson, W.C., L. Wilson, and D.L. Purich, *Taxol induces microtubule assembly at low temperature.* Cell Motil, 1981. **1**(4): p. 445-54.

57. Yildiz, A., et al., *Intramolecular Strain Coordinates Kinesin Stepping Behavior along Microtubules.* Cell, 2008. **134**(6): p. 1030-1041.
58. Brangwynne, C.P., et al., *Bending Dynamics of Fluctuating Biopolymers Probed by Automated High-Resolution Filament Tracking.* Biophysical Journal, 2007. **93**(1): p. 346-359.
59. Valdman, D., et al., *Spectral analysis methods for the robust measurement of the flexural rigidity of biopolymers.* Biophysical journal, 2012. **102**(5): p. 1144-1153.
60. Binder, L.I., A. Frankfurter, and L.I. Rebhun, *The distribution of tau in the mammalian central nervous system.* J Cell Biol, 1985. **101**(4): p. 1371-8.
61. Drubin, D.G., et al., *Nerve growth factor-induced neurite outgrowth in PC12 cells involves the coordinate induction of microtubule assembly and assembly-promoting factors.* J Cell Biol, 1985. **101**(5 Pt 1): p. 1799-807.
62. Leibler, S. and D.A. Huse, *Porters versus rowers: a unified stochastic model of motor proteins.* The Journal of Cell Biology, 1993. **121**(6): p. 1357-1368.
63. Maccioni, R.B., et al., *The role of neuroimmunomodulation in Alzheimer's disease.* Ann N Y Acad Sci, 2009. **1153**: p. 240-6.
64. Trinczek, B., et al., *Domains of tau protein, differential phosphorylation, and dynamic instability of microtubules.* Mol Biol Cell, 1995. **6**(12): p. 1887-902.
65. Lee, G., R.L. Neve, and K.S. Kosik, *The microtubule binding domain of tau protein.* Neuron, 1989. **2**(6): p. 1615-24.
66. Delobel, P., et al., *Functional characterization of FTDP-17 tau gene mutations through their effects on Xenopus oocyte maturation.* J Biol Chem, 2002. **277**(11): p. 9199-205.
67. LeBoeuf, A.C., et al., *FTDP-17 mutations in tau alter the regulation of microtubule dynamics - an "Alternative Core" model for normal and pathological tau action.* J Biol Chem, 2008. **283**(52): p. 36406-36415.
68. Bunker, J.M., et al., *FTDP-17 mutations compromise the ability of tau to regulate microtubule dynamics in cells.* J Biol Chem, 2006. **281**(17): p. 11856-63.
69. Goode, B.L., et al., *Structural and functional differences between 3-repeat and 4-repeat tau isoforms. Implications for normal tau function and the onset of neurodegenetative disease.* J Biol Chem, 2000. **275**(49): p. 38182-9.
70. Keskin, O., et al., *Relating molecular flexibility to function: a case study of tubulin.* Biophys J, 2002. **83**(2): p. 663-80.
71. Drechsel, D.N., et al., *Modulation of the dynamic instability of tubulin assembly by the microtubule-associated protein tau.* Mol Biol Cell, 1992. **3**(10): p. 1141-54.
72. Kar, S., et al., *Repeat motifs of tau bind to the insides of microtubules in the absence of taxol.* Embo J, 2003. **22**(1): p. 70-7.
73. Brunden, K.R., et al., *Epothilone D Improves Microtubule Density, Axonal Integrity, and Cognition in a Transgenic Mouse Model of Tauopathy.* The Journal of Neuroscience, 2010. **30**(41): p. 13861-13866.
74. Zhang, B., et al., *The Microtubule-Stabilizing Agent, Epothilone D, Reduces Axonal Dysfunction, Neurotoxicity, Cognitive Deficits, and Alzheimer-Like Pathology in an Interventional Study with Aged Tau Transgenic Mice.* The Journal of Neuroscience, 2012. **32**(11): p. 3601-3611.
75. Fletcher, D.A. and R.D. Mullins, *Cell mechanics and the cytoskeleton.* Nature, 2010. **463**(7280): p. 485-92.

76. Felgner, H., et al., *Domains of neuronal microtubule-associated proteins and flexural rigidity of microtubules.* J Cell Biol, 1997. **138**(5): p. 1067-75.
77. Felgner, H., R. Frank, and M. Schliwa, *Flexural rigidity of microtubules measured with the use of optical tweezers.* J Cell Sci, 1996. **109 (Pt 2)**: p. 509-16.
78. Gittes, F., et al., *Flexural rigidity of microtubules and actin filaments measured from thermal fluctuations in shape.* The Journal of Cell Biology, 1993. **120**(4): p. 923-934.
79. Janson, M.E. and M. Dogterom, *A bending mode analysis for growing microtubules: evidence for a velocity-dependent rigidity.* Biophys J, 2004. **87**(4): p. 2723-36.
80. Mickey, B. and J. Howard, *Rigidity of microtubules is increased by stabilizing agents.* The Journal of Cell Biology, 1995. **130**(4): p. 909-917.
81. van Mameren, J., et al., *Leveraging single protein polymers to measure flexural rigidity.* J Phys Chem B, 2009. **113**(12): p. 3837-44.
82. Nogales, E., S.G. Wolf, and K.H. Downing, *Structure of the alpha beta tubulin dimer by electron crystallography.* Nature, 1998. **391**(6663): p. 199-203.
83. Wang, H.W. and E. Nogales, *Nucleotide-dependent bending flexibility of tubulin regulates microtubule assembly.* Nature, 2005. **435**(7044): p. 911-5.
84. Bohm, K.J., et al., *Effect of microtubule-associated proteins on the protofilament number of microtubules assembled in vitro.* Biochim Biophys Acta, 1984. **800**(2): p. 119-26.
85. Chretien, D., et al., *Lattice defects in microtubules: protofilament numbers vary within individual microtubules.* J Cell Biol, 1992. **117**(5): p. 1031-40.
86. Pierson, G.B., P.R. Burton, and R.H. Himes, *Alterations in number of protofilaments in microtubules assembled in vitro.* J Cell Biol, 1978. **76**(1): p. 223-8.
87. Pampaloni, F., et al., *Thermal fluctuations of grafted microtubules provide evidence of a length-dependent persistence length.* Proc Natl Acad Sci U S A, 2006. **103**(27): p. 10248-53.
88. van den Heuvel, M.G., S. Bolhuis, and C. Dekker, *Persistence length measurements from stochastic single-microtubule trajectories.* Nano Lett, 2007. **7**(10): p. 3138-44.
89. Van den Heuvel, M.G., M.P. de Graaff, and C. Dekker, *Microtubule curvatures under perpendicular electric forces reveal a low persistence length.* Proc Natl Acad Sci U S A, 2008. **105**(23): p. 7941-6.
90. Kikumoto, M., et al., *Flexural rigidity of individual microtubules measured by a buckling force with optical traps.* Biophys J, 2006. **90**(5): p. 1687-96.
91. Trefethen, L.N., *Spectral methods in MATLAB*. Vol. 10. 2000: Siam.
92. Peskin, C.S., *The immersed boundary method.* Acta numerica, 2002. **11**: p. 479-517.
93. Atzberger, P.J., P.R. Kramer, and C.S. Peskin, *A stochastic immersed boundary method for fluid-structure dynamics at microscopic length scales.* Journal of Computational Physics, 2007. **224**(2): p. 1255-1292.
94. Gelfand, I.M. and S.V. Fomin, *Calculus of variations*. 2000, Mineola, NY: Dover.
95. Saitô, N., K. Takahashi, and Y. Yunoki, *The statistical mechanical theory of stiff chains.* Journal of the Physical Society of Japan, 1967. **22**(1): p. 219-226.
96. Reichl, L.E., *A Modern Course in Statistical Physics*. 1997, John Wiley and Sons: New York.
97. Le Cam, L., *Maximum likelihood: an introduction.* International Statistical Review/Revue Internationale de Statistique, 1990: p. 153-171.

98. Taute, K.M., et al., *Microtubule dynamics depart from the wormlike chain model.* Phys Rev Lett, 2008. **100**(2): p. 028102.
99. Howard, J., *Mechanics of Motor Proteins and the Cytoskeleton*. 2001, Sunderland, MA: Sinauer.
100. Yu, D., et al., *Mechanical and functional properties of epothilone‐stabilized microtubules.* Cytoskeleton, 2013. **70**(2): p. 74-84.
101. Cortes, J. and J. Baselga, *Targeting the Microtubules in Breast Cancer Beyond Taxanes: The Epothilones.* The Oncologist, 2007. **12**(271-280).
102. Alvarez, R.H., V. Valero, and G.N. Hortobagyi, *Ixabepilone for the treatment of breast cancer.* Annals of Medicine, 2011. **43**(6): p. 477-486.
103. Bollag, D.M., et al., *Epothilones, a New Class of Microtubule-stabilizing Agents with a Taxol-like Mechanism of Action.* Cancer Research, 1995. **55**(11): p. 2325-2333.
104. Argyriou, A.A., et al., *Peripheral nerve damage associated with administration of taxanes in patients with cancer.* Critical Reviews in Oncology/Hematology, 2008. **66**(218-228).
105. Hagiwara, H. and Y. Sunada, *Mechanism of Taxane Neurotoxicity.* Breast Cancer, 2004. **11**(1): p. 82-85.
106. Lema, M.J., K.M. Foley, and F.H. Hausheer, *Types and Epidemiology of Cancer-Related Neuropathic Pain: The Intersection of Cancer Pain and Neuropathic Pain.* The Oncologist, 2010. **15**: p. 3-8.
107. Wolf, S., et al., *Chemotherapy-induced peripheral neuropathy: Prevention and treatment strategies.* European Journal of Cancer, 2008. **44**(11): p. 1507-1515.
108. Park, S.B., et al., *Mechanisms Underlying Chemotherapy-Induced Neurotoxicity and the Potential for Neuroprotective Strategies.* Current Medicinal Chemistry, 2008. **15**: p. 3081-3094.
109. Park, S.B., et al., *Early, progressive, and sustained dysfunctoin of sensory axons underlies paclitaxel-induced neuropathy.* Muscle and Nerve, 2011. **43**: p. 367-374.
110. Block, S.M., et al., *Probing the kinesin reaction cycle with a 2D optical force clamp.* Proceedings of the National Academy of Sciences, 2003. **100**(5): p. 2351-2356.
111. Feinstein, S.C. and L. Wilson, *Inability of tau to properly regulate neuronal microtubule dynamics: a loss-of-function mechanism by which tau might mediate neuronal cell death.* Biochim Biophys Acta, 2005. **1739**(2-3): p. 268-79.
112. Kieran, D., et al., *A mutation in dynein rescues axonal transport defects and extends the life span of ALS mice.* J Cell Biol, 2005. **169**(4): p. 561-7.
113. LaMonte, B.H., et al., *Disruption of dynein/dynactin inhibits axonal transport in motor neurons causing late-onset progressive degeneration.* Neuron, 2002. **34**(5): p. 715-27.
114. Saxton, W.M., et al., *Kinesin heavy chain is essential for viability and neuromuscular functions in Drosophila, but mutants show no defects in mitosis.* Cell, 1991. **64**(6): p. 1093-102.
115. Ferreira, A., et al., *Suppression of kinesin expression in cultured hippocampal neurons using antisense oligonucleotides.* J Cell Biol, 1992. **117**(3): p. 595-606.
116. Hurd, D.D., M. Stern, and W.M. Saxton, *Mutation of the axonal transport motor kinesin enhances paralytic and suppresses Shaker in Drosophila.* Genetics, 1996. **142**(1): p. 195-204.

117. Tanaka, Y., et al., *Targeted disruption of mouse conventional kinesin heavy chain, kif5B, results in abnormal perinuclear clustering of mitochondria.* Cell, 1998. **93**(7): p. 1147-58.
118. Taute, K.M., et al., *Microtubule Dynamics Depart from the Wormlike Chain Model.* Physical Review Letters, 2008. **100**(2): p. 028102.
119. Hawkins, T., et al., *Perturbations in Microtubule Mechanics from Tubulin Preparation.* Cellular and Molecular Bioengineering, 2012. **5**(2): p. 227-238.
120. Hawkins, T., et al., *Mechanics of microtubules.* Journal of Biomechanics, 2010. **43**(1): p. 23-30.
121. Huzil, J.T., et al., *A Unique Mode of Microtubule Stabilization Induced by Peloruside A.* Journal of Molecular Biology, 2008. **378**(5): p. 1016-1030.
122. Khrapunovich-Baine, M., et al., *Hallmarks of Molecular Action of Microtubule Stabilizing Agents.* Journal of Biological Chemistry, 2011. **286**(13): p. 11765-11778.
123. Correia, J.J. and S. Lobert, *Physiochemical Aspects of Tubulin-Interacting Antimitotic Drugs* Current Pharmaceutical Design 2001. **7**(13): p. 1213-1228.
124. Meurer-Grob, P., J.r.m. Kasparian, and R.H. Wade, *Microtubule Structure at Improved Resolutionâ€* Biochemistry, 2001. **40**(27): p. 8000-8008.
125. Choi, M.C., et al., *Human Microtubule-Associated-Protein Tau Regulates the Number of Protofilaments in Microtubules: A Synchrotron X-Ray Scattering Study.* Biophysical Journal, 2009. **97**(2): p. 519-527.
126. Lopez, B.J. and M.T. Valentine, *Mechanical effects of EB1 on microtubules depend on GTP hydrolysis state and presence of paclitaxel.* Cytoskeleton (Hoboken), 2014. **71**(9): p. 530-41.
127. Balint, S., et al., *Correlative live-cell and superresolution microscopy reveals cargo transport dynamics at microtubule intersections.* Proc Natl Acad Sci U S A, 2013. **110**(9): p. 3375-80.
128. Sbalzarini, I.F. and P. Koumoutsakos, *Feature point tracking and trajectory analysis for video imaging in cell biology.* J Struct Biol, 2005. **151**(2): p. 182-95.
129. Bouzigues, C. and M. Dahan, *Transient directed motions of GABA(A) receptors in growth cones detected by a speed correlation index.* Biophys J, 2007. **92**(2): p. 654-60.
130. Baas, P.W., T.P. Pienkowski, and K.S. Kosik, *Processes induced by tau expression in Sf9 cells have an axon-like microtubule organization.* J Cell Biol, 1991. **115**(5): p. 1333-44.
131. Kanai, Y., et al., *Expression of multiple tau isoforms and microtubule bundle formation in fibroblasts transfected with a single tau cDNA.* J Cell Biol, 1989. **109**(3): p. 1173-84.
132. Takemura, R., et al., *Increased microtubule stability and alpha tubulin acetylation in cells transfected with microtubule-associated proteins MAP1B, MAP2 or tau.* J Cell Sci, 1992. **103 (Pt 4)**: p. 953-64.
133. Kanai, Y., J. Chen, and N. Hirokawa, *Microtubule bundling by tau proteins in vivo: analysis of functional domains.* EMBO J, 1992. **11**(11): p. 3953-61.
134. Porter, M.E. and K.A. Johnson, *Dynein structure and function.* Annu Rev Cell Biol, 1989. **5**: p. 119-51.
135. Woehlke, G. and M. Schliwa, *Walking on two heads: the many talents of kinesin.* Nat Rev Mol Cell Biol, 2000. **1**(1): p. 50-8.

136. Hirokawa, N. and Y. Noda, *Intracellular transport and kinesin superfamily proteins, KIFs: structure, function, and dynamics.* Physiol Rev, 2008. **88**(3): p. 1089-118.
137. Hirokawa, N., Y. Noda, and Y. Okada, *Kinesin and dynein superfamily proteins in organelle transport and cell division.* Curr Opin Cell Biol, 1998. **10**(1): p. 60-73.
138. Hendricks, A.G., et al., *Motor coordination via a tug-of-war mechanism drives bidirectional vesicle transport.* Curr Biol, 2010. **20**(8): p. 697-702.
139. Muller, M.J., S. Klumpp, and R. Lipowsky, *Tug-of-war as a cooperative mechanism for bidirectional cargo transport by molecular motors.* Proc Natl Acad Sci U S A, 2008. **105**(12): p. 4609-14.
140. Kural, C., et al., *Kinesin and dynein move a peroxisome in vivo: a tug-of-war or coordinated movement?* Science, 2005. **308**(5727): p. 1469-72.
141. Gross, S.P., et al., *Coordination of opposite-polarity microtubule motors.* J Cell Biol, 2002. **156**(4): p. 715-24.
142. McVicker, D.P., et al., *Tau interconverts between diffusive and stable populations on the microtubule surface in an isoform and lattice specific manner.* Cytoskeleton (Hoboken), 2014. **71**(3): p. 184-94.
143. Hinrichs, M.H., et al., *Tau protein diffuses along the microtubule lattice.* J Biol Chem, 2012. **287**(46): p. 38559-68.
144. Leung, B.O. and K.C. Chou, *Review of super-resolution fluorescence microscopy for biology.* Appl Spectrosc, 2011. **65**(9): p. 967-80.
145. Rust, M.J., M. Bates, and X. Zhuang, *Sub-diffraction-limit imaging by stochastic optical reconstruction microscopy (STORM).* Nat Methods, 2006. **3**(10): p. 793-5.
146. Frank, J., *Single-particle imaging of macromolecules by cryo-electron microscopy.* Annu Rev Biophys Biomol Struct, 2002. **31**: p. 303-19.
147. Janke, C., et al., *Phylogenetic diversity of the expression of the microtubule-associated protein tau: implications for neurodegenerative disorders.* Brain Res Mol Brain Res, 1999. **68**(1-2): p. 119-28.